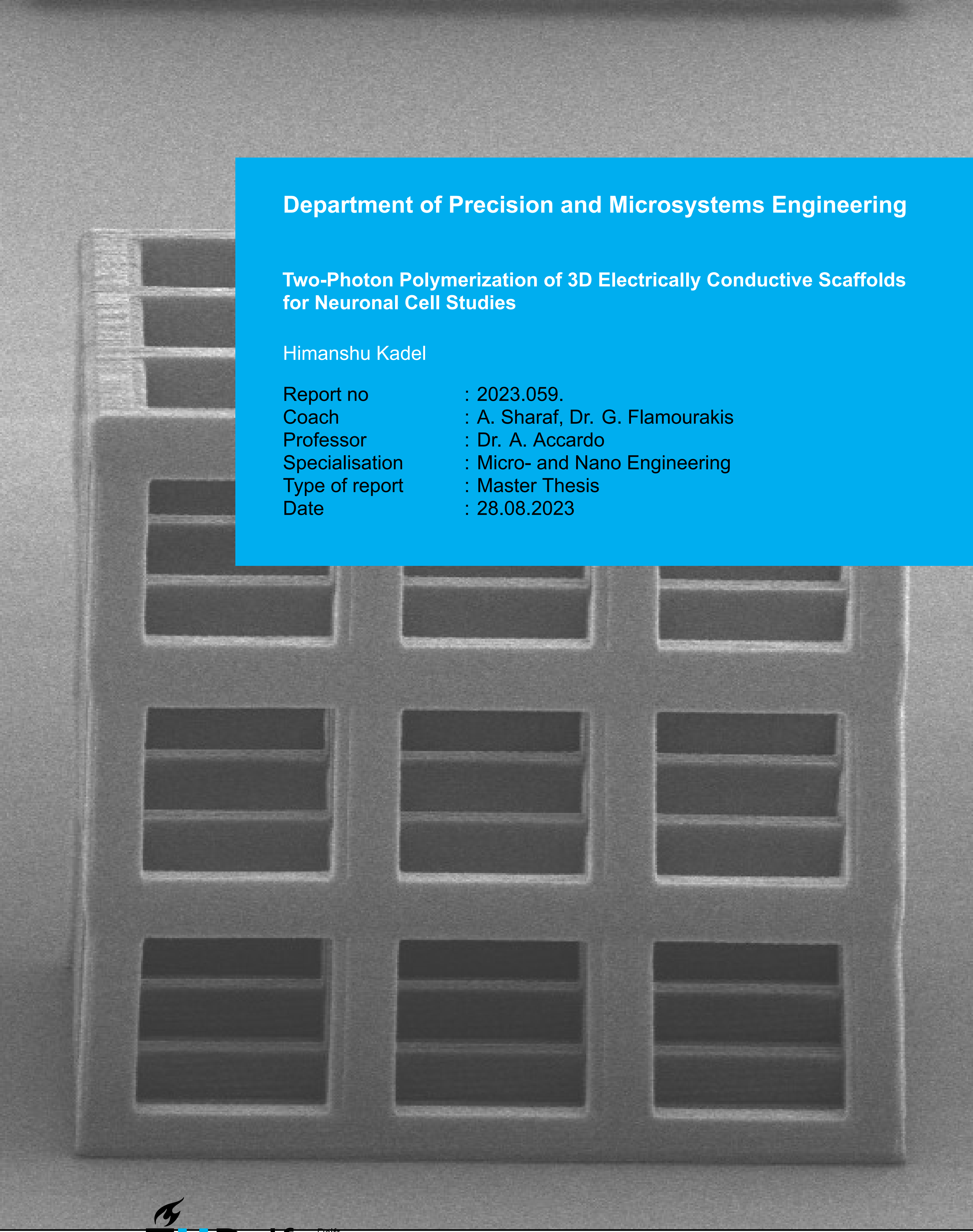

Department of Precision and Microsystems Engineering

Two-Photon Polymerization of 3D Electrically Conductive Scaffolds for Neuronal Cell Studies

Himanshu Kadel

Report no	: 2023.059.
Coach	: A. Sharaf, Dr. G. Flamourakis
Professor	: Dr. A. Accardo
Specialisation	: Micro- and Nano Engineering
Type of report	: Master Thesis
Date	: 28.08.2023

Challenge the future

Delft University of Technology

MSc Thesis

Two-Photon Polymerization of 3D Electrically Conductive Scaffolds for Neuronal Cell Studies

Author:
Himanshu Kadel (5294029)
MSc Mechanical Engineering student
(High Tech Engineering)

Supervisor:
Dr. Angelo Accardo
Assistant Professor

Daily Supervisors:
Ahmed Sharaf
PhD student

Dr. George Flamourakis
Post Doc

Department of Precision and Microsystems Engineering
Faculty of Mechanical, Maritime and Materials Engineering (3mE)
Delft University of Technology

Master committee:
Dr. Angelo Accardo, Assistant Professor, 3mE, TU Delft
Dr. Massimo Mastrangeli, Associate Professor, EEMCS, TU Delft
Dr. George Flamourakis, Post Doc, 3mE, TU Delft
Ahmed Sharaf, PhD Student, 3mE, TU Delft

Abstract

The brain is the most intricate organ in the human body, yet the underlying mechanisms of its cells and networks are not fully mapped. In addition to this lack of understanding, there are numerous neurological disorders and diseases for which a cure remains elusive. There has been persistent research to understand how neuronal cells function when interfaced to engineered biomaterials. The mechanical, topological, and chemical features of the extracellular matrix influence neuronal cell growth, and, among these, also electrical cues play a fundamental role in steering cell fate. The importance of electrical stimulation and 3D engineered microenvironments, better mimicking the spatial configuration followed by cells in the natural brain tissue, necessitates therefore the design of electrically conductive 3D microstructures. In light of the limited number of 3D electrically conductive scaffold studies, their reproducibility issues as well as fabrication constraints, the aim of this thesis is to at develop 3D electrically conductive free-standing microstructures made of polymeric materials. To achieve this goal, a protocol involving the chemical oxidative polymerization of EDOT (3,4-ethylene dioxythiophene) into PEDOT, an electrically conductive polymer, is developed. To ensure conductivity throughout polymeric 3D microstructures, EDOT is incorporated into an acrylate-based resin (IP-L) and 3D printed via two-photon polymerization (2PP), a 3D printing technology with sub-micrometre resolution. The electrical conductivity is experimentally measured, and it is reported how the tuning of printing parameters and organic solvents have a significant influence, with a maximum conductivity of 17.43 S/m after Dimethyl sulfoxide (DMSO) treatment. The mechanical properties of the 2PP-printed structures are evaluated as well, highlighting that the stiffness of microstructures decreases as EDOT doping increases. The versatility of the developed approach is demonstrated by fabricating 3D cage matrices featuring geometries suitable for neuronal cell culture. The reported results pave the way to further investigate the effect of 3D electrically conductive PEDOT-doped microstructures on neuronal cell growth and development.

Acknowledgements

I am grateful to everyone who supported me while completing this thesis. It was a journey full of challenges, learning experiences, and personal growth, and I couldn't have done it without their help and encouragement.

I am incredibly thankful to my supervisor, Dr. Angelo Accardo, for allowing me to work on this exciting project and guiding me throughout the process. They allowed me to experiment freely and always provided valuable feedback and insights. I would like to give my special thanks to my daily supervisor, Ahmed Sharaf and Dr. George Flamourakis, for clarifying my numerous doubts and helping me with using the lab equipment and giving me much needed encouragement.

I would also like to thank my colleagues from Angelo's group for sharing valuable tips and tricks about microfabrication tools and processes. Additionally, I am grateful to Dr. Massimo Mastrangeli, Associate Professor at EEMCS TU Delft, for his invaluable insights on understanding the electrical behaviour of my material. I would like to thank Thomas Michalica for his help in guiding me to respective lab technicians and approaches.

I want to acknowledge the lab engineers and technicians who provided endless support, especially Alex van den Bogaard, for helping me with the sealed glass tube and support in the chemical lab. I also want to thank Satadal Dutta for helping me with the protestation. It was crucial equipment for my thesis.

Working at different labs at PME required a lot of coordination and organization, and I am grateful to the fantastic technicians of the PME department for providing tool training and keeping the workshop running.

Finally, I would like to express my sincere gratitude to my parents for raising me into who I am today and providing me with the opportunity and support to pursue my dreams. I would also like to thank my sisters and friends for keeping my morale up during my need.

Contents

List of Figures

List of Tables

Nomenclature

Abbreviations

Abbreviation	Full form
2PP	Two-photon polymerization
ECM	Extracellular Matrix
PEDOT	Poly(3,4-Ethylenedioxythiophene)
EDOT	3,4-Ethylenedioxythiophene
SLA	Stereolithography
3DP	3D printing
ES	Electrical stimulation
ECP	Electrically conductive polymer
EF	Electric field
ES	Electric stimulation
PNS	Peripheral nervous system
CNS	Central nervous system
NSC	Neural stem cells
FT NSC	Filum Terminale Neural stem cell
hBMMSC	human Bone Marrow Mesenchymal stem cells
hMSC	human Mesenchymal Stem cells
MSC	mesenchymal stem cells
iPSC	induced pluripotent stem cells
ESC	Embryonic stem cells
CNT	Carbon Nanotubes
GO	Graphene Oxide
GNP	Graphene nanoplatelets
MWCNT	Multiwalled Carbon nanotubes
NP	Nanoparticles
DLP	Digital Light Processing
AM	Additive Manufacturing
DLW	Direct laser writing
PEDOT TMA	Poly(3,4-ethylenedioxythiophene)-tetramethacrylate
PEDOT PSS	poly(3,4-ethylenedioxythiophene) polystyrene sulfonate
IPA	Isopropanol

1

Introduction

As the global population grows, so has the demand for functional replacements to repair or enhance damaged tissue function. Within the field of tissue engineering, a multidisciplinary approach integrating scaffolds, cells, and biological molecules has been pursued to devise solutions for tissue repair, preservation, and enhancement. Microstructures, an essential part of tissue engineering research, have contributed a synthetic extracellular matrix (ECM) that directs cellular organisation within a three-dimensional architecture, serving as a highly relevant in vitro platform for imparting physical cues to cells. Notably, functional microstructures have garnered substantial scholarly interest due to their potential to yield functional tissue substitutes and simulate critical cellular and tissue-level phenomena [1]. Accordingly, various methodological approaches have been employed contingent upon the specific tissue under investigation and the distinctive requisites of each application. The requisite material composition and its inherent qualities for scaffold fabrication have exhibited considerable heterogeneity.

Among the organs studied in tissue engineering, the brain is the most intricate and indispensable organ in the human body. Yet, the brain and nervous system present specific challenges in tissue engineering due to their complexity, neuronal connectivity, blood-brain barrier, electrical integration, and long-term viability. Neurons, the fundamental units constituting the brain and nervous system, perform pivotal roles in receiving sensory input from the external environment, transmitting motor commands to musculature, and processing and relaying electrical signals throughout these intricate processes. Such functions hinge on transmitting electrical signals in the form of ions. Consequently, replicating this complex behaviour during cellular studies represents an essential research avenue to develop more stimulatory ECM. Electrical stimulation (ES) has been demonstrated to steer the growth and development of neurons [2, 3]. Furthermore, ES has exhibited the capability to enhance control over cellular processes, encompassing proliferation, adhesion, morphology, and development. In the realm of tissue engineering research, ES has been effectively harnessed to enhance cardiac function, facilitate stem cell differentiation [4], influence cell alignment [5], promote neurite growth, expedite wound healing, facilitate electrotaxis, and foster tissue regeneration [6].

Several methods have been explored to create electrically conductive scaffolds, including electrospinning [7], stereolithography [8], nanoparticle infusion in hydrogel [9], bioprinting [10], and two-photon polymerisation (2PP). Among these fabrication techniques, 2PP stands out due to its distinctive characteristics. This technology employs an additive 3D printing process, utilising targeted femtosecond laser pulses' absorption in photoresist materials. Notably, 2PP achieves a remarkable voxel resolution of up to 200 nm [11], enabling the fabrication of photonic meta-materials [12], microfluidic and biological devices [13], MEMS [14], and actuators. Given its capabilities, 2PP has found applications in scaffolds used in regenerative medicine and tissue engineering. Researchers have successfully fabricated microstructures through 2PP, utilising hybrid organic/inorganic sol-gels [15, 16], and acrylate-based negative tone photoresists [11, 17]. While the focus has predominantly been on 2PP processability, structural resolution, and mechanical properties of photoresist materials, the evolving demand for functional materials drives the need to expand the functionality of photoresists [18]. One such area of interest is imparting electrical conductivity to microstructures, reflecting a significant advancement in electrically conductive microstructures for tissue engineering. Therefore, a fabrication method that allows 3D micro structuring with a mechanism that permits ion-electron exchange will advance electrically conductive microstructures in tissue engineering.

The literature retrieval for this thesis begins with examining the papers listed in the project proposal [19–22]. Subsequently, the research delves into exploring literature on the functioning of the brain and neurons. An extensive literature survey is conducted, encompassing topics such as the ECM, artificial ECM, and various fabrication techniques for ECM. The investigation then progresses to study the impact of ES on neuronal cells and the contemporary methods employed in fabricating electrically conductive scaffolds. After the literature review, the 2PP working principle is elucidated, and the problem statement and research questions are formulated. At this stage, the research plan addresses the fabrication of electrically conductive poly(3,4-ethylene dioxythiophene) (PEDOT)-doped microstructures. Scanning electron microscopy (SEM) and optical microscopy characterise the microstructures. Additionally, the electrical conductivity of the fabricated structures is assessed through two and four-point measurements. Furthermore, the mechanical stiffness of the doped and control structures is characterised. As a proof of principle to highlight the method's versatility, 3D cage-like microstructures are fabricated in the concluding phase of the research.

2

Background

2.1. Nervous System

The nervous system is a fundamental and intricate human body component characterized by two primary divisions, the central nervous system (CNS) and the peripheral nervous system (PNS). The CNS encompasses the brain and the spinal cord, representing the core processing unit responsible for integrating and interpreting sensory inputs. In contrast, the PNS primarily comprises nerves, which are bundles of axons facilitating extensive connections between the CNS and all other body parts.

External stimuli are transduced into electrical impulses, subsequently transmitted to the CNS for storage and intricate processing. In response, the nervous system elicits motor responses by generating electrical impulses that activate effectors, such as muscles or glands [23].

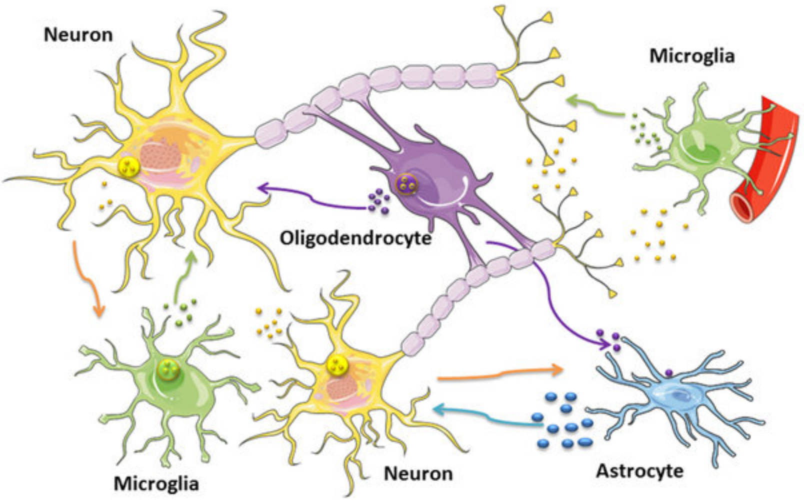

Figure 2.1: A schematic diagram of the central nervous system showing the interaction between neurons and multiple types of glial cells (oligodendrocytes, microglia, and astrocytes). The interaction here is mainly taking place via chemical neurotransmitters shown as yellow or blue small circles [24]

The nervous system is an immensely complex ensemble of around 100 billion neurons, also called nerve cells, accompanied by a substantially larger population of glial cells, which play essential supporting and protective roles for the neurons [25]. Neurons perform a vital function by receiving and transmitting information through both chemical neurotransmission and electrical signalling. Through intricate interactions, these cells form complex neural networks within the brain, enabling the analysis and interpretation of the vast influx of information received from the PNS. Figure 2.1 illustrates three distinct types of glial cells in the CNS, namely astrocytes, oligodendrocytes, and microglia, in conjunction with neurons. Additionally, the presence of ependymal cells is observed, ciliated-epithelial glial cells lining the surfaces of the brain's ventricles and the spinal canal [23, 24].

2.1.1. Neurons

Neurons represent one of the most vital building blocks of the nervous system, and their fundamental structure is illustrated in Figure 2.2. These specialized cells exhibit various protrusions originating from the cell body. Among these structures are the dendrites, characterized by short and branching processes, and the axon, typically longer than the dendrites. Dendrites are pivotal in two essential neuronal functions: receiving and processing incoming information, primarily occurring within the dendrites and cell body. In contrast, axons maintain a relatively uniform diameter along their length. To facilitate efficient nerve impulse transmission, axons are coated with myelin, an insulating material. At the end of the axon, it divides into multiple branches, forming bulbous swellings known as axon terminals or nerve terminals. These axon terminals establish connections with target cells [26].

Like other cells, neurons possess a cell body, the soma, the nucleus-containing core. Due to the substantial protein demands of neurons, most neuronal proteins are synthesized within the soma. The diameter of the soma typically varies within the range of 5 to 140 μm [23].

Neurons communicate with one another through chemical messengers known as neurotransmitters. This intricate intercellular signalling involves the release of neurotransmitters into the synapses, which are the junctions between neurons. Combining specific neurotransmitters can initiate an electrical current that swiftly travels along the nerve cell. The movement of ions generates this electrical impulse, as a potential difference exists across the axon membrane. Subsequently, the electrical signal is propagated along the length of the axon, facilitated by the flow of ions through membrane channels [26].

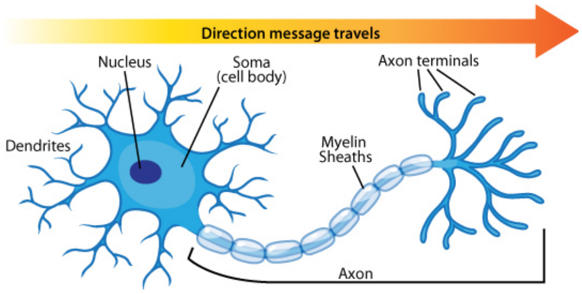

Figure 2.2: Anatomy of Neuron [26]

2.2. Extracellular Matrix

The Extracellular Matrix (ECM) is a complex and dynamic network consisting of diverse multi-domain macromolecules arranged in a cell- and tissue-specific manner. These ECM components interconnect to form a structurally stable composite, contributing significantly to the mechanical properties of tissues. Moreover, the ECM serves as a reservoir for growth factors and various bioactive compounds. Its highly dynamic nature is critical in dictating and regulating fundamental cell behaviours and features, including proliferation, adhesion, migration, polarity, and differentiation [27]. Figure2.3 presents a schematic representation of the ECM.

Collagen stands out as the principal protein constituent of the ECM, conferring strength and resilience to the tissue. Another crucial protein, fibronectin, anchors the cell surface to the basal lamina, a specialized ECM layer. Cell-to-ECM adhesion is governed by specific proteins known as integrins, which facilitate the transmission of mechanical stimuli from the ECM to the cytoskeleton. This intricate structure aids in preserving cellular shape and internal organization. Additionally, actin, a protein forming microfilaments in the cytoskeleton, plays a crucial role in cell crawling through the formation of branched filaments[28]

The ECM in the brain can be categorized into three major components: the basal lamina, surrounding cerebral vasculature; the perineuronal net, enveloping neuronal cell bodies and dendrites; and the neural interstitial matrix, distributed between cells in the brain parenchyma (the functional tissue of the organ). This macromolecular network comprises proteins and polysaccharides, filling the space between neurons and glial cells. In the adult brain, the ECM accounts for approximately 20% of the total volume and exhibits a stiffness of around 1 KPa [29]. Gray matter has a conductivity value of 0.26 S/m, while the white matter has a conductivity value of 0.17 S/m, according to [30]. Gray matter is responsible for information processing, while white matter facilitates communication between gray matter areas and the rest of the body. Neurons in gray matter are made up of cell bodies and their dendrites.

The brain ECM primarily consists of non-fibrillar components, including hyaluronic acid and ECM proteins, such as proteoglycans, glycosaminoglycans, and tenascins. Collagens and specific proteins like fibronectin and laminin are predominantly localized to the vascular basement membrane. Hyaluronic acid can interact with link proteins, forming perineuronal nets on the surfaces of neurons in association with tenascins.

Apart from neurons, the brain also harbours various cell types, including vascular cells like endothelial cells and pericytes, glial cells such as astrocytes, oligodendrocytes, and microglia, as well as immunological cells like microglia[29]. The intricate ECM architecture and composition play crucial roles in supporting the structural integrity and functions of the brain tissue, including cell adhesion, migration, and signalling processes [31].

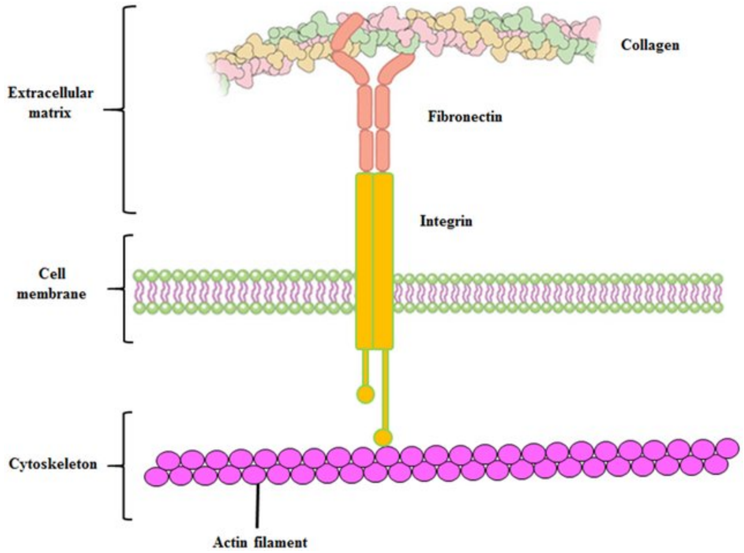

Figure 2.3: Schematic representation of the extracellular matrix (ECM). [28]

2.2.1. Artificial micro-environments for neurons

In biological research, 2D cell culture has been the traditional and widely used approach due to its simplicity, cost-effectiveness, and reproducibility. However, 3D cell culture systems have gained increasing prominence as they offer greater complexity and better mimic the *in vivo* environment. When cells are cultured in 3D, significant changes occur in their shape, motility, and polarity, as illustrated in Figure 2.4. This transition to 3D culture provides researchers with a more physiologically relevant platform to study cell behaviour and responses, making it particularly suitable for investigations aiming to recreate native tissue conditions.

Cell culture studies employ two main types of scaffolds: reconstituted matrices composed of biomacromolecules derived from animal tissues and synthetic ECM mimics. Surface coatings can enhance cell adherence, while 3D scaffolds allow the embedding of cells in an environment that more closely resembles *in vivo* conditions. An essential feature of synthetic ECM is the ability to tailor specific biophysical characteristics, such as mechanical properties or permeability, to examine their influence on cell fate. Various natural and synthetic polymers have created ECM mimics [32]. This diversity in scaffold design allows researchers to investigate the impact of various microenvironments on cellular behaviour, ultimately advancing our understanding of cell biology and tissue engineering applications.

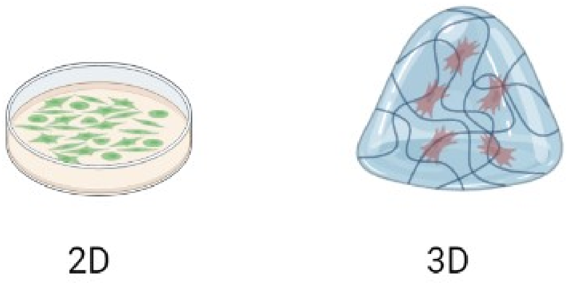

Figure 2.4: 2D and 3D microenvironment for cell [32].

As illustrated in Figure 2.5, several microenvironmental characteristics can significantly influence the fidelity with which a 3D model replicates cellular activity in an *in vivo* setting. The bidirectional arrows in the figure emphasize the interdependent relationship between these factors and the cells themselves. These microenvironmental features include factors such as cell-cell interactions, cell-matrix interactions, and mechanical properties of the extracellular matrix. The spatial arrangement of cells within the 3D model can also impact cellular behaviour and function. The complexity and bidirectional interactions between these microenvironmental factors are crucial considerations when designing and utilizing 3D cell culture models to mimic better the physiological conditions found *in vivo* [33].

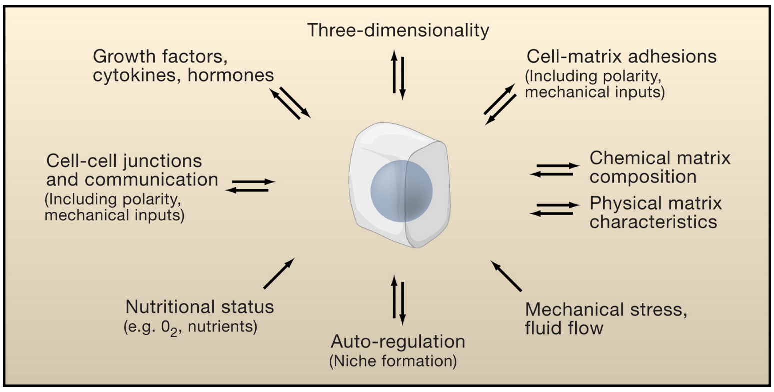

Figure 2.5: Environmental factors affecting cell development. [33]

The composition, stiffness, and topological structure of the extracellular matrix (ECM) scaffold play a vital role in determining its functionality and influencing cellular interactions with the material. The mechanical properties of the ECM are known to have an impact on embryo development, while tissue stiffness can significantly influence organ development. As depicted in Figure 2.6, various artificial 3D ECM models have been developed for neuronal studies, emphasizing the importance of tailoring the ECM to specific research needs. The methods used to fabricate artificial ECM are elaborated in Section 2.4.

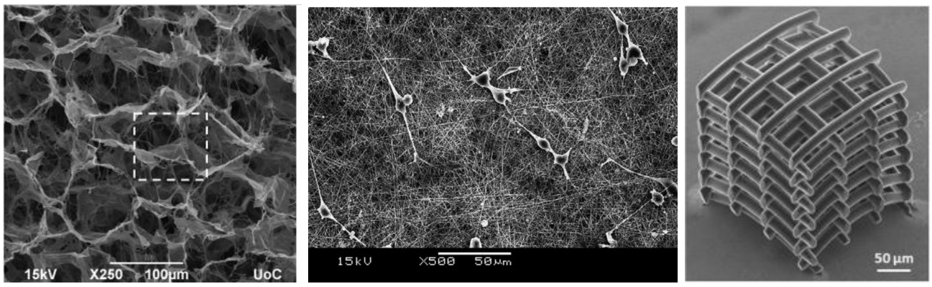

(a) **(b)** **(c)**

Figure 2.6: DIfferent artificial ECM for neuronal studies, (a) Porous Hydrogel [34], (b) Electrospun Fibre [35], (c) 2PP[17]

2.3. Effect of electrical stimulation and electrically conductive materials

Stem cells possess the remarkable ability to undergo self-renewal and differentiate into a diverse array of specialized cell types. Over the past decades, various stem cells types, such as neural stem cells (NSCs), mesenchymal stem cells (MSCs), induced pluripotent stem cells (iPSCs), and embryonic stem cells (ESCs), have been extensively studied both *in vitro* and *in vivo*, aiming to explore their therapeutic potential for regenerative treatments.

Electrotaxis is a phenomenon observed in biological cells or organisms wherein directed motion occurs in response to an electric field or current. This process can manifest in migration, cell growth, and differentiation. External ES offers artificial stimulation for electrically active cells like neurons, directly imparting an electrical charge to promote specific cellular responses. The therapeutic potential of external ES has been extensively investigated, particularly in the context of nerve regeneration following damage. Studies have demonstrated that ES applied to the medium can enhance brain cell proliferation, suggesting its potential role in promoting neural tissue repair and regeneration [36]

Table 2.1 lists several electrically conductive scaffolds and their effects on cells. Some examples from the literature and their effects are briefly described here.

Migration, Figure 2.7 shows the path of neutrophils, a type of white blood cells, with and without Electric Field's (EF) action. It is an example of how cells migrate toward the electric field [37].

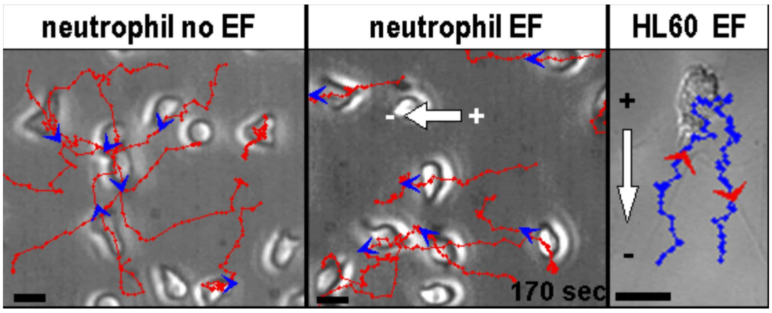

Figure 2.7: Behaviour of neutrophil with and without EF. Image reconstructed from[37]

The differentiation process in neural stem cells (NSCs) is commonly assessed by staining a protein called MAP2. Figure 2.8 presents the results of MAP2 staining performed on Filum Terminale NSCs (FT NSCs) in the presence and absence of an electric field (EF). The filum terminale (FT) is a thin tissue band connecting the spinal cord to the coccyx. Notably, the observations indicate that in the absence of an EF, there is minimal differentiation compared to when an electric field of 150 mV/mm is applied [38]. These findings highlight the significant effect of the electric field on the differentiation process of NSCs, suggesting the potential of electrical stimulation as a regulatory factor in directing cellular fate.

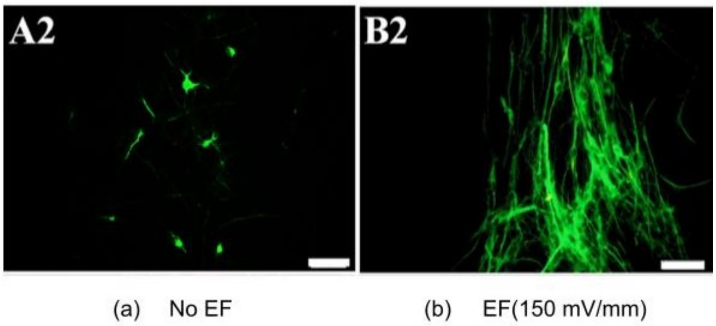

(a) No EF (b) EF(150 mV/mm)

Figure 2.8: FT-NSC in (a)No EF, (b)150 mV/mm EF stimulation. Image reconstructed from [38]

Figure 2.9 shows neurite outgrowth of cochlear neural explants grown on a conductive film made of Polypyrrole, which contains Neutrophin (NT-3) - a protein that induces the survival, development, and function of neurons. When exposed to ES [39, 40], the neurite length and spread changed.

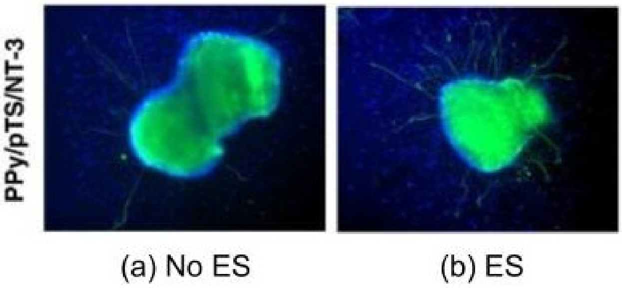

(a) No ES (b) ES

Figure 2.9: Neurite outgrowth from cochlear neural explants grown on the Polypyrrole with Neurotrophin. Image reconstructed from [40].

Intracellular Ca2+ dynamics *in vitro*: hMSCs showed increased levels of Ca2+ oscillations when exposed to DC electric field.[41][42].

It is observed that ES with the direct current affects mobility, directional migration, neurite length, and differentiation. Alternating current does not affect migration and alignment but has enhanced differentiation compared to no ES[43]

2D and 3D conductive material (without ES) has shown increased neurite length, cell migration, adhesion, proliferation, neuron differentiation, and inhibited astrocyte differentiation.[43]

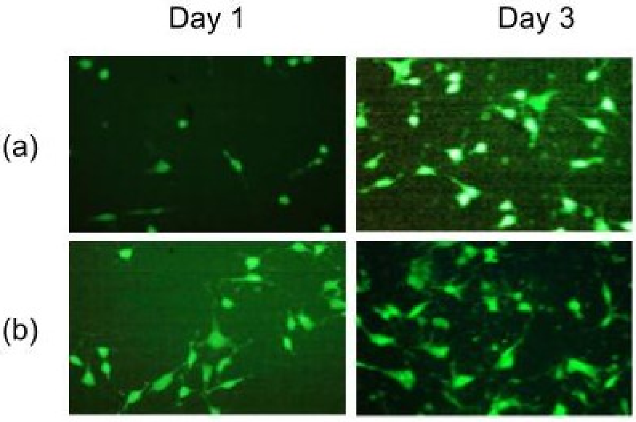

Figure 2.10: Fluorescence images of HT-22 rat hippocampal neuron on the scaffolds. (a)Chitosan (b) C/M. Image reconstructed from [44]

Figure 2.10 shows the day three fluorescent images of AO-stained live HT22 cells on Chitosan and Chitosan + 0.5% wt MWCNT (multiwalled carbon nanotubes) (C/M) substrate. Here it is observed that 20% more proliferation on the composite substrate is linked to the presence of MWCNT even without ES, and 70% more on C/G (Chitosan + 0.5 wt GNP, Graphene Nano Platelets). The cell spread was 40% more in C/G and no change in C/M compared to the control. C/M had conductivity of 1.89875 x 10^{-7} S/cm [44]

The influence of carboxylated multi-walled carbon nanotubes (MWCNTs) on human bone marrow-derived mesenchymal stem cells (hBMMSCs) is examined on a collagen substrate. Figure 2.11 demonstrates the impact of carboxylated MWCNTs on hBMMSC neural differentiation. Remarkably, the group treated with carboxylated MWCNTs exhibited sustained expression of neural markers, implying their potential to autonomously induce and maintain hBMMSC neural differentiation without external factors [45].

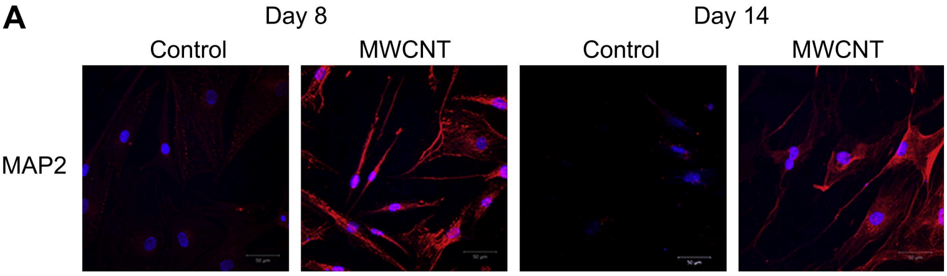

Figure 2.11: Immunofluorescence of hBMMSCs cultured on control and MWCNT groups in the basal medium. Image reconstructed from[45]

2.4. Microfabrication methods

Various fabrication techniques are utilized to create electrically conductive microstructures. While some methods yield directly conductive structures, others involve post-processing steps to confer electrical conductivity.

2.4.1. Electrospinning

Electrospinning is a fabrication technique that employs electrostatic forces to generate fibrous structures spanning from micrometres to nanometers in diameter, contingent on polymer types and processing conditions. This method holds considerable appeal for producing polymer biomaterials, offering simplicity in equipment and enabling the monitoring of morphology, porosity, and composition. Electrospinning has been widely utilized in tissue engineering to create fibrous scaffolds that mimic the ECM, utilizing biocompatible polymers.

For the production of electrically conductive nanofibers, two approaches are commonly employed. One involves coating the substrate with an electrically conductive polymer (ECP), while the other entails fabricating the fibres using the same ECP. Figure 2.12a presents an SEM image of Electrospun Polyvinylidene fluoride fibres coated with polyaniline through oxidative polymerization [7]. This method showcases the capability of Electrospinning to create nanofiber structures with enhanced electrical conductivity, which holds potential for various applications, including tissue engineering and neural interfacing.

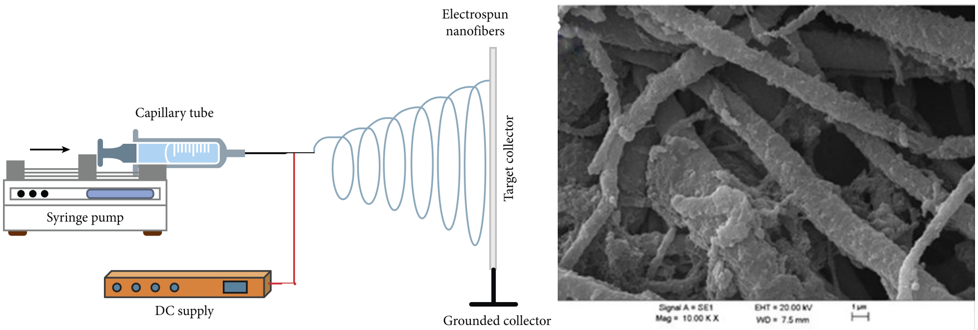

(a) (b)

Figure 2.12: (a) Illustration of Electrospinning device[46], (b) Polyvinylidene Flouride - Polyaniline Electrically conductive Electrospun fibres[7]

2.4.2. Nanoparticles Infused Hydrogels

Polymeric and inorganic nanoparticles, including noteworthy examples such as gold nanoparticles (AuNPs) [9] and carbon nanotubes (CNTs) [47], are employed to enhance the electrical conductivity of scaffolds in tissue engineering. This enhancement is significant for tissues with electroactive properties, such as cardiac and neural tissues. In such contexts, efficient electrical signal transmission between cells and throughout the tissue matrix is imperative.

These nanoparticles offer customization potential in size and shape, exhibiting size-dependent optical characteristics and enabling effective functionalization. As depicted in Figure 2.13, the incorporation of functionalized Carbon Nanotubes and Graphene Oxide within an electrically conductive hydrogel is shown to promote the proliferation of PC12 cells (rat medulla cells) and induce neuronal differentiation [48]. This approach underscores the potential of nanoparticle-modified hydrogels in advancing tissue engineering strategies that require enhanced electrical conductivity to support the function and integration of electroactive tissues.

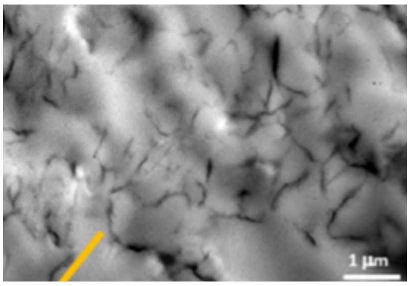

Figure 2.13: SEM image of Graphene oxide and CNT embedded hydrogel. Image reconstructed from[48]

2.4.3. Light-assisted 3D Fabrication

Light-assisted fabrication techniques use photopolymerization, an additive manufacturing technique wherein light is harnessed to polymerize photosensitive resin. This process involves three key components in the photopolymer mixture, as illustrated in Figure 2.14: monomers, oligomers, and photoinitiators. Upon exposure to curing light, photoinitiators initiate the generation of reactive species that catalyze the formation of molecular chains among the monomers and oligomers, leading to polymerization [49]. This technology is pivotal in fabricating intricate structures with high precision and resolution in various fields such as microfabrication, tissue engineering, and electronics.

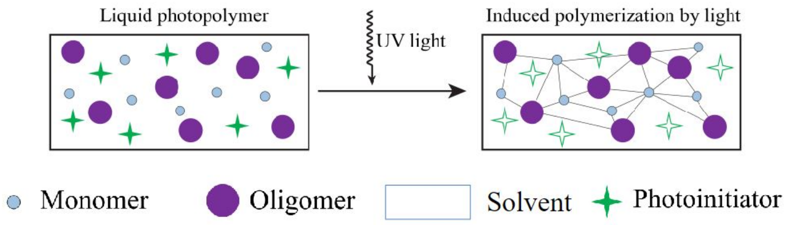

Figure 2.14: Photopolymerization process [49]

There are different kinds of photopolymerization methods,

- **Laser StereoLithography (SLA)** is a notable additive manufacturing method, alternatively referred to as SL, optical fabrication, photo-solidification, or resin printing. Figure 2.15 illustrates a stereolithography system. In the SLA manufacturing process, a highly concentrated ultraviolet light beam or laser is directed onto the surface of a liquid photopolymer contained in a vat. This light exposure induces the fabrication of individual layers of the intended 3D object, achieved through cross-linking or polymer degradation [50]. This technique enables the creation of intricate and precise 3D structures, holding applicability across diverse sectors such as prototyping and biomedical engineering.

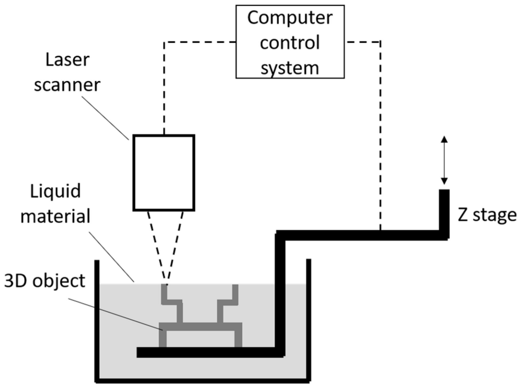

Figure 2.15: Stereolithography system[50]

Figure 2.16 illustrates an electrically conductive scaffold fabricated through StereoLithography (SLA) with a pore size of 800 μm. The scaffold incorporates PEDOT PSS nanofibrils mixed with GelMA, rendering it conductive (sheet resistance of 750 S/cm² at 0.91% nanofibril concentration). A cell viability assay was conducted within the scaffold and PEGDA medium environment using rat dorsal root ganglion cells. Remarkably, no substantial change in cell behaviour was observed without electrical stimulation (ES). Upon application of ES, there was a 30% increase in neural differentiation markers, indicating improved neuronal differentiation [8].

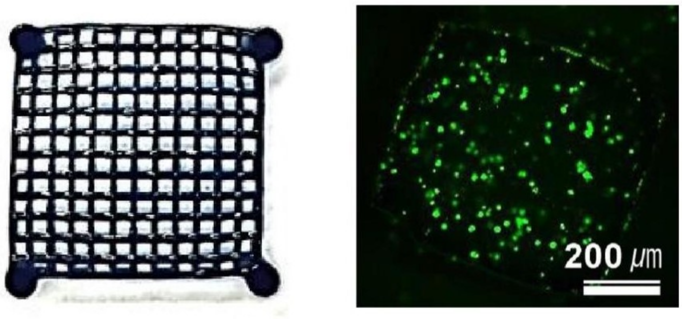

(a) (b)

Figure 2.16: (a)Conductive scaffold with pore size 800 μm, (b) Encapsulated DRG cells in GelMA with 3D printed PEDOT/PSS hydrogel live/dead assay. Image is reconstructed from [8]

- **Digital Light Processing (DLP)** involves using a digital projector screen that rapidly displays an image of each layer across the entire build platform simultaneously. The projected image comprises square pixels, forming each layer as small rectangular bricks called pixels. DLP printing has an advantage in speed for certain components, as each layer is exposed simultaneously rather than being drawn out using a laser [51, 52].
- **Two-photon polymerization(2PP)**, will be discussed in detail in Section 4.4

Table 2.1 lists some of the conductive microstructures fabricated by various methods and the electrical properties of these structures.

Table 2.1: Conductivity of microstructures and effect of ES. Here, EDOT - 3,4-Ethylenedioxythiophene, PEG-DA - Poly(ethylene glycol) diacrylate, GelMA - Gelatin methacryloyl, MWCNT - multiwalled carbon nanotubes, EIS - electrochemical spectroscopy, PEDOT PSS - poly(3,4-ethylene dioxythiophene) polystyrene sulfonate, DMSO - Dimethyl sulfoxide, HT22 cells - mouse hippocampal neuronal cells, GO - Graphene oxide, CNT/PEG - Poly ethylene glycol functionalized carbon nanotube, OPF - oligo(poly(ethylene glycol) fumarate, DRG - Dorsal root ganglion, PC12 - Tumor cells from rat adrenal medulla).

Method	**Material**	**Electrical characterization**	**Cell type**	**Results**	**References**
Porous foam	Graphene	-	NSC	Enhanced differentiation	[53]
Electrospinning	Polyvinyl coated	0.5 S/cm	-	-	[7]
Hydrogel	GO + CNT/PEG + OPF	2.4 - 9 x 10^{-5} S/cm	PC12	Enhanced differentiation (2.5x)	[48]
Composite film (2D)	Chitosan + MWCNT	1.89875 x 10^{-7} S/cm	HT22	Enhanced proliferation (1.2x)	[44]
Conductive film (2D)	Collagen + MWCNT	-	hBMMSCs	Enhanced neural differentiation	[45]
3D printing	PEDOT PSS	28 S/cm	Neural probe coupling (mice)	Enhanced cell viability	[54]
SLA	PANI GELMA	0.025 S/cm	Murine NSC	Increased cell adhesion	[55]
SLA	PEDOT PSS + PEGDA	-	Rat DRG	Enhanced differentiation	[8]
2PP (2D)	PEGMA + PEDOT PSS + DMSO	280 S/cm	-	-	[56]
2PP(3D)	IP + PEDOT PSS film	-	HT22 cells	Enhanced neurite growth	[57]
2PP(3D)	EDOT infused PEG-DA	0.04S/cm	-	-	[18]
2PP(3D)	GelMA MWCNT	-	Cardiomyocytes	Enchanced cell viability	[58]
2PP(3D)	IP L 780 + Ionic liquid	1-4 S/cm	-	-	[59]

2.5. Electrically Conductive Polymers

Electrically Conductive Polymers (ECPs) and their derivatives have gained significant traction in biomedical engineering due to their ability to amalgamate the chemical and physical attributes of organic polymers with the electrical characteristics of metals [60–62]. ECPs offer an electrical stimulus, furnish a physical environment conducive to tissue development and cell proliferation, and afford meticulous control over the duration and strength of the applied stimulation. Additionally, conductive polymers find utility in generating polymeric composites with enhanced structural, mechanical, and electrical properties, a feature particularly advantageous in regenerative medicine. Applications span domains such as cardiac and neurological tissue engineering [63–65].

Chemically conductive polymers comprise conjugated monomers, wherein electron transfer within pi-bonds (the conjugate bond chain of PANI shown in Figure 2.17) underpins their electrical conductivity. Prominent ECPs employed within the biomedical realm encompass polypyrrole (PPy), polyaniline (PANI), and poly 3,4-ethylene dioxythiophene (PEDOT), characterized by their distinctive electrical and optical attributes.

- PANI, commonly called aniline black, is one of the most extensively utilized ECPs due to its cost-effectiveness and straightforward synthesis process. Notably, its electrical conductivity spans a range of 1 to 600 S/cm [66, 67]. This versatility makes PANI a sought-after material for various applications, including its prominent role in electrically conductive materials, sensors, and electroactive coatings. The chemical formula of PEDOT is shown in Figure 2.17.

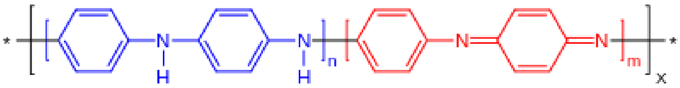

Figure 2.17: PANI Formula

- PPy is one of the most conductive ECPs. Notably, PPy demonstrates commendable stability in both aqueous and atmospheric environments [68]. Additionally, PPy exhibits the advantageous ability to enhance cell proliferation and adherence across various cell types. Regarding its electrical conductivity, PPy showcases a range from 2 to 100 S/cm [69, 70]. This exceptional combination of properties positions PPy as a versatile and promising material for diverse applications, including bioelectrodes, neural interfaces, and tissue engineering scaffolds. The chemical formula of PEDOT is shown in Figure 2.18.

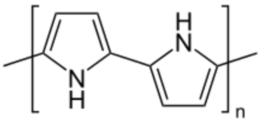

Figure 2.18: PPy Formula

- PEDOT exhibits commendable electrical, environmental, and chemical stability. Notably, PEDOT surpasses PPy in terms of both thermal stability and conductivity. Its electrical conductivity spans a range of 0.3 to 2000 S/cm. Noteworthy is its low intrinsic cytotoxicity, as reported by studies [71], rendering PEDOT well-suited for a spectrum of biological and biosensing applications. Examples include employment in neural electrodes, cardiac muscle patches, and nerve grafts [72]. The robust combination of electrical, mechanical, and biocompatible properties further solidifies PEDOT's standing as a promising candidate in bioelectronic and tissue engineering advancements. The chemical formula of PEDOT is shown in Figure 2.19.

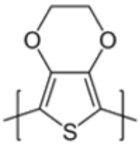

Figure 2.19: PEDOT Formula

Adopting organic conductive materials in bioelectronic devices has garnered substantial attention due to their favourable physical-chemical attributes compared to inorganic counterparts. These attributes encompass various characteristics, including augmented versatility in synthesis and functionalization and improved fabrication and processability. PEDOT:PSS currently takes centre stage as a prominently employed conjugated polymer across diverse bioelectronic applications. A noteworthy functionalisation of PEDOT: PSS is its mechanical properties, which closely emulate those of biological systems. Moreover, it demonstrates a hybrid ionic/electronic conduction mechanism with hole conductivity exceeding 1000 S cm−1. This distinctive attribute enhances communication between cells and microelectrode arrays, emphasizing its pivotal role in advancing interactions between cells and materials. Hence, a comprehensive comprehension of PEDOT synthesis is crucial for fabricating conductive microstructures.

2.5.1. Synthesis of Electrically Conductive polymers

The synthesis of ECPs encompasses various methods. Most ECPs are synthesised through the oxidative coupling of monocyclic (having one ring of molecules) monomers. Two principal approaches are commonly employed in synthesising conductive polymers: chemical synthesis and electro-polymerisation. The synthesis enables the controlled fabrication of ECPs with tailored electrical properties.

- Chemical polymerization involves the connection of carbon-carbon bonds within monomers by applying heat, pressure, illumination, and catalysis. This results in the production of significant amounts of polymerized products. However, it is important to note that this method can also contaminate the final product, negatively affecting its quality and safety [73].
- Electro-polymerisation involves the application of voltage to electrodes, promoting redox reactions to synthesise polymers. This method can be categorised into Cyclic Voltammetry and potentiostatic process. Cyclic Voltammetry entails applying cyclic voltage profiles, while the potentiostatic method involves maintaining a constant voltage. A key advantage of electro-polymerisation lies in the high purity of the resulting products. However, a limitation is that this method is typically suitable for synthesising only a limited number of products simultaneously [73].

The chemical reaction depicted below illustrates the typical pattern observed in the polymerisation of ECP. In this process, the monomers (represented as X) initiate a chain formation by continuously removing H+ ions via chemical or electrical mechanisms. Subsequently, the newly generated ions engage with vacant monomers or existing chains, facilitating the elongation or creation of the polymer chain structure. Reaction 2.1 highlights the importance of ion exchange and polymer chain growth in ECP synthesis.

$$nH–[X]–H \rightarrow H–[X]_n–H + 2(n–1)H^+ + 2(n–1)e^- \tag{2.1}$$

2.5.2. Synthesis of PEDOT

The properties of PEDOT (transparency, electrical conductivity, are highly dependent on the counterion and packing of PEDOT polymer.

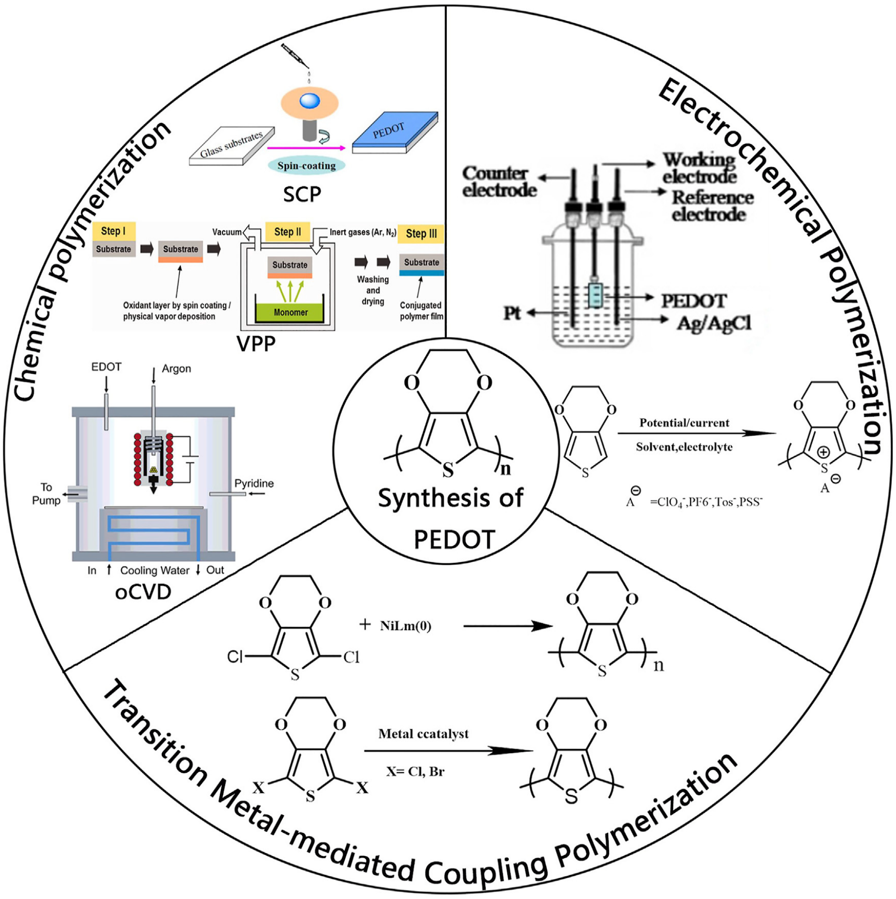

Figure 2.20: Polymerization methods for PEDOT [73]

Oxidative Polymerization

Oxidative Polymerisation is the most common and widely utilised method for producing PEDOT.(Figure 2.20) This process gradually became the dominant method for generating PEDOT and its derivatives. PEDOT's oxidative polymerisation process is separated into two phases. The EDOT monomer is first oxidised to produce cationic radicals, which are then dimerised by free radicals. Dimerisation is the chemical reaction that joins two molecular subunits, forming a single dimer. As a result, the produced dimer undergoes the removal of hydrogen cation, resulting in an active neutral dimer that can react in the subsequent oxidation process for chain development. (Figure 2.21)[73, 74]

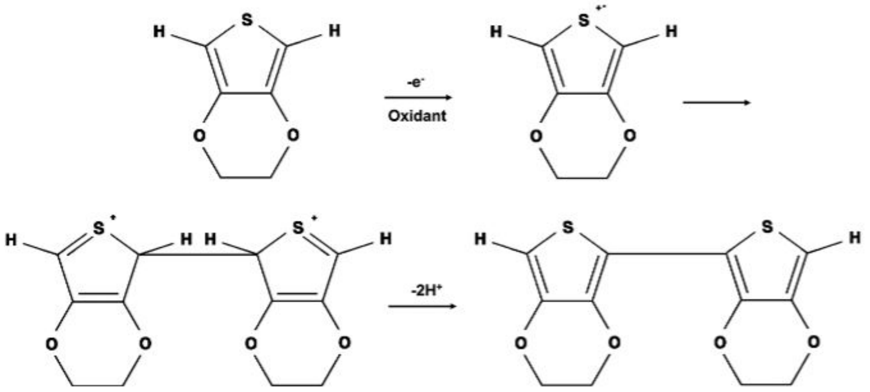

Figure 2.21: Oxidative Polymerization [74]

The conductivity of PEDOT can range from 0.1 S/cm to 2000 S/cm based on chemicals used, time and temperature. The properties of PEDOT synthesised varies dramatically with a change in chemicals and concentration of the anion in the solution. A slow(>6h) reaction leads to smoother and more conductive ECP. This can be achieved using larger anions, compared to chloride, like Fe (III)sulphonates, which are organo-soluble. Adding organic bases also slows down the reaction by increasing the pH of the reaction, thus acting as an inhibitor for positively charged PEDOT.

Electrochemical Polymerization

The Electrochemical Polymerization process is similar to oxidative chemical polymerization. But there are no oxidants in this process, the potential difference polymerizes EDOT, and the polymerization occurs at the electrode. As can be seen in the figure. 2.20, there are three electrodes(Counter, working, reference). Generally, small molecules are used as electrolytes, such as Lithium perchlorate, 1-butyl-3-methylimidazolium hexaphonate (BMIMPF6), and lithium bis (trifluoromethosulfonyl) amide (LiTFSI). Here, the anions of electrolyte solution dope into PEDOT and counterions stabilise the charge in PEDOT. The selection of counterions affects the properties of PEDOT. In this process, high-conductivity films are produced, but the prerequisite is that the substrate should be conductive. The conductivity can go as high as 2000 S/cm, and based on the current and additional chemicals, the optical properties of PEDOT can be changed as well [73, 75].

Transition metal Polymerization

While widely employed for PEDOT synthesis, the methods above can result in impurities leading to doped PEDOT. To address this issue, a strategy involves the initial halogenation (X) of the EDOT monomer using N-chlorosuccinimide. The resulting X-EDOT-X compound then undergoes organometallic dehalogenation polycondensation, facilitated by Nickel complexes (as illustrated in Figure 2.20). This approach yields undoped PEDOT. However, it's important to note that the PEDOT acquired through this process is black in colour, insoluble in water, and non-conductive. Consequently, this methodology is not favoured due to these limitations [76]. Despite its drawbacks, this approach underscores the ongoing efforts to refine PEDOT synthesis techniques to enhance its suitability for various applications.

3

Research Proposal

3.1. Problem Statement

Electrical stimulation applied to neuronal cell cultures is pivotal in orchestrating differentiation, cell migration, and the alignment of neuronal cells (as discussed in Section 2.3). Extensive investigations involving a spectrum of electrically conductive artificial ECM substrates specifically tailored for neuronal cells have been conducted. Noteworthy examples encompass conductive electrospun fibres, electrically conductive hydrogels infused with nanoparticles, nanoparticle-infused 2D and 3D scaffolds fabricated via 2PP (discussed in Section 4.4), as well as scaffolds coated with ECP. These structures offer a dual advantage, electrical stimulation and an environment conducive to cell growth. Consequently, significant cellular responses and alterations are discerned, signifying the potential of these platforms in steering neuronal cell behaviour (details presented in Table 2.1). These insights highlight the promising avenues of harnessing electrical stimulation and electrically conductive scaffolds to advance our understanding of neuronal cell biology.

The engineered microenvironments described above are not without their limitations, emphasising areas for potential improvement and advancement. One notable challenge lies in the design aspect, where prevailing fabrication methods exhibit inherent constraints such as limited resolution and an inability to create entirely free-standing 3D structures. Reproducibility of the fabricated microstructures is another concern, necessitating efforts to enhance the consistency and reliability of these processes. Furthermore, a notable dearth of research exploring electrically conductive 3D scaffolds using the promising 2PP approach suggests a valuable avenue for future investigations. Moreover, exploring conductive resins and associated processes within the context of 2PP is relatively scarce and primarily focused on commercially available solutions, indicating a need for expanded research into novel conductive materials and methodologies.

This study aims to potentially answer these shortcomings by developing a 3D electrically conductive scaffold using two-photon polymerisation. Using 2PP will ensure better resolution, customisable structures, free-standing structures, and reproducibility. This study emphasises developing a protocol to fabricate 3D electrically conductive microstructures using commercially available photoresists and the mechanical and electrical characterisation of the designed structures.

3.2. Research question

How can two-photon polymerisation be employed to fabricate 3D electrically conductive Scaffolds for neuronal cells?

3.2.1. Sub questions

This central question is split into sub-questions in descending order of priority.

- What is the most suitable fabrication approach?

  - **Direct printing,** mixing EDOT in the photoresist (IP-L) prior to 2PP (plan A (section 3.3.1) & plan D (Appendix A.3). If this method is chosen, then the following questions are proposed:
    - What is the relationship between the concentration of monomer and feasibility of fabrication for direct printing of microstructure?
    - What is the relationship between the concentration of oxidising agent and the morphology of structure?

  - **Coating** a conductive layer after the fabrication of the base structure.

    - Which coating approach is more feasible, the one based on the cyclic voltammetric deposition of PEDOT PSS (Plan B(Appendix A.1)) or photopolymerisation of PEDOT TMA (Plan C (Appendix A.2))?
- What are the electrical, morphological and mechanical features of microstructures?
  - What is the relationship between structure conductivity, its integrity, and feature reproducibility?
- What is the uniformity of conductivity in the structure? (Qualitatively by SEM images)
- How does the manufacturing approach affect the porosity of the structure?

3.3. Research Plan

3.3.1. Process plan

Figure 3.1 visually represents the research plan to fabricate electrically conductive microstructures. The plan initiates with the formulation of Plan-A and the requisite training for utilising essential setups, including Nanoscribe for 3D printing employing 2-photon polymerisation (2PP) for nanometric resolution, Scanning Electron Microscope (SEM), and Femtotools for mechanical characterisation.

A backup, Plan B, is activated if the initial optimization of the IP-L and EDOT leads to failure to mix or print. This is illustrated in the process plan.

After establishing the foundational elements, the subsequent steps involve fabricating precise 2D microstructures and characterising their electrical conductivity. Moving forward, the focus shifts to fabricating and characterizing 2.5D structures using SEM imaging to characterise and measure the dimensions. The culmination of research is achieved by refining 3D microstructures, embodying a comprehensive and systematic approach to the research endeavour.

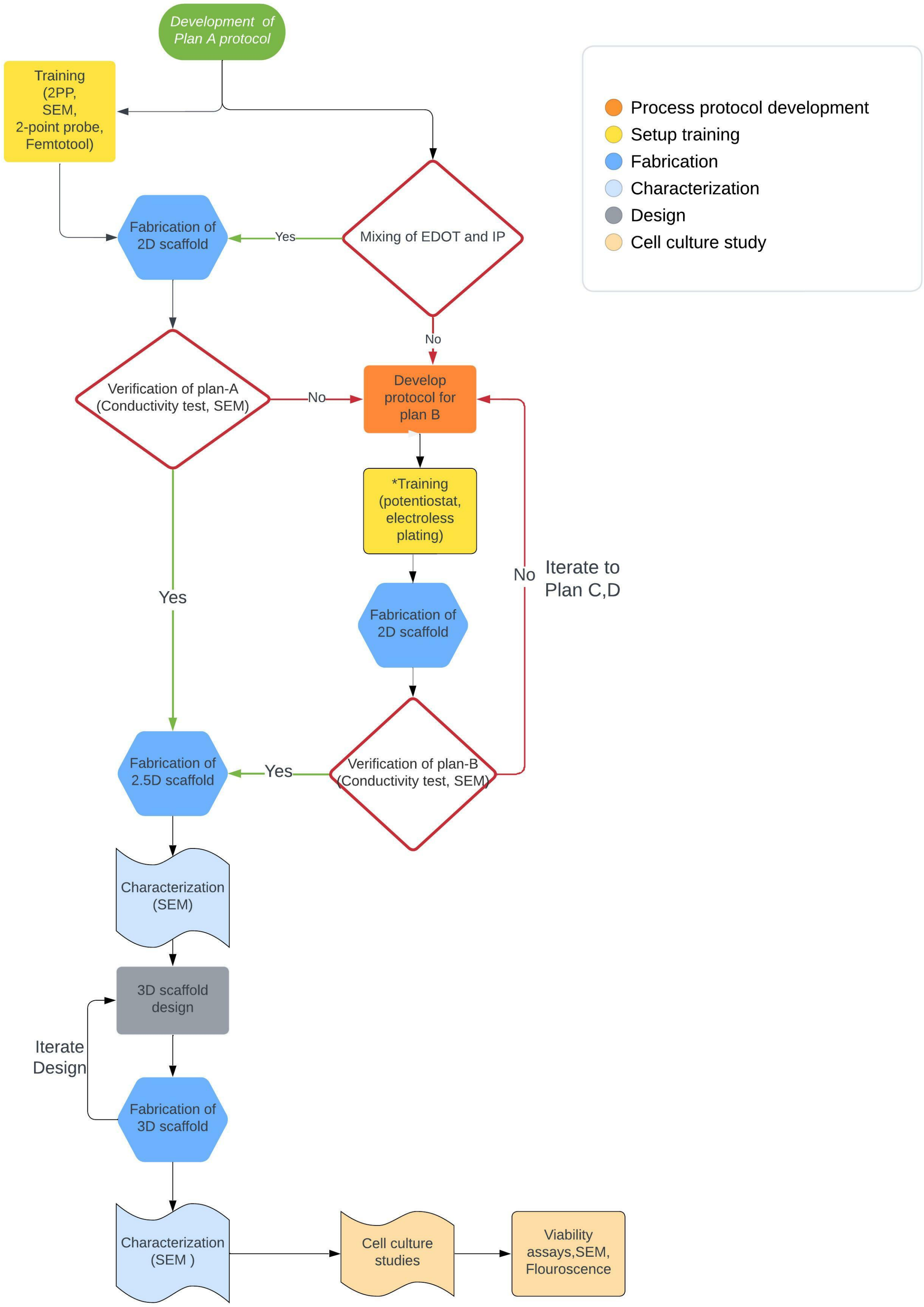

Figure 3.1: Process plan

3.3.2. Risk analysis

In the main fabrication strategy, certain risks are anticipated. They are:

- Mixing of EDOT and IP-L, an acrylate-based photoresin, poses the first risk. Since this is the first step of this plan and the failure in repeated attempts to mix them homogeneously discards this plan. This can happen due to the possible immiscibility of IP-L(hydrophobic) and EDOT(hydrophobic).
- Failure in 2PP of the obtained mixture of IP-L and EDOT. This can happen due to the resultant refractive index of the mixture, here EDOT(1.5765), IP-L(1.477), and substrate(borosilicate, 1.517). A refractive index contrast of > 0.04 is required to use Oil configuration in 63x.
- Failure to chemically polymerize the fabricated microstructure. This can happen due to the impermeability of oxidising agent to the inner layers of the 2PP microstructure.

If plan A fails, three backup plans are formulated: B (Appendix A.1), C (Appendix A.2), and D (Appendix A.3).

3.4. Time plan

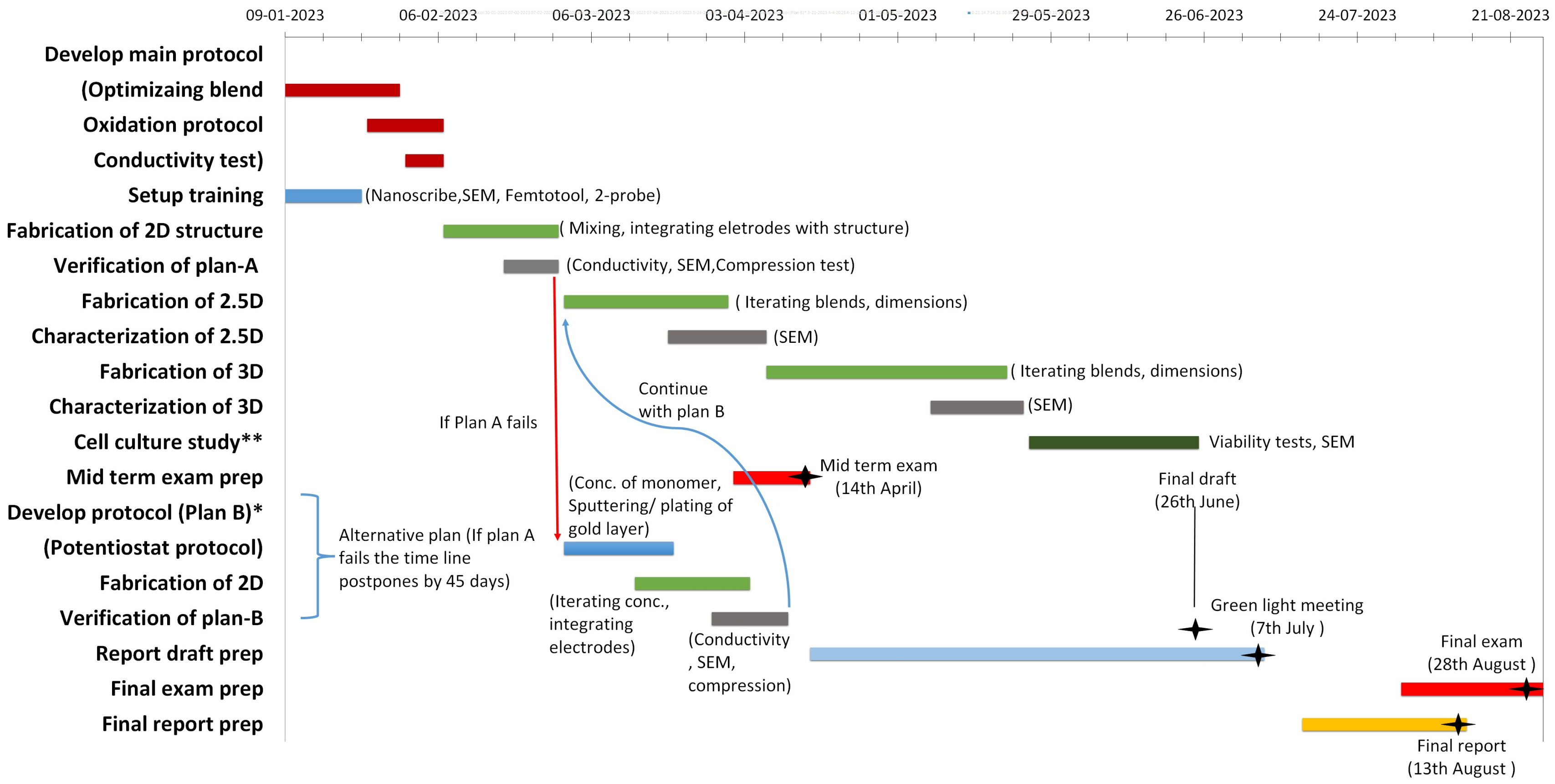

Figure 3.2: Time plan

4

Methodology

In this chapter, the fabrication approach for PEDOT-doped microstructures is discussed. First, an overview of the design and fabrication process is laid out. Afterwards, the used fabrication tools and techniques are introduced and explained. Finally, the chapter culminates in thoroughly examining the verification and characterization steps, providing a comprehensive insight into the complete journey from design to validation of PEDOT-doped microstructures.

4.1. Materials

The materials predominantly used are IP-L, a commercial bio-compatible photoresist from Nanoscribe, and 3,4-ethylene dioxythiophene (EDOT) monomer (Sigma Aldrich). 3-(Trimethoxysilyl)propyl methacrylate (MAPTMS) (Sigma Aldrich) for treatment of substrates. Silicon substrates (25 mm x 25 mm x 0.725 mm) for DiLL-mode 2PP printing, Borosilicate substrates (30 mm diameter and 170 μm thickness) for Oil-mode printing. Immersol oil is used in Oil-mode printing. The DiLL and Oil mode will be discussed in section 4.4. Propylene glycol monomethyl ether acetate (PGMEA) (Sigma Aldrich), Isopropyl alcohol (IPA) as developers, and Novec 7100 to replace IPA. Ferric chloride hexahydrate ($FeCl_3.6H_2O$) as a chemical oxidant in the polymerization of EDOT. Dimethyl Sulfoxide (DMSO) as a remover and for solvent treatment. AZ 4562 resin (MicroChemicals) for maskless lithography using 2PP, AZ 400K developer for AZ resin.

4.2. Process

The fabrication process for PEDOT-doped microstructures involves successive steps, as depicted in Figure 4.1. Starting with the mixing of photoresist (IP-L) and monomer (EDOT), the process progresses to the fabrication of microstructures through 2PP, based on Kurselis et al. [18]. Subsequently, the doped monomers within the microstructures undergo oxidative polymerisation facilitated by an oxidising agent. This transformative step culminates in the yield of conductive microstructures. The final stages encompass a thorough washing procedure followed by storage, rendering the structures ready for subsequent utilisation. This comprehensive process highlights the detailed journey towards the fabrication of PEDOT-doped microstructures.

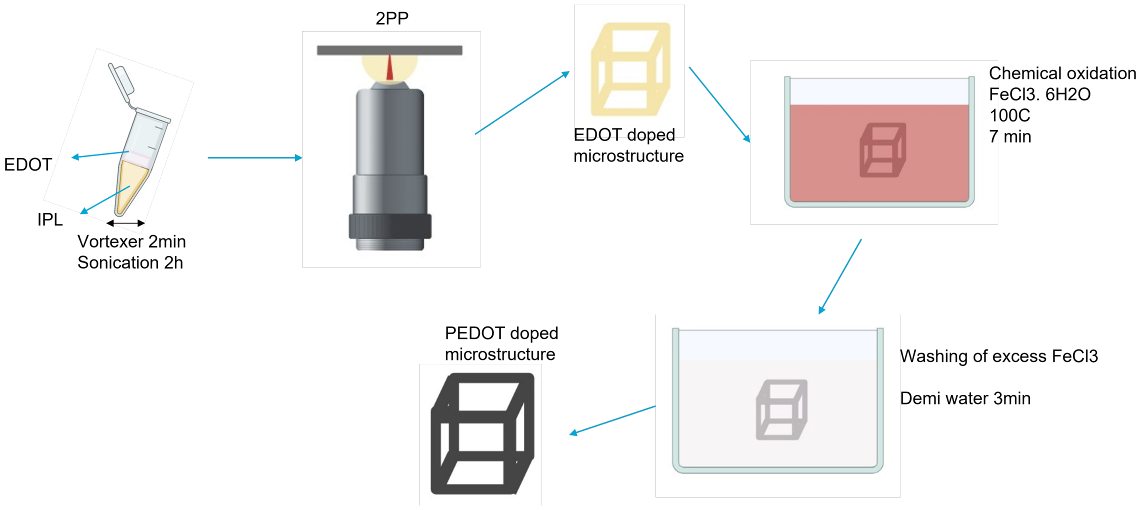

Figure 4.1: Schematic showing fabrication process of PEDOT-doped microstructure

Three blends of IP-L/ EDOT were prepared 5, 10, 15% and undoped IP-L for control. The blends were made in a total of 800 μL for each concentration, IP L was siphoned from the bottle using a 1 mL syringe and EDOT using a 200 μL pipette into a 1.5 mL plastic vial. First, It is coarsely mixed by shaking it on a vortexer for 2 min and then by sonication for two hours. The microstructures are using 2PP, which will be explained in the following section4.4, the development protocol for 2PP is 10 min in PGMEA bath and 3 min IPA followed by 30s in Novec 7100 and left to air dry.

4.2.1. Oxidative polymerisation

The oxidative polymerization of EDOT is done using $FeCl_3.6H_2O$ in a melt of undiluted salt at 70 °C for 7 min [18], the temperature is regulated by Stuart SCT1 temperature controller. A sealed glass tube with mineral oil is used as a barrier between the probe and the chemical bath to protect the probe from corrosion. A 3 min immersion in demi water is used to wash away the salt from the microstructure and substrate, the substrate is rinsed with IPA and placed in Dimethyl sulfoxide (DMSO) for 5 min for solvent treatment, and once again, it is rinsed with IPA to wash away the DMSO and immersed in Novec 7100 for 30s and left to air dry.

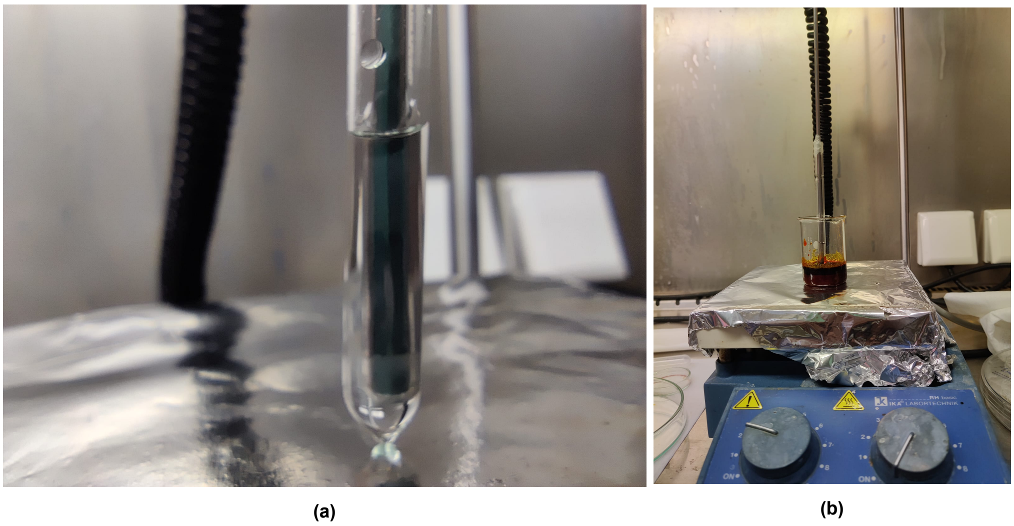
(a)
(b)

Figure 4.2: The setup for controlled temperature chemical polymerization, (a) The protective glass tube with mineral oil and thermal probe, (b) Placement of probe in a chemical bath to regulate temperature

Initial experiments were conducted using a hot plate without temperature regulation. This resulted in temperature fluctuations ranging from 60°C to 80°C. Subsequently, a controlled temperature setup was employed, which produced distinct changes in electrical conductivity, as indicated in Table 5.4. The setup for the controlled temperature chemical polymerization process is depicted in Figure 4.2.

4.3. Design of microstructures

All the CAD files and designs were made using Solidworks, and different designs were used based on the characterization needed. A 30 μm cube, a pedestal for mechanical characterisation, a dog bone design for electrical characterisation, a 3D cage matrix for pore size optimization and a final design.

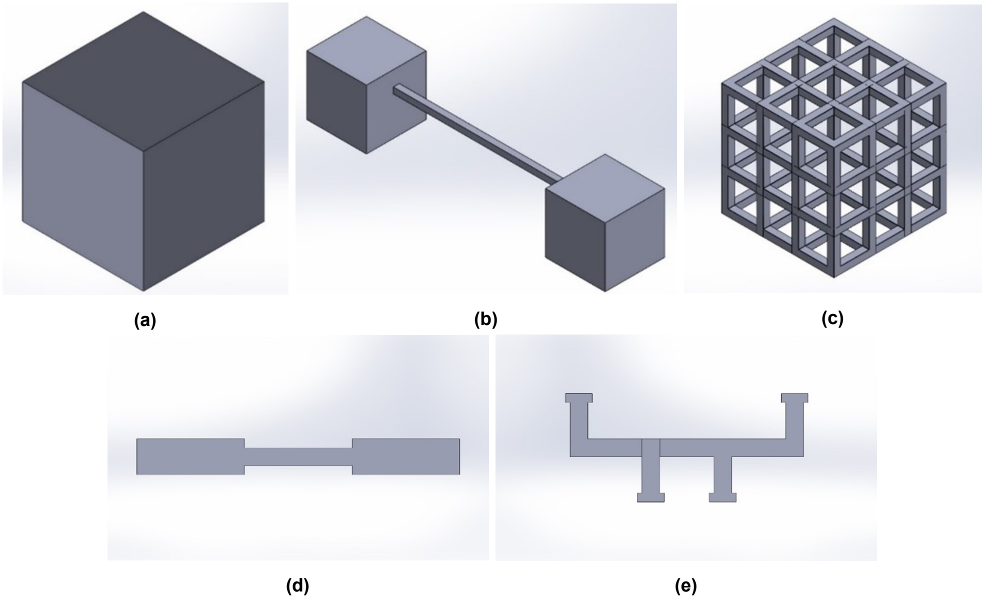

(a) (b) (c)

(d) (e)

Figure 4.3: CAD designs for (a) Cubic pedestal of 30x30x30 μm^3, (b) Beam for morphological analysis, (c) 3D Cage matrix, (d) Two-point measurement microstructure, (e) Four-point measurement microstructure

4.4. Two photon polymerization

The process of 2PP is a form of direct laser writing (DLW) currently used as a light-assisted technique in additive manufacturing (AM). This method is distinguished from other AM methodologies by its unparalleled resolution, which has the potential to achieve feature sizes as small as 200 nm in all three spatial dimensions. With various viable materials, 2PP is an exemplary tool for different micro-precision-oriented domains, including tissue engineering, microelectromechanical systems (MEMS), microfluidics, and micro-optics. The materials suitable for 2PP include acrylate and epoxy-based polymers, composites of metals and polymers, resins compatible with biological contexts, and hydrogels. This technological framework allows for flexible structural design, with dynamic changes in material properties such as rigidity, refractive index, and thermal conductivity. It is important to note that one of the limitations associated with this approach is the considerable duration of the printing process [77]. In this thesis, the Photonic Professional GT+ setup developed by Nanoscribe GmbH is used for the 2PP printing procedure.

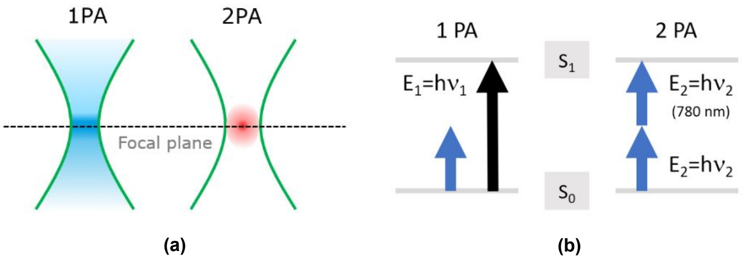

Figure 4.4: Comparison between one and two-photon absorption. (a) Voxel visualization of 1PP and 2PP, (b) One and two-photon absorption, where an excited state S1 is reached that triggers polymerization[11]

The femtosecond pulsed laser beam triggers the 2PP process by absorbing two near-infrared photons within a highly intense light environment. This laser is focused into a resin medium, where 2PP occurs exclusively within the focal spot. This activation occurs only when light intensity exceeds a critical polymerization threshold, as shown in Figure 4.5. This concept is graphically represented in Figure 4.4a. The minimal 3D printable unit is a voxel, similar to a 2D pixel, with a diameter ranging from 0.2 to 1.2 μm. This technique creates structures of multiple voxels and printed lines by manipulating the laser's focus in all three dimensions. This technology enables the production of structures with small, medium, and large feature sizes in both 3D and 2D patterns.

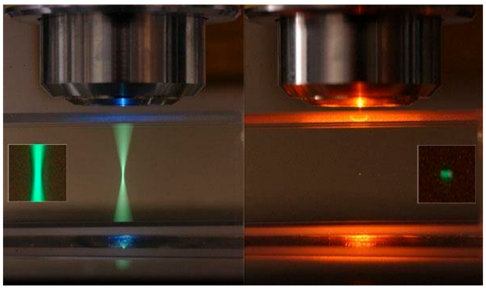

Figure 4.5: Imaging fluorescence from one and two-photon absorption processes.[78]

The intricate polymerisation process in negative-tone resins is elucidated through a tripartite free radical polymerization mechanism [11]. The process involves three distinct phases. First, in the initiation phase, the photoresist is irradiated by a laser beam, which initiates the activation of the photo-initiator and leads to the emergence of free radicals. These radicals engage with monomers in the propagation phase, driving the polymerization process forward. Finally, termination phase, the polymerization process culminates, where the long-chain monomer radicals generated in the preceding steps amalgamate with other radicals or initiators, leading to the termination of the reaction.

The procedure for fabricating the designed structure entails a series of systematic steps. The digital 3D model is first imported into computer-assisted manufacturing (CAM) software, DeScribe (from Nanoscribe), to render it ready for manufacturing. This model is divided into thin slices, typically ranging from 0.1 μm to 5 μm, along the z-axis. Each of these layers is subsequently partitioned into smaller segments along either the x- or y-axis, a hatching procedure where the distances encompass a range of 0.2 μm to 1 μm. The final stage involves the physical fabrication of the design through 3D printing. This fabrication is achieved by successively tracing the laser along the hatching lines of each layer, thus fabricating the model.

After the fabrication process, it is necessary to perform a sequence of post-processing steps. This step is significant when using the structures in combination with cell cultures, as unpolymerized photoresin can be harmful. The model is usually washed thoroughly with a developing solution or developer, such as PGMEA and IPA. Also, post-curing using UV-light or temperature models can generate additional polymer cross-linking. Depending on the dosage and temperature, this procedure will cause shrinking, which is typically uniform. This may be accommodated by scaling up the digital model of the structure [11].

Print Sets

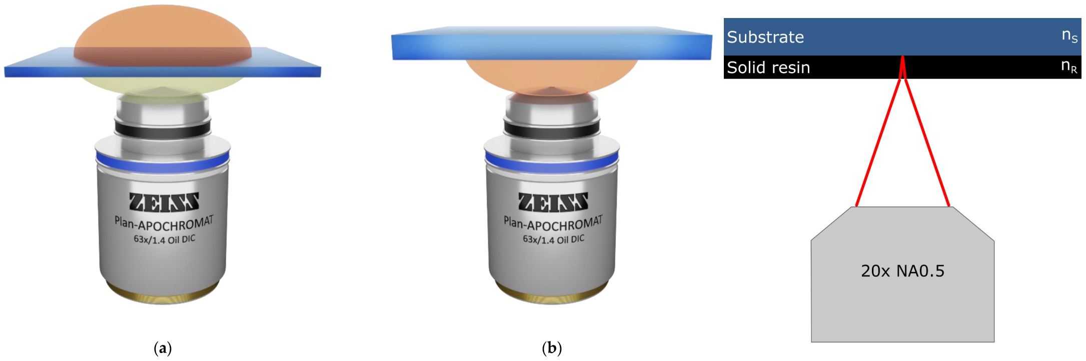

Figure 4.6: Schematic representation of the setup for printing in (a) oil immersion and (b) DiLL configuration, (c) solid-resin/Air 20x objective [79]

In PPGT+ Nanoscribe, there are two different 2PP configurations to choose from. The first is the oil immersion configuration (shown in Figure 4.6a), where the objective lens (either 63x or 25x) is immersed in an oil droplet under the borosilicate substrate. The photoresist is deposited on top of the substrate, and the laser passes through the oil, substrate and finally interacts with the photoresist. This configuration uses oil immersion to improve the resolution of the objective, with the translucent substrate playing a role in the structure's construction. In contrast, the dip-in laser lithography (DiLL) configuration (shown in Figure 4.6b) involves submerging the objective directly into the resin. This design choice reduces the number of interfaces and facilitates the creation of taller objects that can reach a few millimetres in height. The DiLL configuration supports 10x, 25x, and 63x objectives. It is worth noting that when printing on AZ 4562, a solid resin post-baking, the Air/2PP configuration is used with a 20x objective (shown in Figure 4.6c).

The process of creating microstructures involves utilizing 2PP. Different slicing and hatching dimensions are used for the 63x oil mode and the 25x oil/DiLL configuration. A stitching methodology is employed for larger structures with an overlap of 5µm and a shear angle of 50°.

4.5. Scanning electron microscopy

The qualitative and quantitative analyses of the printed microstructures are conducted using the Scanning Electron Microscope (SEM) model JOEL 6010LA. To minimize electron charging, all samples underwent sputter coating with a layer of gold at a current of 20 mA for 30 seconds. This coating process was essential to enhance the accuracy of the acquired images. To ensure precise measurements, images were captured from two distinct angles, 0° and 85°.

4.6. Optical microscopy

Two microscopes were used during the fabrication process. The Motic Elite compound microscope verified the accuracy and integrity of the printed structures, while the Keyence Digital Microscope VHX-6000 captured high-quality images and provided superior resolution. Image documentation occurred at two critical points, following the initial printing stage and after the oxidative polymerization process.

4.7. Mechanical Characterisation

The Youngs modulus of the blend was experimentally measured by performing a two-way compression test on a 30x30x30 um3 pedestal using the Femtotools FT-NMT03 Nanomechanical Testing System. A micro force sensing probe FT-S200000 is used, with a force range ±2 N and probe tip cross-section of 50 x 50 μm^2.

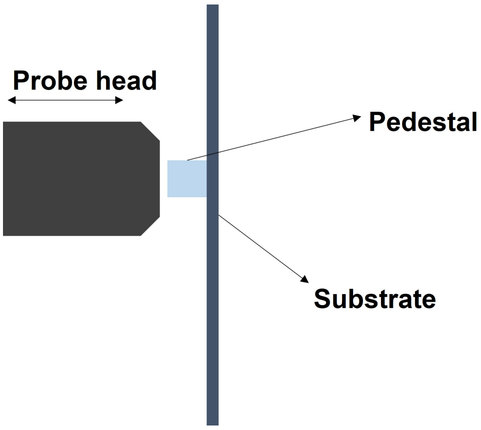

Figure 4.7: Schematic showing the compression probe on a 2PP printed pedestal

4.8. Fabrication of Gold Electrodes

To characterise the microstructures printed without any stitching, it is crucial to have electrodes fabricated with a maximum gap of 350 μm. The microstructures are fabricated directly onto gold electrodes to characterize their electrical properties for the final application. The gold electrodes are fabricated through maskless lithography using the 2PP technique. A target layer thickness of 10 µm is achieved by spin-coating the photoresist, specifically AZ 4562, on the silicon substrate, involving two stages, 5 seconds at 540 rpm and 30 seconds at 2080 rpm. After being baked at 110°C for 5 minutes, it is left in the air for at least 20 minutes. The structures are printed via 2PP using a 20x air objective with laser power set at 45 mW and a scan speed of 10 mm/s. The hatching distance measures 0.8 µm, and slicing is conducted at 3 µm. The developed photoresist undergoes immersion in a diluted solution of the AZ 400K developer at a ratio of 1:3 in demi water for 8 minutes. Subsequent steps encompass rinsing the samples with demi water and employing compressed air for blow-drying.

A sputtering technique is employed for the deposition of gold, involving a current of 40 mA and a deposition duration of 60 seconds, with the sample positioned approximately 25 mm from the source. Subsequently, a process of gold removal and lift-off is executed, which entails utilizing DMSO at a temperature of 60°C for 30 minutes. These comprehensive steps collectively serve to fabricate the gold electrodes.

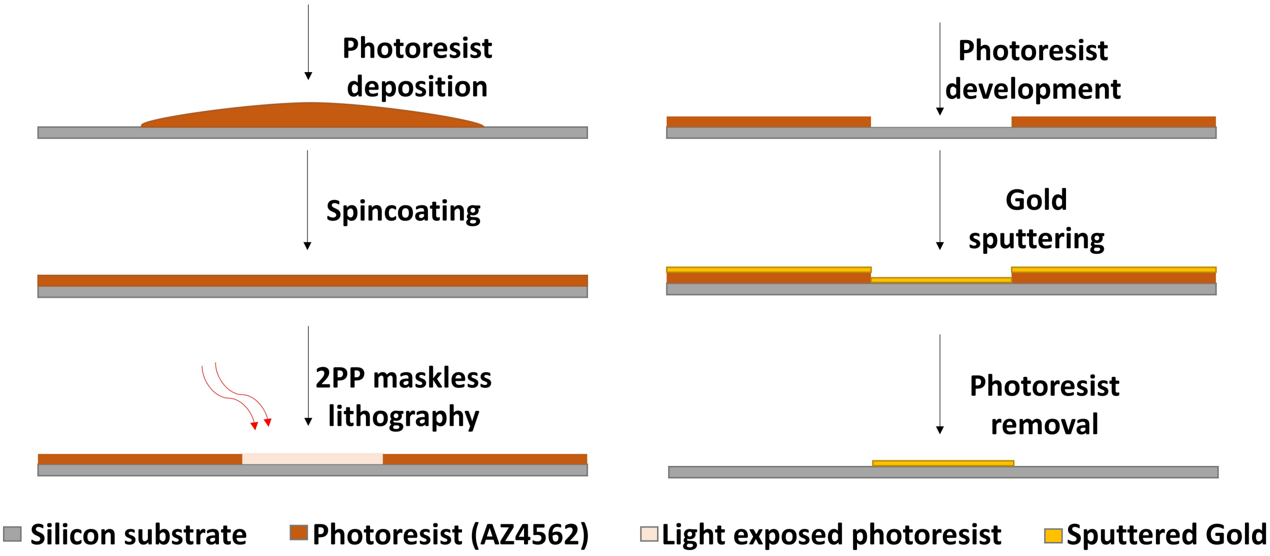

Figure 4.8: Process of fabricating gold electrodes using maskless lithography

4.9. Electrical Characterization

The characterisation of microstructure conductivity is undertaken within the Süss MicroTec probe station situated in a Faraday cage to mitigate external electromagnetic interference. Both 2-point and 4-point measurements are conducted on structures deliberately designed to accommodate these specific measurement techniques.

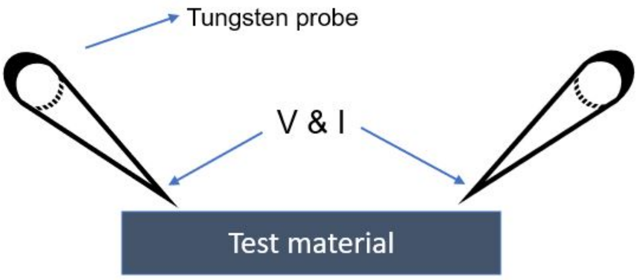

(a) Schematic of probe placement: 2- point configuration

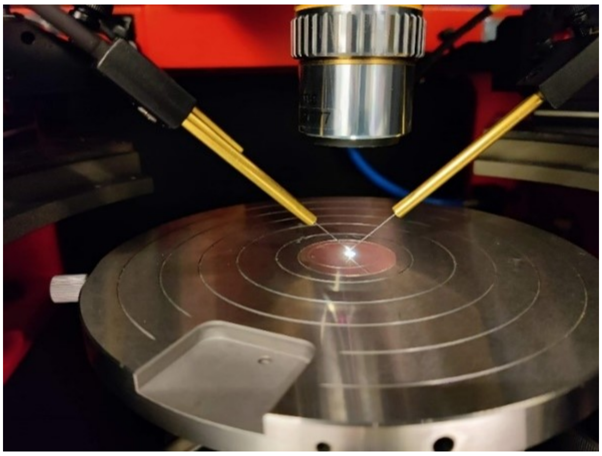

(b) SUSS Mictrotec Probestation: 2-point configuration

Figure 4.9: Electrical characterisation setup

A layer of silver paste is meticulously applied using a brush to establish an ohmic contact between the 2D structure and the tungsten needle probe. This manual application necessitates the structural dimensions to be adequately sized for naked-eye visibility. Consequently, creating multiple prints becomes imperative, as the print field attainable with a 25x objective is limited to 380 µm. A distinctive design strategy is adopted to encompass the region covered by the silver paste accurately. The structure's design is modified to be wider at both ends, forming a dog bone-like shape, which facilitates two-point measurements.

The 2-point probe method is employed within this measurement paradigm, wherein current and voltage are sensed through the same probes. This approach, though straightforward for assessing material conductivity, is not devoid of shortcomings. An inherent error emerges due to contact resistance from the interface between the electrode and the probe. Despite this challenge, the two-point probe method remains a valuable tool, offering simplicity in conductivity measurement albeit necessitating careful consideration of contact resistance-induced inaccuracies.

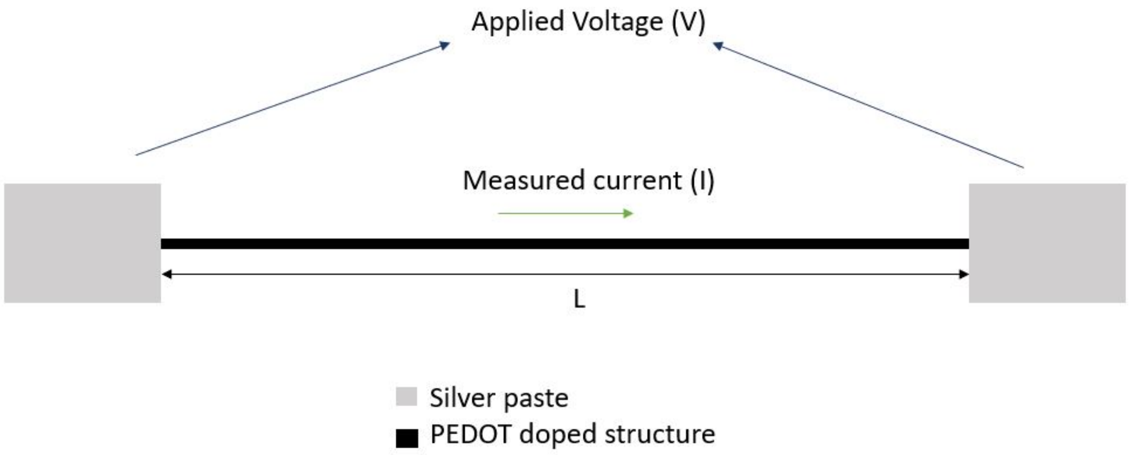

Figure 4.10: Schematic of 2-point electrical characterization

Four-point measurements are a precise and reliable technique for evaluating microstructure conductivity. This method directs current through input and output probes while a pair senses voltage drop. The methodology ensures accurate and consistent results by eliminating contact resistance at the electrode-probe interface, assuming uniform electrical properties and ohmic electrodes.

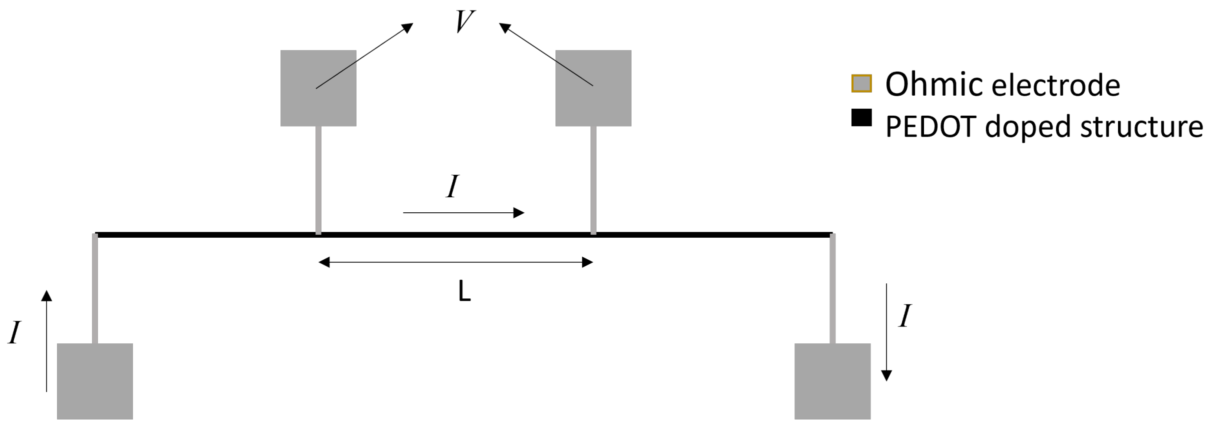

Figure 4.11: Schematic of 4-point electrical characterization

5

Results and Discussion

5.1. Fabrication of Microstructures

The fabrication process starts with creating a blend of EDOT and IP-L. Mixing protocol follows an established methodology. Initially, the printing uses a 63x objective in an oil immersion configuration to protect the lens. Optimal printing parameters are identified through systematic dose tests as shown in Figure B.2.

SEM imaging reveals a phenomenon called ”shadowing” that affects the printing process when using oil mode. Shadowing occurs when the increasing height of a structure interacts with the underlying printed structure, causing defocusing and a decrease in laser power, resulting in deviations from the original design parameters. This phenomenon is depicted in Figure 5.1.

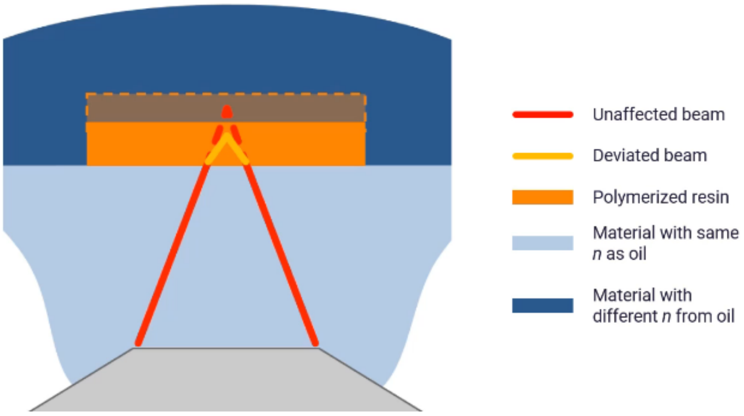

Figure 5.1: Shadowing in Oil mode due to bottom layers

The Pspowerslope command in DeScribe software plays a pivotal role in dynamically elevating laser power as structure height advances. The command translates design and printing parameters to the system using the equation:

Laser Power at a given height (h) = Initial Laser power x (1 + powerslope x h of the specific slice).

A parameter value of 0.02 is optimal based on a sweep test. The visual comparison in Figure 5.2 effectively highlights the discernible distinctions between the outcomes of printing activities executed with the integration of the power slope command and those undertaken without it. This substantiates the substantial impact of the powerslope strategy in mitigating the shadowing phenomenon and enhancing the reliability of the printing process.

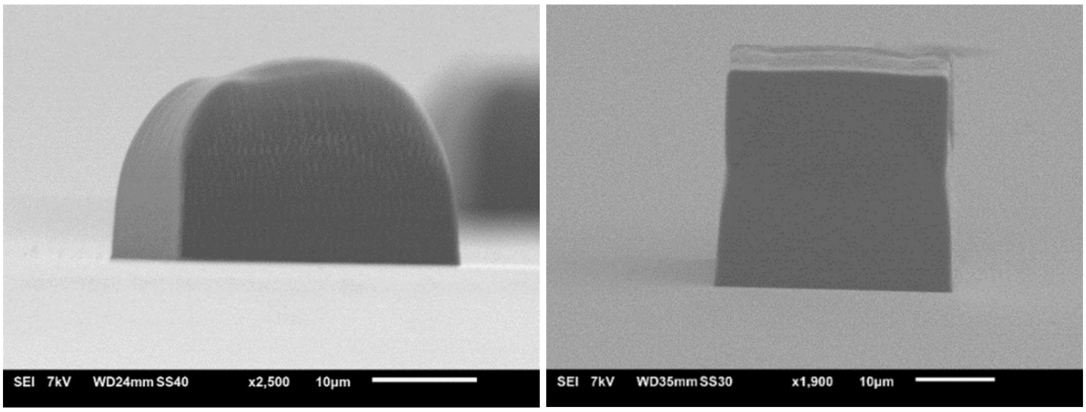

(a) (b)

Figure 5.2: Effect of powerslope in 63x Oil configuration printed with, (a) Constant power, (b) Powerslope of 0.02

During the printing process of higher structures using the powerslope function with a 63x objective, the structural integrity of the printed entities was compromised, resulting in collapse. Additional insights about fabrication with the 63x oil mode can be found in Appendix B.

In response to this challenge, an alternative approach was to print these structures using a 25x objective in oil immersion. Although the shadowing phenomenon persisted, this approach required an adaptation due to inherent discrepancies. An inconsistency in locating the interface emerged due to the IP-L resin needing to be designed for the 25x Oil configuration. The 25x objective requires a minimum refractive index disparity of 0.1, which is problematic as the refractive index values for IP-L and borosilicate glass are 1.477 and 1.517, respectively [11]. This mismatch in refractive indices between the 25x objective and IP-L within the oil mode necessitated a transition to the 25x Dip-in Laser Lithography (DiLL) mode.

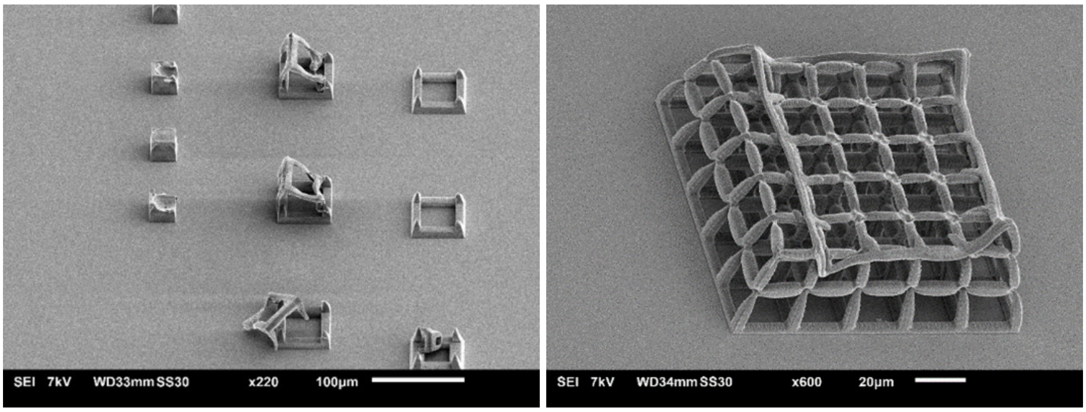

(a) (b)

Figure 5.3: SEM images of 10% EDOT doped 3D microstructures printed Powerslope of 0.02 with, (a) 63x objective, (b) 25x objective

To check the hypothesis of whether this approach is capable of producing electrically conductive microstructures, lines of 5 mm length, 200 μm width, and 15 μm height were printed in 25x oil and oxidised for electrical characterisation. The colour change of the microstructures obtains visual proof of the process. They go from near transparent to a dark colour which signifies that PEDOT formation is successful. This can be seen in the optical microscopic images in Figure 5.4.

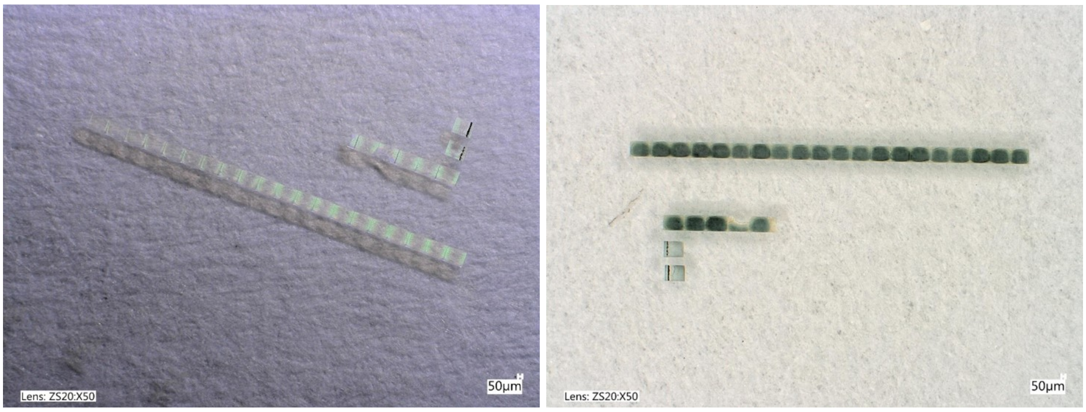

(a) (b)

Figure 5.4: Optical microscope image of 10% EDOT doped line of length 5 mm, (a) 2PP printed, (b) After oxidative polymerisation

The printing process now exclusively uses the 25x DiLL mode to ensure consistency. A cleaning test on a glass substrate confirms the resin blend's compatibility with the lens, ensuring no residue remains after cleansing.

A structural configuration referred to as a dog bone design has been implemented to expedite the production of samples earmarked for electrical characterisation. However, microexplosions are localised explosions caused by overexposure to the laser due to the stitching process, as visually depicted in Figure 5.5. Stitching is performed to print continuous long structures, and each new section starts with 5 μm overlaps to ensure connectivity. The laser power and scanning speed are calibrated to reduce this phenomenon. This calibrated set of parameters is now being systematically employed to fabricate all pertinent structures, and the adjusted laser parameters are listed in Table 5.1.

Resin	Laser power (mW)	Scan speed (mm/s)
IPL	30	60
5% EDOT	30	60
10% EDOT	30	60
15% EDOT	35	40

Table 5.1: Optimised printing parameter

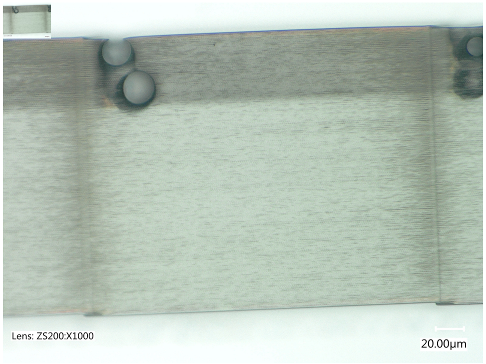

Figure 5.5: Microexplosion at stitch for 10% PEDOT

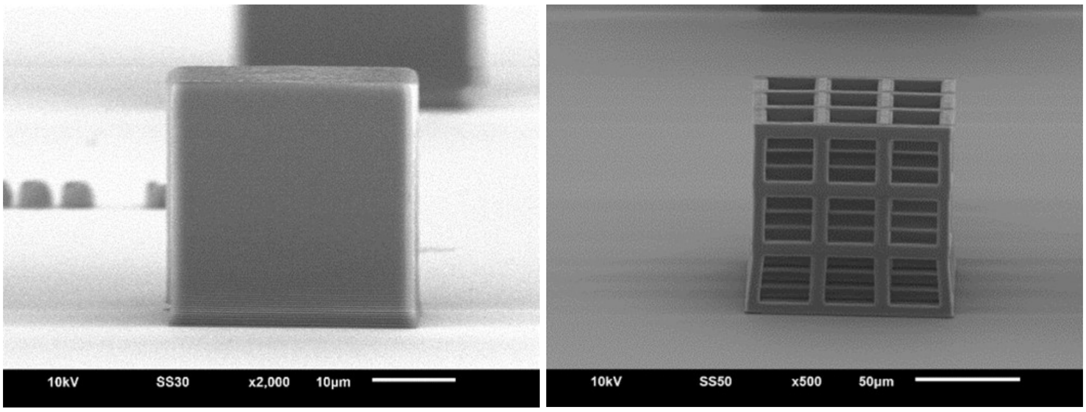

(a) (b)

Figure 5.6: 3D microstructures printed in 25x DiLL mode, (a) pedestal, (b) 3D Cage

The provided images below illustrate distinct stages: the control sample (Figure 5.7), the doped prints (Figure 5.8), and the doped prints subjected to oxidative polymerization (Figure 5.9). An important observation is that higher doping levels make deformations during the oxidative polymerization process more pronounced. Additionally, there is a noticeable trend of the colour change becoming progressively darker as the doping level increases.

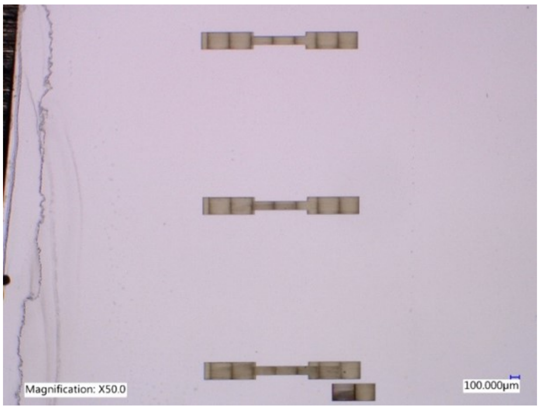

Figure 5.7: Dog bone structure IP L (control)

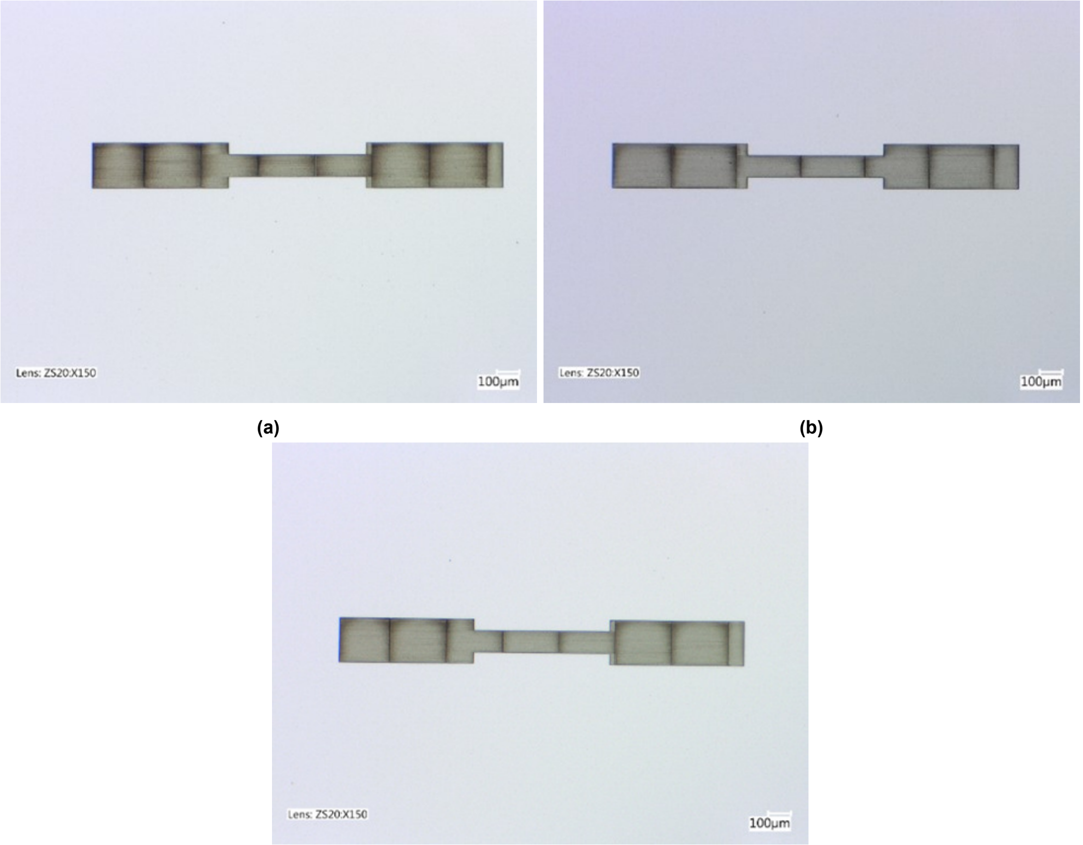

(a) **(b)**

(c)

Figure 5.8: Optical microscope images of Dog bone structure doped IP-L, (a) 5% EDOT, (b) 10% EDOT, (c) 15% EDOT

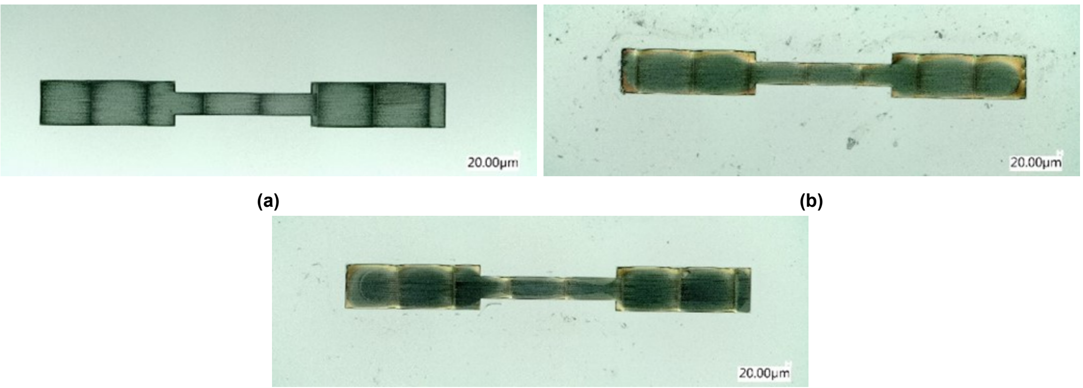

(a) **(b)**

(c)

Figure 5.9: Optical microscope images of Dog bone structure doped IP-L after oxidative polymerisation, (a) 5% EDOT, (b) 10% EDOT, (c) 15% EDOT. The change in colour indicates the formation of PEDOT in the microstructures

5.1.1. Morphology

A series of cross-section beams were fabricated in control and doped resins with 1x1 and 2x2 μm² measurements. The length of the beams ranged from 5 to 30 μm, with a 25x objective. Through observation, it was noted that as beam length increased, the thickness of the printed beam decreased. This decrease in thickness was due to shrinkage, which in turn, was found to increase with higher doping levels. Figure 5.10 displays that the voxel size achievable with the 25x objective for the initial resin (IP-L) is 2.5 μm. However, the voxel size contracted to 0.626 μm post-shrinkage for a 15% EDOT doping level. Interestingly, the 15% EDOT doped resin, printed with a higher laser dosage, shows increased rigidity and resists collapsing compared to the 10% EDOT doped print. This highlights the impact of doping concentration and laser dosage on the structural integrity of printed microstructures.

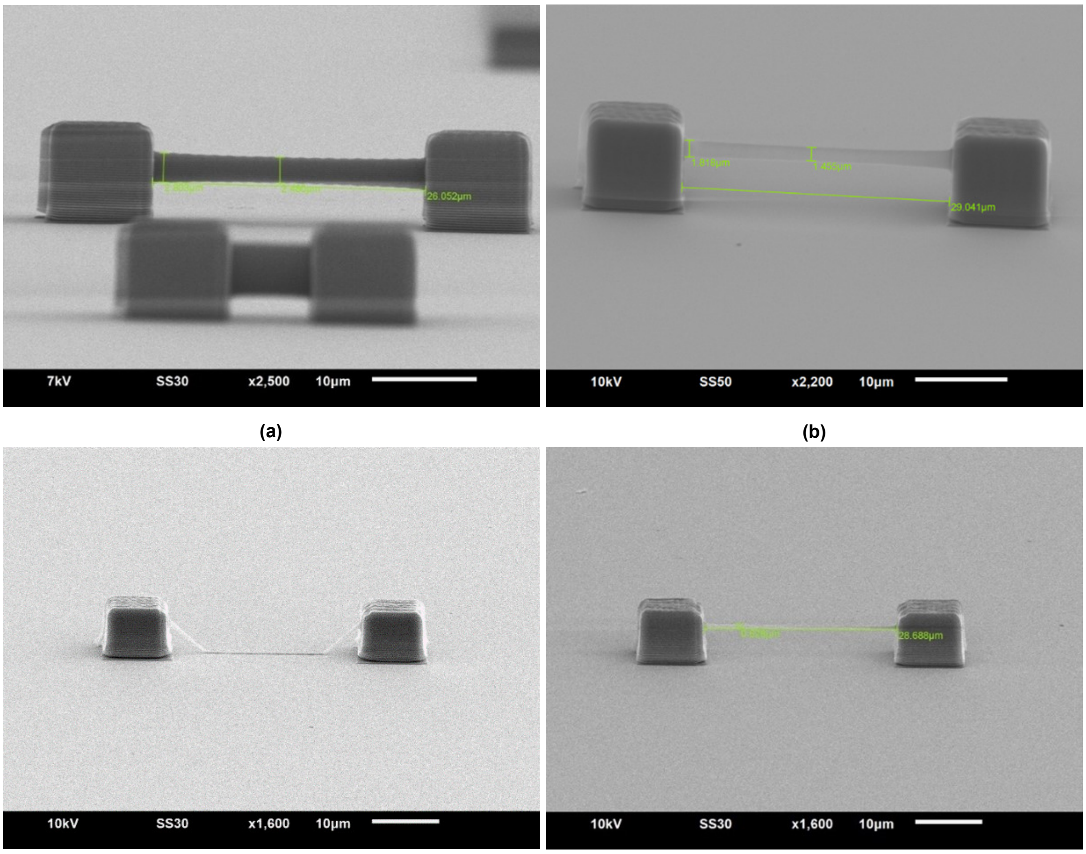

(a)

(b)

(c)

(d)

Figure 5.10: 30 μm beam with 1x1 μm^2 crosssection, (a) IP-L, (b) 5% EDOT, (c) 10% EDOT, (d) 15% PEDOT

5.1.2. Complex 3D structures

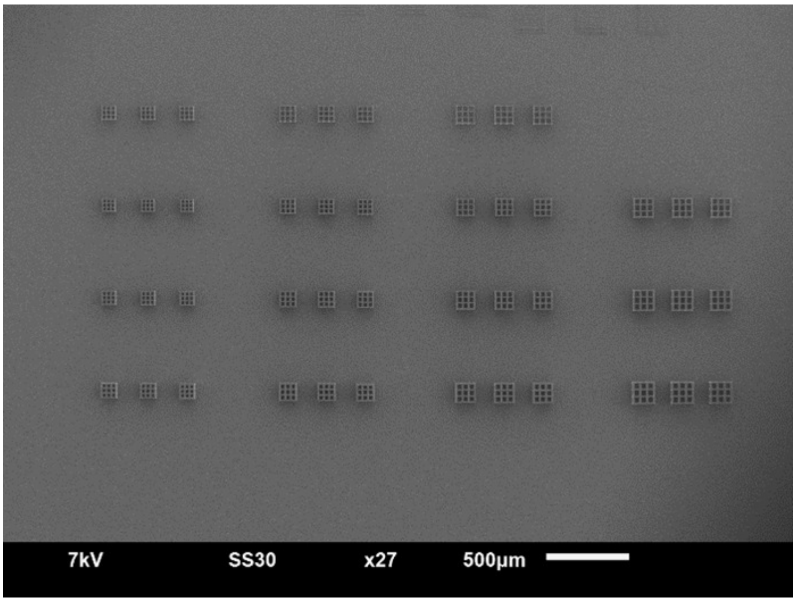

Figure 5.11: 3D cage array printed in IP-L with beam thickness 4 - 10 μm and pore size 20 - 35 μm

To evaluate its suitability for creating a 3D environment for cell culture, a 3D cage matrix design was executed through printing. This design encompassed pore sizes spanning from 20 to 35 µm and beam thicknesses ranging from 4 to 10 µm, as exemplified in Figure 5.11. SEM analysis reveals that at a 10% EDOT doping concentration, beam structures measuring 4 µm experienced collapse when encountering pore sizes of 25 µm and larger. When the doping level was increased to 15% EDOT, the beams deformed.

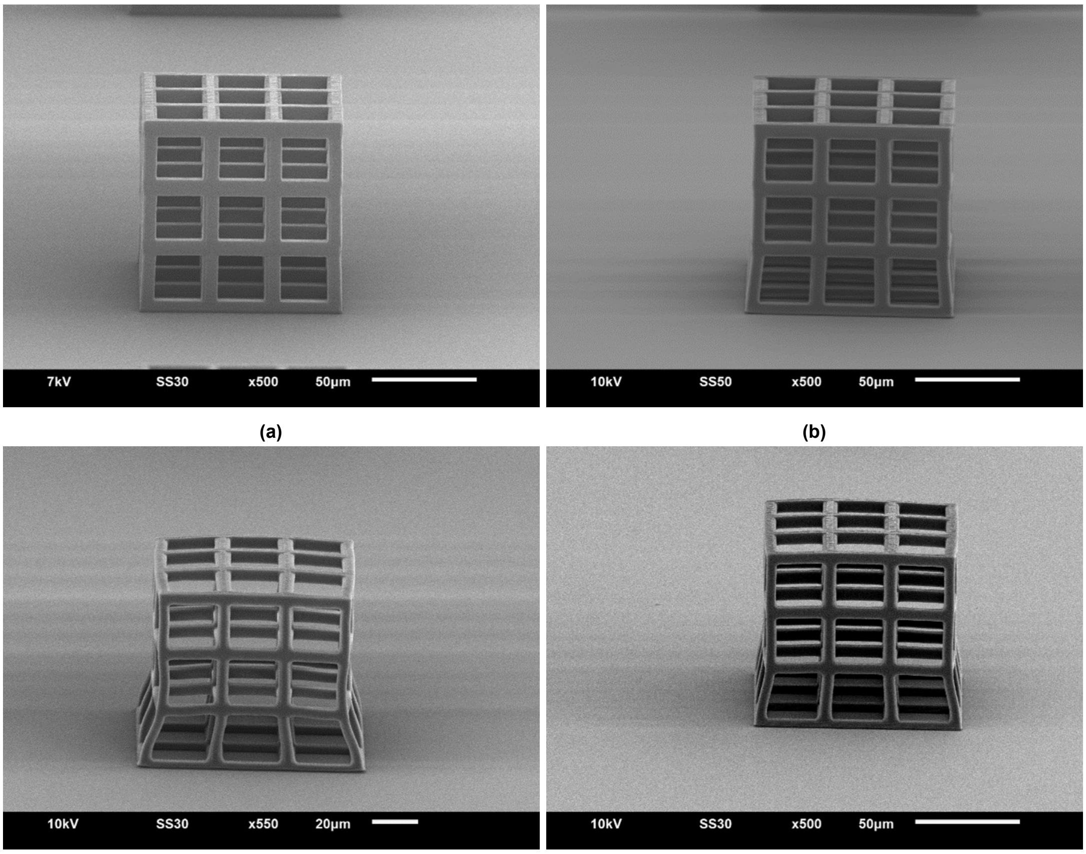

(a) (b)

(c) (d)

Figure 5.12: 3D Cages of $6\mu m$ beam thickness and $25\mu m$ pore size, (a) IP-L, (b) 5% EDOT, (c) 10% EDOT, (d) 15% EDOT

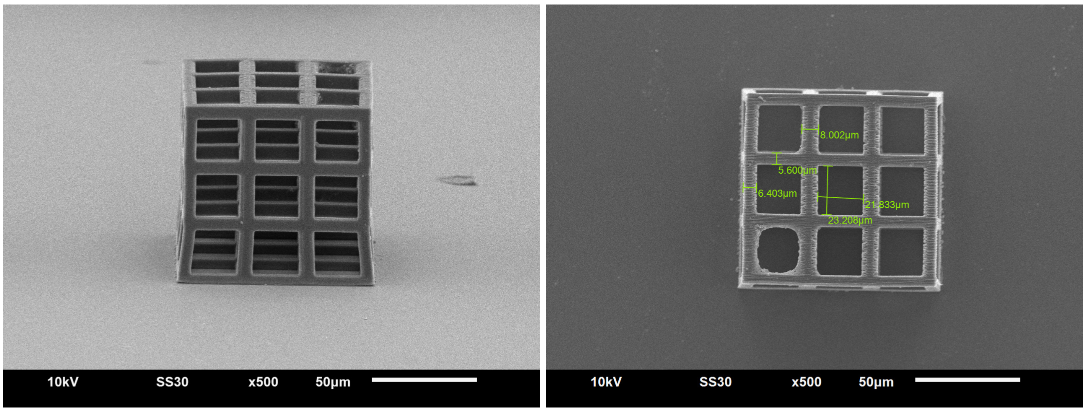

(a) (b)

Figure 5.13: 3D Cage of 6 μm beam thickness and 25 μm pore size for 5% PEDOT, (a) 3D view, (b) top view

Figure 5.13 shows a 3D cage structure after oxidative polymerisation. The structure is stable and blockage-free, but one of the pores has a noticeable residue build-up.

The pore size of approximately 22 µm, seen in Figure 5.14, is suitable for cell culture study, aligning well with the soma diameter of cells (around 20 µm). Increasing doping levels cause a shrinking of the overall structure. However, the beams in the central region display an increased thickness, possibly due to factors such as inertia within the Galvo mirror or heat-induced polymerisation. Though this might not impact cell growth, this deviation from design is worth noting.

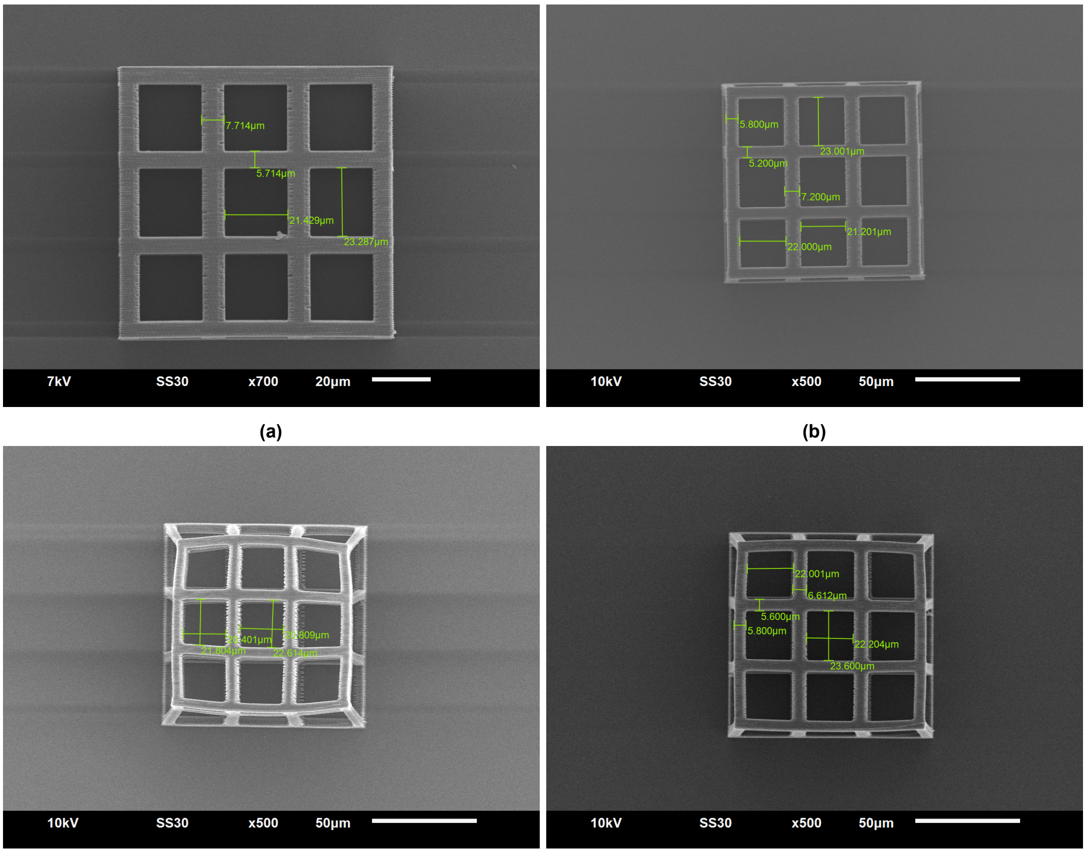

(a) (b)

(c) (d)

Figure 5.14: Top of 3D cages of 6 μm beam thickness and 25 μm pore size, (a) IP-L, (b) 5% EDOT, (c) 10% EDOT, (d) 15% EDOT

5.1.3. Fabrication of gold electrodes

After verifying the capability of fabricating 3D microstructures, the next step is to validate their electrical conductivity. For this, optimising the Gold pads fabrication process was iterative and involved several changes before the final working protocol, which is mentioned in the methodology, was reached. Initially, the printing parameters remained consistent: a hatching distance of 1μm, a slicing distance of 3 μm, a laser dosage of 45 mW, and a scanning speed of 10 mm/s. The results of this approach are illustrated in Figure 5.15, where it becomes evident that developmental inconsistency was observed. This observation occurred within the context of utilizing a 1:4 concentration of AZ 400K developer for 5 minutes, thereby highlighting the intricacies associated with this specific printing and development process.

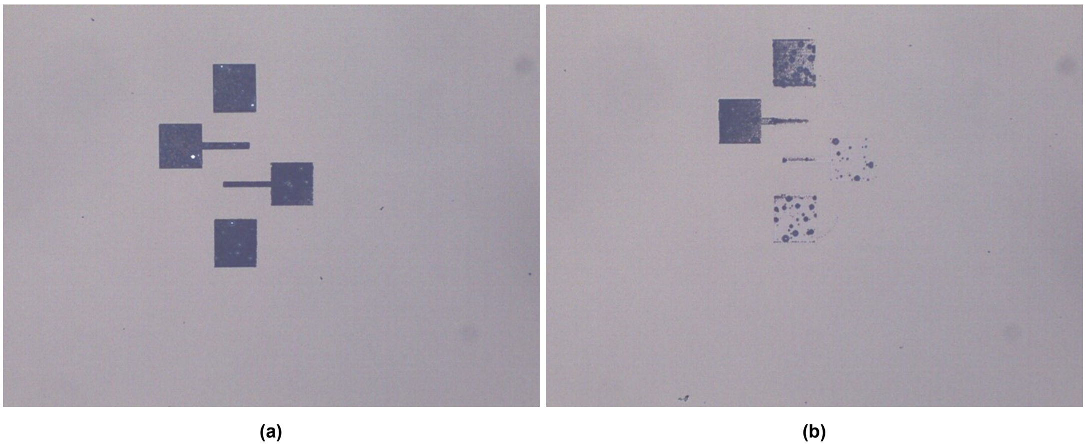
(a) (b)

Figure 5.15: Inconsistently developed AZ prints on the same substrate, (a) Fully developed, (b) Partially developed

Next, this developed substrate undergoes a sputter-coating process with Gold at a current of 40mA for 60 seconds. In the preliminary trials, acetone was selected as the removal agent. However, it was observed that despite a prolonged immersion of 16 hours in acetone (as depicted in Figure 5.16), the adhesion of the gold layer to the substrate persisted. Sonication was used to fasten this lift-off process, but it led to the complete delamination of the gold layer.

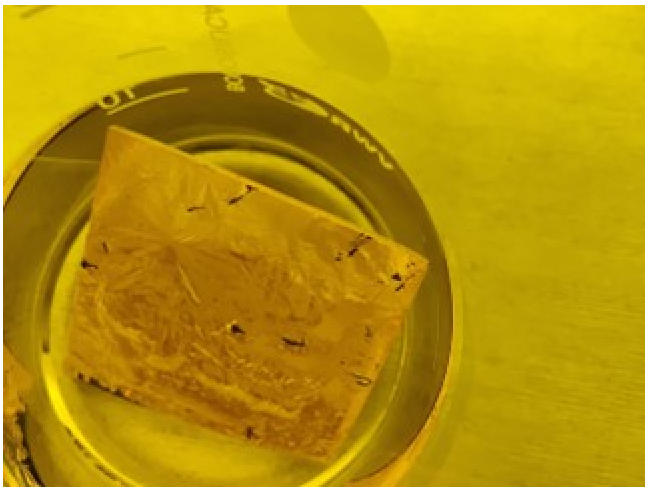

Figure 5.16: Gold coated AZ after 16h in Acetone

To pinpoint the exact stage that caused delamination, a Silicon substrate was given a coating of Gold and subsequently treated with Acetone for 5 minutes. Further, the substrate was subjected to sonication for 2 minutes. As a result, the layer of Gold separated from the substrate, as illustrated in Figure 5.17. This experiment was inconclusive.

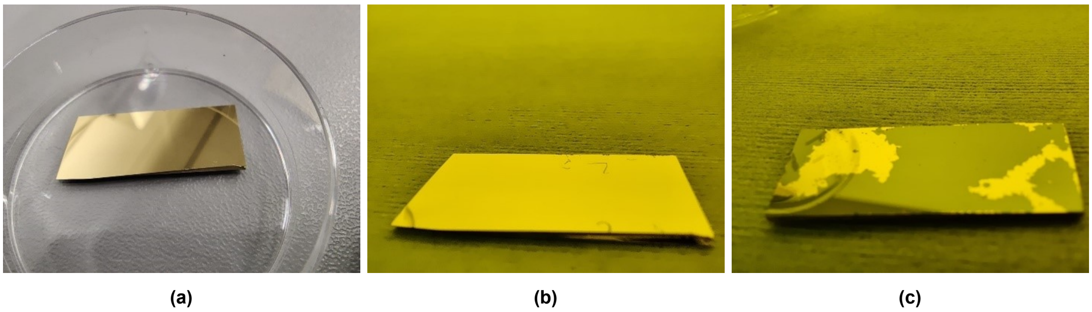
(a) (b) (c)

Figure 5.17: Lift-off test on Gold coated Silicon using Acetone, (a) Gold sputtered Silicon,(b) After 5 min in Acetone, (c) After 2 min of sonication

Further study in the literature found that acetone is unsuitable as a photoresist stripper because of its high vapour pressure, causing rapid drying. The fast evaporation of acetone can result in the unwanted redeposition of stripped photoresist onto the substrate, resulting in undesirable striations. To avoid this problem, alternative solvents with lower vapour pressures and slower evaporation rates are considered more appropriate for precise and controlled photoresist removal, as reported by Microchemicals.eu.

In subsequent trials, dimethyl sulfoxide (DMSO) was used as a remover at 60° C. To address the issue of inconsistent prints, the hatching distance was reduced to 0.8 μm, the AZ 400K developer concentration was increased to a ratio of 1:3, and the development time was extended to 8 minutes. Figure 5.18 shows the results, including the microscopic image post-development, the outcomes after DMSO treatment, and subsequent 2-minute sonication.

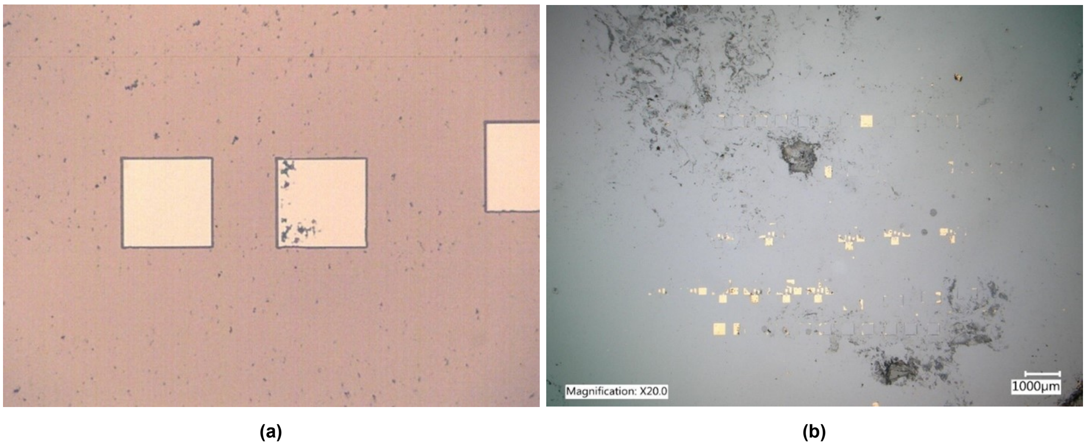

(a) (b)

Figure 5.18: Lift-off test using DMSO, (a) Developed AZ print, (b) 10 min DMSO and 2 min sonication

To facilitate solvent penetration into the baked photoresist and optimize the removal process, a negative slope is incorporated into the AZ print. This strategic alteration will enable the solvent to permeate the print walls more effectively. In sputtering, which lacks directionality, the deposition of gold occurs nondirectionally across all exposed surfaces within the plasma path. Consequently, there is a likelihood of gold being deposited on the AZ walls. A negative slope can mitigate this effect by reducing the surface area exposed to gold deposition.

The SEM images in Figure 5.19 visually compare the print walls with and without a negative slope of 45°. Notably, an observation is made regarding the formation of a protrusion at the interface between AZ and air. This phenomenon might be attributed to direct air exposure after baking, potentially influenced by the laser's initial defocusing on the initial AZ layers as the printing process commences from the Silicon-AZ interface. Despite this anomaly, its implications remain unexplored, as no discernible impact on the electrode fabrication process is established.

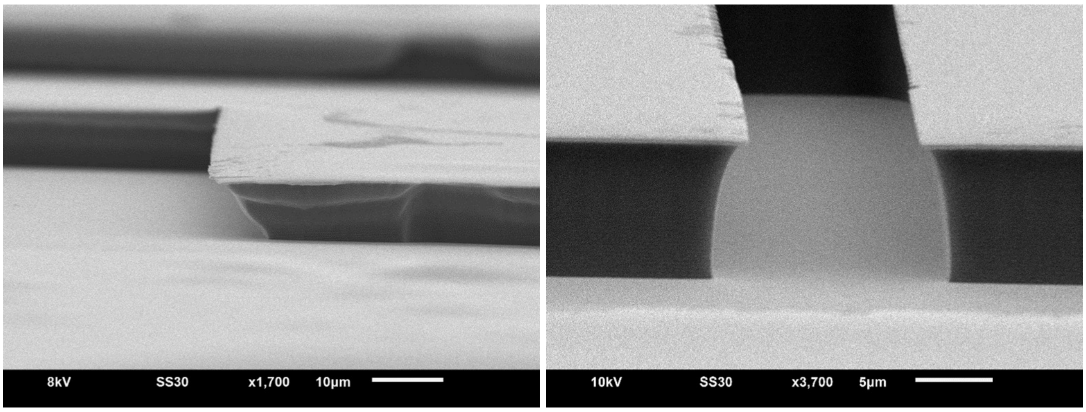

(a)

(b)

Figure 5.19: SEM images of developed AZ prints with (a) 45° Negative slope, (b) No slope in design

After the development process, the resulting sample is sputter-coated with gold. Dome-like structures in the centre of exposed areas are observed (Figure 5.20), possibly due to poor adhesion between the gold layer and underlying silicon.

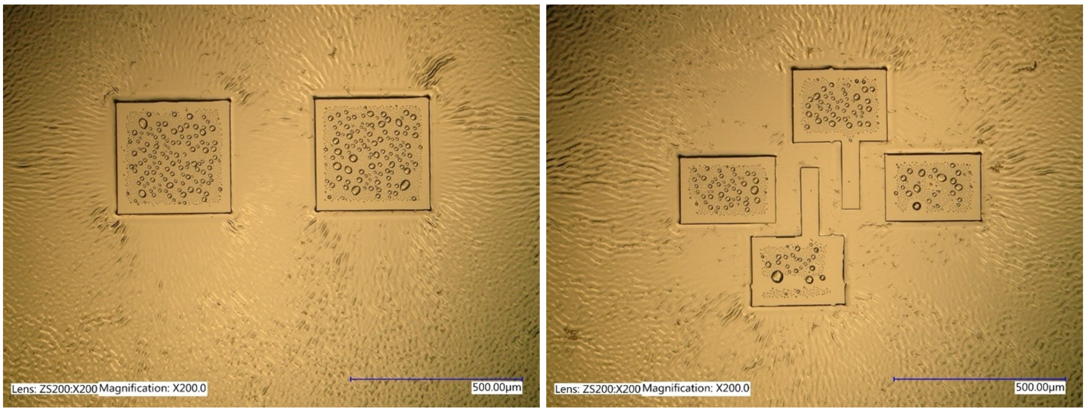

(a)

(b)

Figure 5.20: Gold sputtered on developed AZ prints, (a) 2-point probe pads, (b) 4-point probe pads

After sputtering, the revised lift-off procedure eliminates the AZ layer and excessive gold deposition. This procedure involves immersing the substrate in DMSO at 60° C for 30 minutes, with the substrate securely held within a metal holder. Subsequently, the substrate is agitated within DMSO until any loosely adhered gold layer detaches from the substrate. Any residual DMSO on the substrate is then removed through a subsequent rinsing step utilizing acetone. The substrate is then left to air-dry. Figure 5.21 shows the two and four-point electrodes fabricated with this protocol. Next is printing on these deposited gold electrodes.

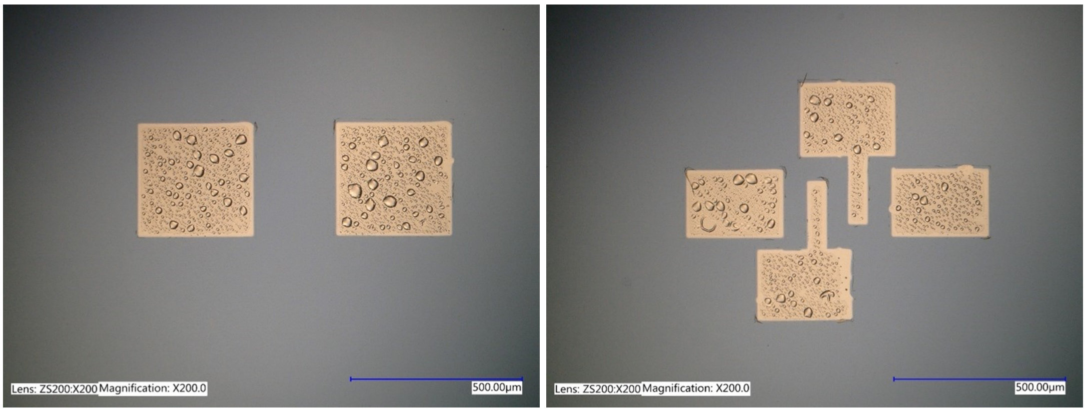

(a) (b)

Figure 5.21: Gold electrodes after lift-off process, (a) 2-point probe pads, (b) 4-point probe pads

5.1.4. 2PP printing on Gold electrodes

It is known that laser beams can undergo reflection when incident upon polished substrates and surfaces with reflective coatings, as documented in the literature [11]. The visual representation below illustrates the laser beam's trajectory and the voxel's positioning after the reflection, as demonstrated in Figure 5.22. This phenomenon engenders a localized augmentation in laser power, resulting in microexplosions. To avoid this overexposure near the surface, the base layers of the structure are printed with a reduced laser dosage.

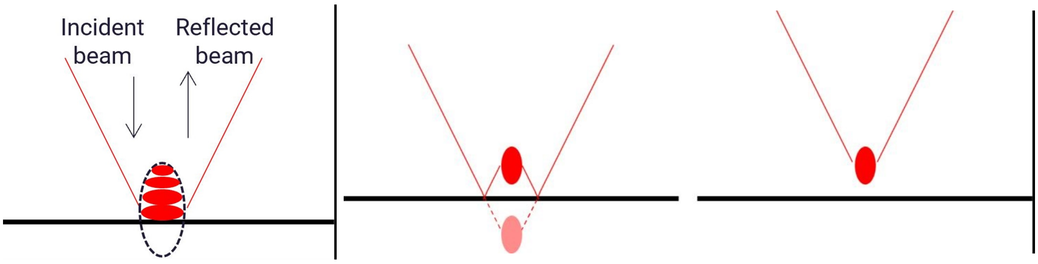

(a) (b)

Figure 5.22: illustration of laser reflection, (a) Voxel during reflection of laser, (b) The position of voxel after laser reflection, The voxel without reflection [11]

The optimal base layer count and corresponding printing parameters are determined through trial and error. Initially, a base layer count of 8 (equivalent to 5.6 μm) is employed. However, this configuration results in microexplosions in the print, particularly at the periphery of the gold pads. The specific laser power is set at 12.5 mW with a scan speed of 10 mm/s. These instances are shown in Figure 5.23, where the microexplosions near the edges of the gold pads are evident.

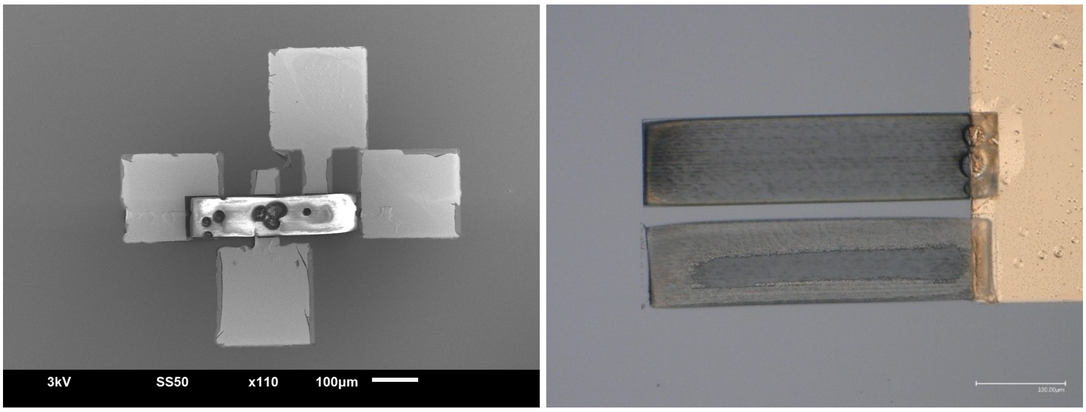

(a) SEM image of microexplosions in a 4-point sample

(b)

Figure 5.23: Microexplosions at the edge of the gold electrode, (a) SEM image of microexplosions in a 4-point sample, (b) Optical Microscope image of microexplosions in a 2-point sample

To minimize the occurrence of microexplosions, the base layer count has been increased to 10 (7 μm). It is important to note that the laser power and scan speed remain consistent to ensure accuracy. The positive outcome is that this strategy has significantly reduced microexplosions, as shown in Figure 5.24.

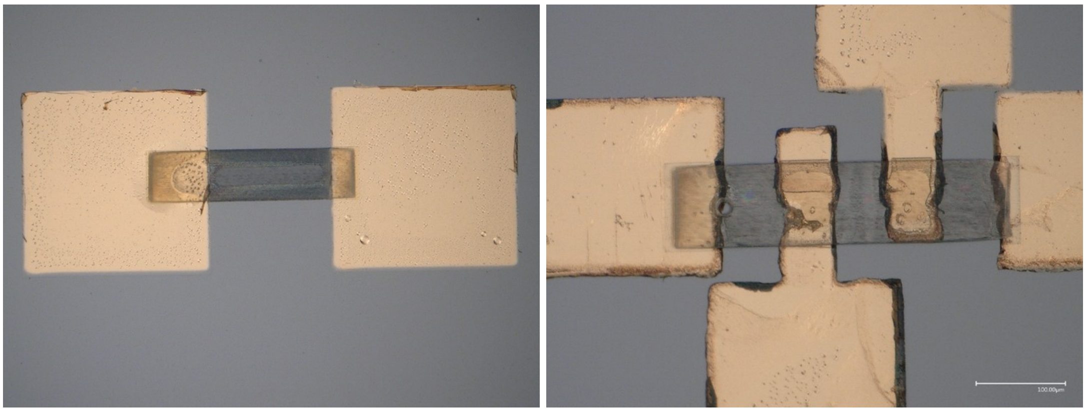

(a)

(b)

Figure 5.24: 2PP printed microstructures on gold pads for (a) 2-point probe, (b) 4-point probe

Upon conducting the oxidation process on the samples printed on gold electrodes, it is noticeable that the gold pads experience contraction and tearing as they come into contact with the microstructure. This observation can be seen in Figure 5.25.

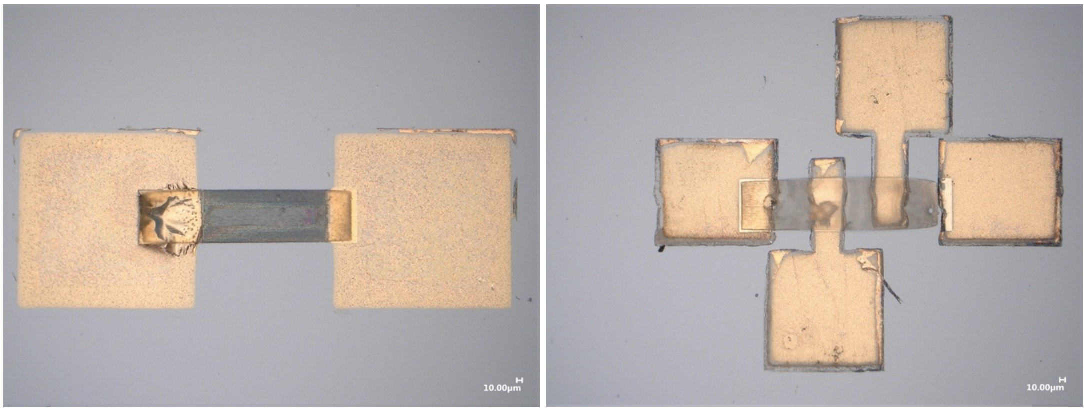

(a)

(b)

Figure 5.25: Oxidative polymerized 2PP printed microstructures on gold pads, (a) 2-point probe, (b) 4-point probe

The chemical polymerization process was successfully applied to samples with 10% EDOT and 15% EDOT doping levels. However, a noteworthy occurrence was witnessed during the chemical polymerization of samples with 5% doping. This failed sample is shown in Figure 5.26, all six consecutive substrates featuring the deposited gold pads experienced delamination. This complete delamination might be due to poor adhesion of Gold on Silicon, leftover AZ resin, or the MAPTMS on Silicon. The exact cause for this observation was indeterminant.

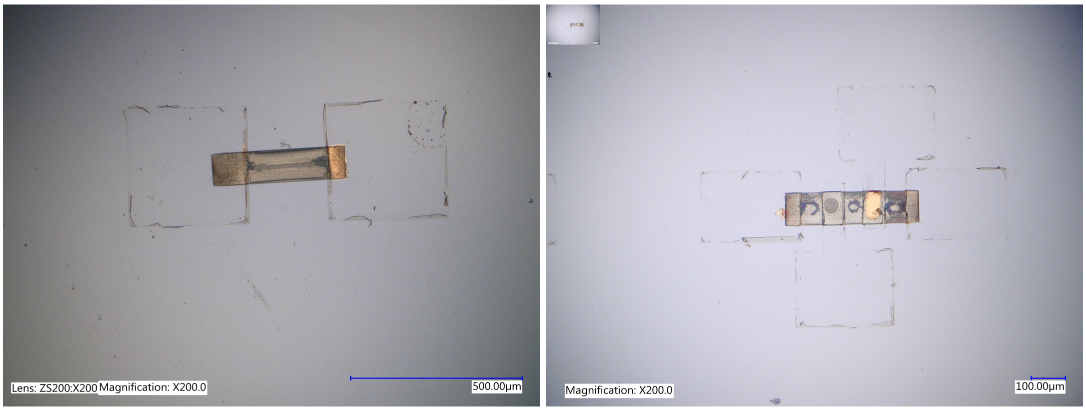

(a)

(b)

Figure 5.26: Delaminated gold pads for 5% doped microstructures, (a) 2-point probe, (b) 4-point probe

After conducting a thorough analysis using SEM, Figure 5.27, it was discovered that there were distinct differences in the microstructure morphology due to variations in laser dosages, base layers, and the main structure. Upon comparing the gold pad section to the area printed on silicon, it was observed that the former exhibited a greater thickness. This can be attributed to increased laser reflection on the gold surface, resulting in a more pronounced material polymerisation.

Furthermore, upon closer examination, it was noted that there was poor adhesion between the gold and 2PP printed structure. This suggests that there may be a need to modify the printing parameters to ensure better bonding between the two materials. These findings highlight the importance of carefully controlling the printing process to achieve optimal microstructure morphology and material adhesion results.

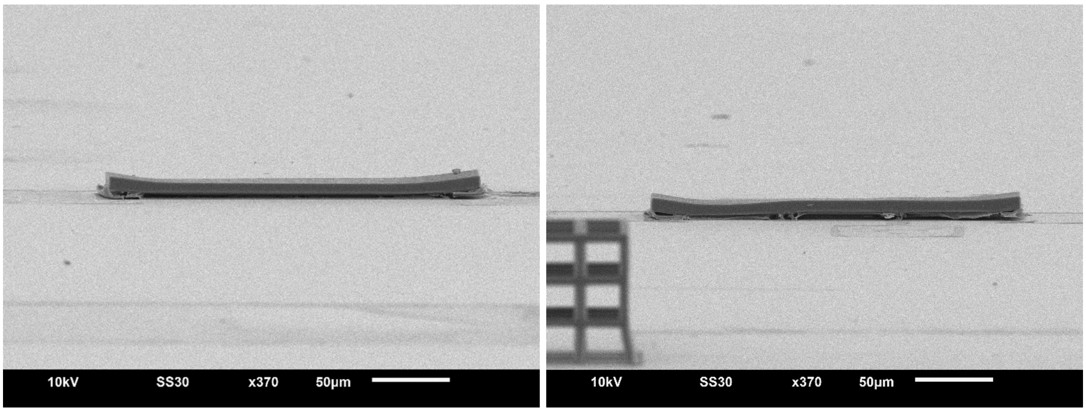

(a) **(b)** e

Figure 5.27: SEM image of 5% doped microstructure on gold pads, (a) 2-point probe, (b) 4-point probe

Upon closer examination of Figure 5.28, it becomes evident that the gold pads might have undergone erosion during oxidative polymerisation, resulting in a porous texture. Additionally, the base and main layers display observable discrepancies due to differing shrinkage levels during development. This visual distinction between the base and main layers becomes apparent due to varying levels of shrinkage during the development process of the layer printed on silicon. Next, the mechanical properties of the printed structures are characterised.

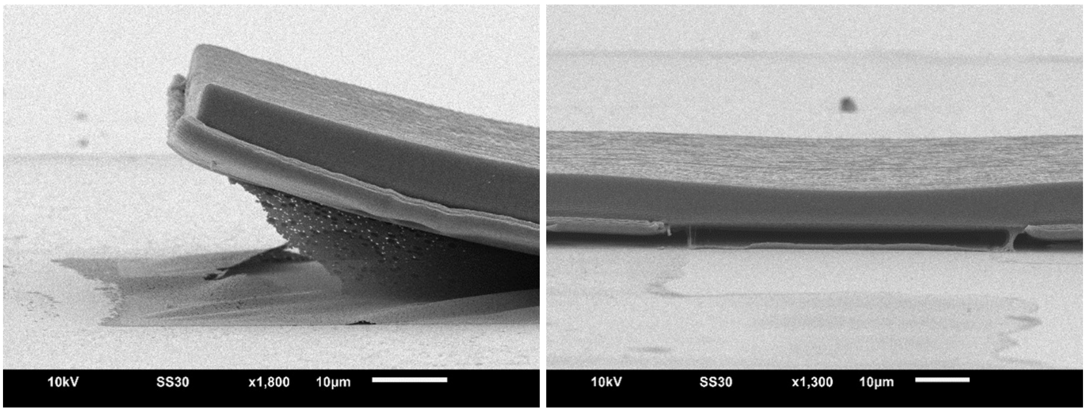

(a) **(b)**

Figure 5.28: Higher magnification SEM image of 5% doped microstructure on gold pads, (a) 2-point probe, (b) 4-point probe

5.2. Mechanical Characterization

The mechanical characterisation involves a set of pedestal samples with dimensions of 30x30x30 μm^3. Accurate analysis requires considering the dimensions after both printing and chemical polymerisation. Young's modulus (E) is calculated using the formula E = KL/A, where K represents the stiffness derived from the force-distance graph using the Femtotools data analysis toolkit. In this equation, L denotes the height of the pedestal, and A corresponds to the cross-sectional area.

During the compression test, precautions are taken. A safety margin of 5 μm is maintained, ensuring the compression does not exceed 4 μm. Moreover, an upper limit of 90 mN is set within the program to prevent excessive loading. The test is executed with a compression speed of 0.25 $\mu m/s$ and 25 $\mu m/s^2$ acceleration. This method allows for a comprehensive evaluation of the mechanical properties of the pedestal samples.

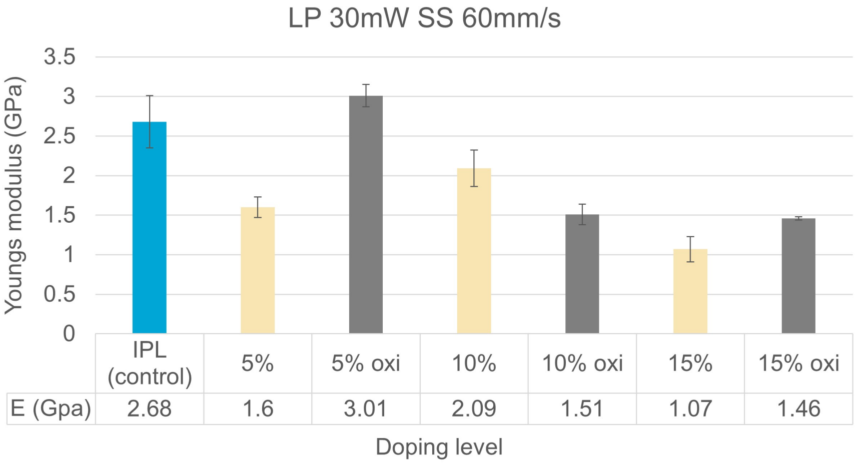

Figure 5.29: Young's Modulus at 30 mW and 60 mm/s laser dosage

The results obtained from the compression tests on various samples provide valuable insights. As the doping level of the materials increases, there is a noticeable decrease in Young's modulus. This trend is particularly evident in the doped structures. Interestingly, applying oxidative polymerisation leads to an increase in modulus in these doped structures.

For structures printed using a 25x objective, Young's modulus of IP-L (control) is measured at 2.68 GPa under the printing conditions of 30mW laser power and 60 mm/s scan speed. This value significantly drops to 1.07 GPa for structures doped with 15% EDOT. Remarkably, after the chemical polymerisation process, the modulus of the 15% EDOT doped structures rises to 1.46 GPa. The most noteworthy changes are observed in the 5% doped structures, where Young's modulus escalates from 1.59 GPa to 3.01 GPa following chemical polymerisation. These findings suggest that doping and the chemical polymerisation process substantially impact the structures' mechanical properties. Here, an anomaly occurs with 10% EDOT prints. Young's modulus drops after oxidative polymerisation. The exact reason for this is unknown, but this might be due to the composite nature of IP-L and PEDOT. The Young's Modulus of PEDOT films is 2.6 ± 1.4 GPa [80].

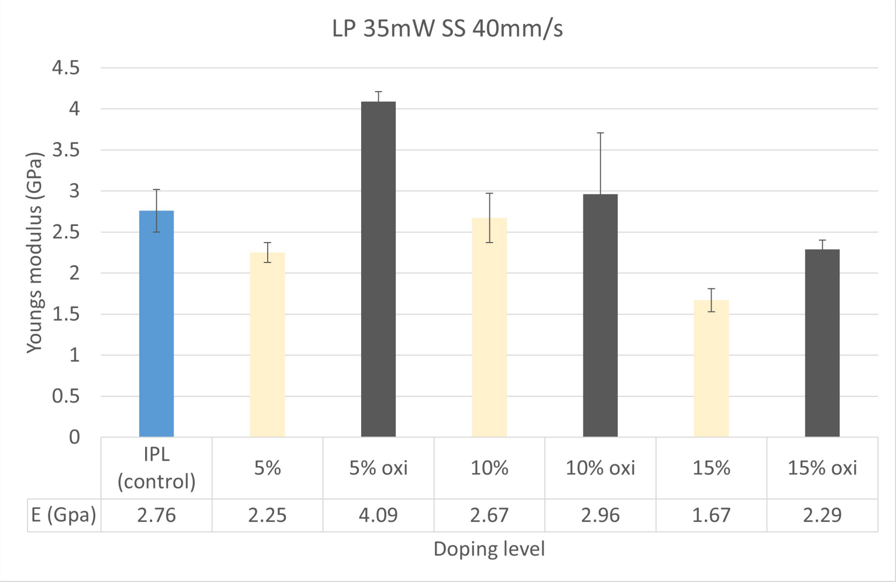

Figure 5.30: Young's Modulus at 35 mW and 40 mm/s laser dosage

Since for 15% doped resin, it was observed that 35 mW and 40 mm/s printing dose gives better print quality comparatively, the mechanical compression test is also performed on this dosage for all the doping levels. The trend of decreasing Young's modulus with higher doping levels remains consistent with these parameters. The structures' overall stiffness increases with higher laser dosages, as highlighted in Figure 5.30. This finding emphasizes the complex relationship between material composition and printing process parameters in determining the mechanical properties of microstructures. The anomaly in this laser exposure occurs at 5% EDOT. Here Young's modulus of 5% EDOT is lower than that of 10% EDOT. It might be possible that this behaviour is caused due to different extents of polymerisation at other laser exposures. With the fabrication process's optimisation and mechanical characterisation completion, the focus shifts to a critical aspect of the material—its electrical conductivity.

5.3. Electrical characterisation

During this phase of the study, the focus lies on characterizing the electrical conductivity of the printed microstructures, offering significant insights into their performance. An exhaustive protocol is initially developed through an iterative process, which delves into various factors. These factors include the effect of laser exposure, the effects of solvent treatment, the implications of hatch direction, the effects of UV exposure, and the effects of phosphate buffer solution on the electrical conductivity of large 2D 2PP printed microstructures. Ultimately, the electrical conductivity of structures printed directly onto the gold pads is also measured, providing a comprehensive assessment of the material's conductive properties. This study step forms a crucial bridge between fabrication and application, contributing to a deeper understanding of the material's functional attributes.

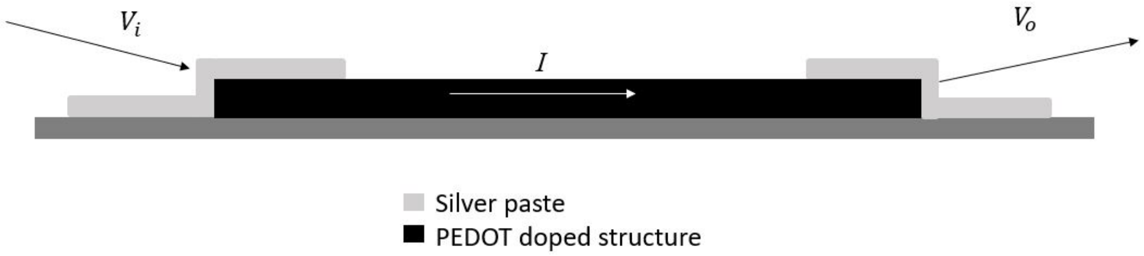

Figure 5.31: Illustration of current flow for 2-point IV sweep with silver paste

Silver paste is applied to the structure's ends to establish a reliable connection between the probe and the 2PP printed material. This application ensures that the current flows through the outer surface of the 2PP printed structure when utilizing the silver paste. For analytical calculations, it is considered that the current distribution remains uniform across the cross-section, as depicted in Figure 5.31. The designated thickness remains consistent at 15 µm throughout the prints. The dimensions of the areas not covered by the silver paste are meticulously measured using a microscope as shown in Figure 5.32. The centre part of the two-point probe structure is 600x100x15 μm^3, and the ends are 600x200x15 μm^3. In the four-point microstructure, the horizontal segments are 600 μm, and the vertical protrusions are 400 μm.

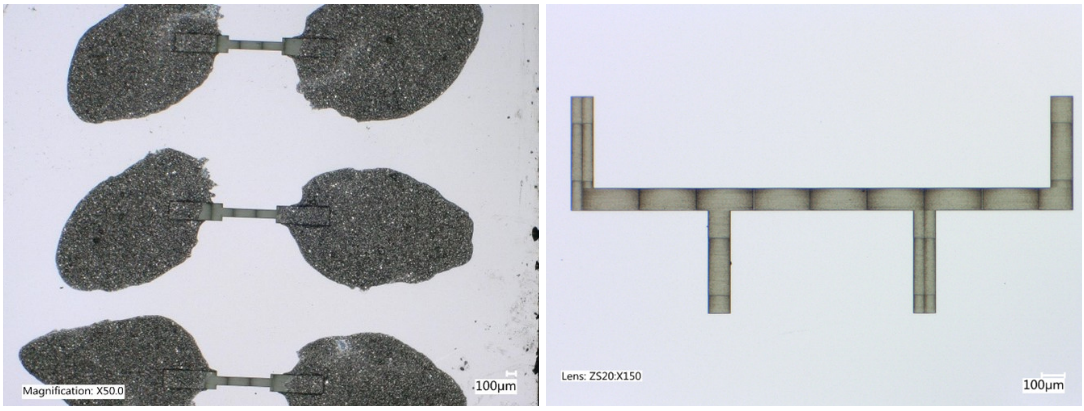

(a) (b)

Figure 5.32: 2D microstructures used for IV sweeps, (a) Structure for 2-point IV sweep with silver paste, (b) Structure for 4-point IV sweep

An interesting phenomenon is apparent in the obtained IV sweep plots from the 2-point measurements, as depicted in Figure 5.33a. This behaviour exhibits hysteresis and a memory effect. A reference to the existing literature on the electrical properties of PEDOT:PSS films provides valuable insights. These films show a switchable diode phenomenon and a reduction state that becomes active upon applying high voltage. For further context, Figure 5.33b illustrates the IV sweep under both vacuum and atmospheric conditions, as documented in sources such as [81] and [82]. These findings emphasize the complex and intriguing nature of the electrical characteristics displayed by PEDOT:PSS films.

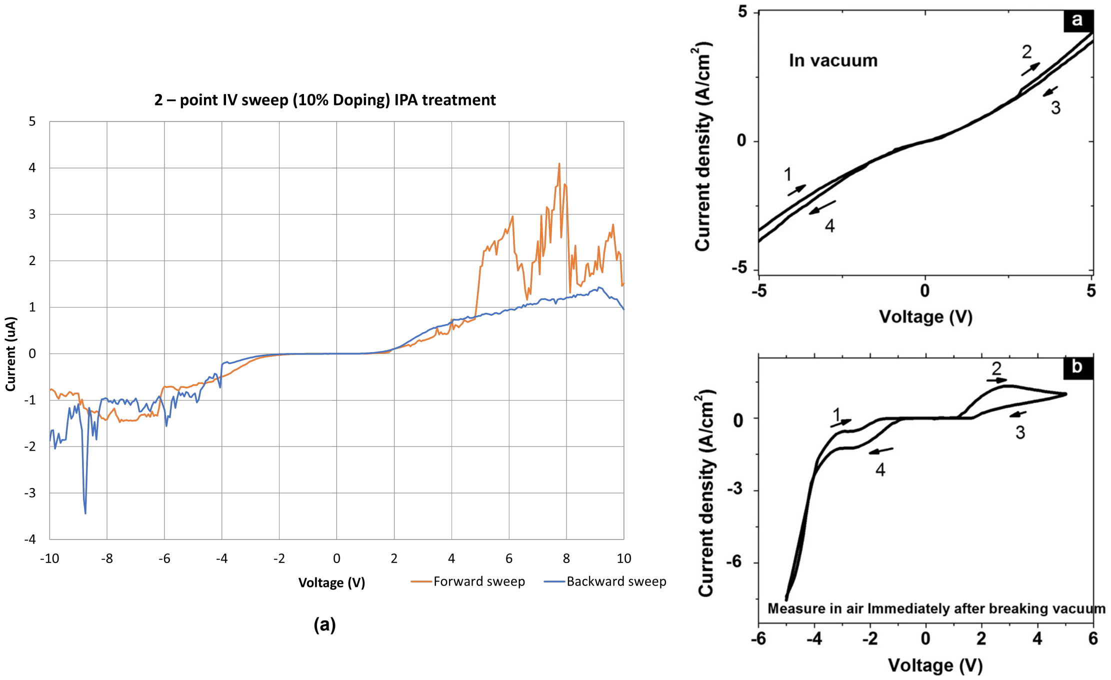

(a) (b)

Figure 5.33: Electrical behaviour of PEDOT, (a) IV sweep of oxidative polymerised 10% EDOT 5mm line on Silicon substrate, and (b) IV sweep of PEDOT:PSS thin film[81]

5.3.1. Effect of laser dose on conductivity

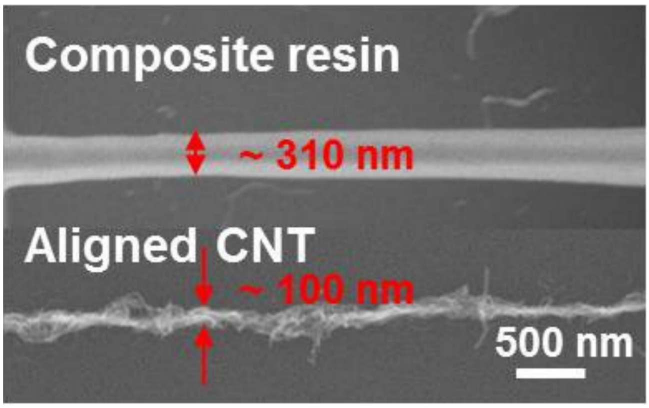

Figure 5.34: SEM micrographs of an MCNT straight wire before/after thermal annealing[83]

While 2PP printing with carbon nanocomposites infused resin, as highlighted in [83], a prevalent observation in the literature suggests that a significant portion of the particles align themselves along the printing lines, as illustrated in Figure 5.34.

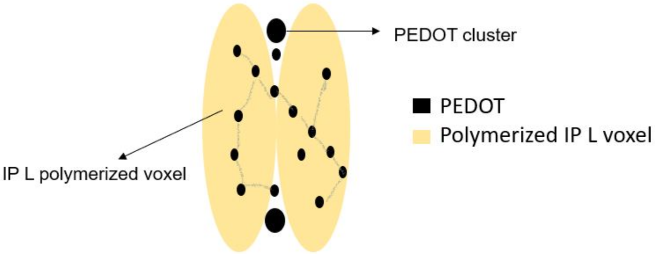

Figure 5.35: PEDOT cluster distribution in IPL voxel

Drawing from this observation, it might be possible that EDOT molecules could exhibit a similar alignment pattern along the hatch lines and within any possible voids or deformations arising between these lines during the fabrication process. Such alignment tendencies might give rise to PEDOT clusters in those locations, as depicted in Figure 5.35. This proposed mechanism could explain how distinctive conductivity patterns emerge in printed microstructures.

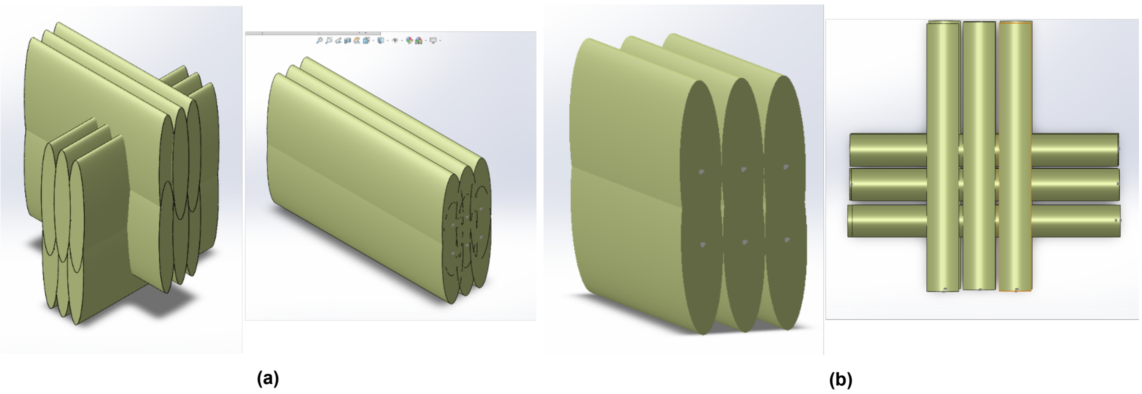

Figure 5.36: Illustration of voxel matrix for 25x objective printed in IP-L, (a) Ideal matrix, (b) Matrix with increased hatching and slicing

Hence, manipulating the gaps within the IP L matrix could influence the resulting conductivity of the structure. The configuration shown in Figure 5.36 illustrates the ideal polymerised resin matrix without gaps and a matrix with deliberate gaps introduced into it. The voxel dimensions in IP-L for the 25x objective are 2.5 μm in height and 0.6 μm in width [11]. This illustration is designed based on this information and the specified hatching distance of 0.4 μm and slicing distance of 0.7 $\mu m.$ To test this hypothesis, two distinct approaches are pursued. First, altering the printing dose to modulate the degree of polymerization within the voxel, and second, modifying the printing direction.

Table 5.2: Effect of laser dosage on conductivity

Scan speed (mm/s)	Conductivity (S/m)
80	2.055 ± 0.98
60	0.34 ± 0.11
40	0.55 ± 0.11

The results of these experiments unveil intriguing trends. Reducing the printing dose by increasing the laser's scanning speed leads to a noteworthy enhancement in conductivity (as documented in table 5.2). It is to be noted that the voxel size remains the same for the same laser power, but the extent of polymerisation within that voxel changes with a change in scan speed. This creates non-uniform print lines. Furthermore, adjusting the hatch offset, the orientation of print lines concerning the previous slice, from 90° to 0°, also exerts a discernible impact on the conductivity (as detailed in table 5.3). It is also observed that diminishing the printing dose amplifies the deformations within the structure post-chemical oxidation.

5.3.2. Effect of solvent treatment on conductivity

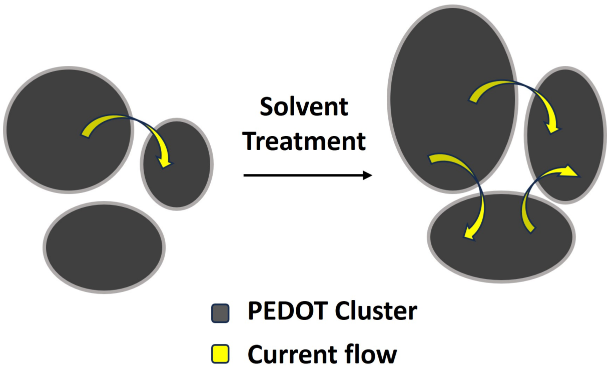

Figure 5.37: Effect of solvent treatment on PEDOT cluster

According to the existing literature, it is evident that the treatment of solvents has a significant influence on the conductivity of thin films that comprise PEDOT PSS clusters [84] [85]. The conducted studies have indicated that exposure to solvents subsequently triggers the extension of these clusters within the doped microstructures. Such a phenomenon could have a crucial impact on shaping the overall electrical properties of the microstructures, as visually depicted in Figure 5.37.

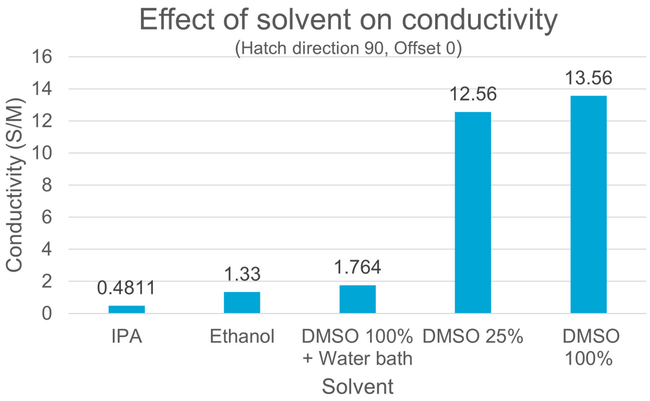

Figure 5.38: Effect of solvent treatment on electrical conductivity

The choice of solvents is a careful process, considering their interactions with the material. This choice is pivotal for ensuring the accuracy of conductivity assessments and attaining dependable and scientifically meaningful outcomes, as illustrated in Figure 5.38. Observations distinctly reveal a noteworthy upsurge in conductivity, approximately 32 times higher, when employing DMSO in contrast to IPA treatment, as highlighted in table 5.3. This observation points toward the substantial influence of DMSO on the material's conductivity. DMSO, an extensively employed organic solvent, has a high dielectric constant, which might facilitate heightened mobility of charged particles within the material, thereby contributing to increased conductivity. Conversely, IPA's lower polarity and dielectric constant could potentially impede ion mobility, thus yielding comparatively lower conductivity values. Besides pure IPA and DMSO, Ethanol and diluted DMSO + demi water are also used in this solvent study. Here, there is an increase in conductivity by 2.7 and 3.7 times, respectively.

5.3.3. Effect of UV exposure on conductivity

UV light sterilization of microstructures is done before cell culture in some instances. The study investigated the relationship between the conductivity of 2PP printed structures and UV treatment and laser dosage variables. The PEDOT clusters are embedded within a polymerized IP-L matrix. Extended UV exposure can affect the electrical conductivity of the structures by changing the PEDOT-IP-L matrix. There are two ways to study this phenomenon: (i) exposing the structures to UV light after oxidative polymerization and (ii) exposure to UV light before the oxidative polymerization process. The investigations provide a deeper understanding of how UV treatment affects electrical conductivity based on structural and material properties.

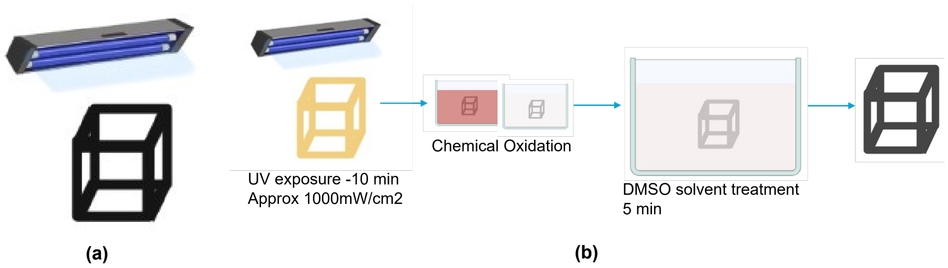

Figure 5.39: Illustration of the UV treatment procedure, (a) After oxidative polymerisation, (b) Before oxidative polymerisation

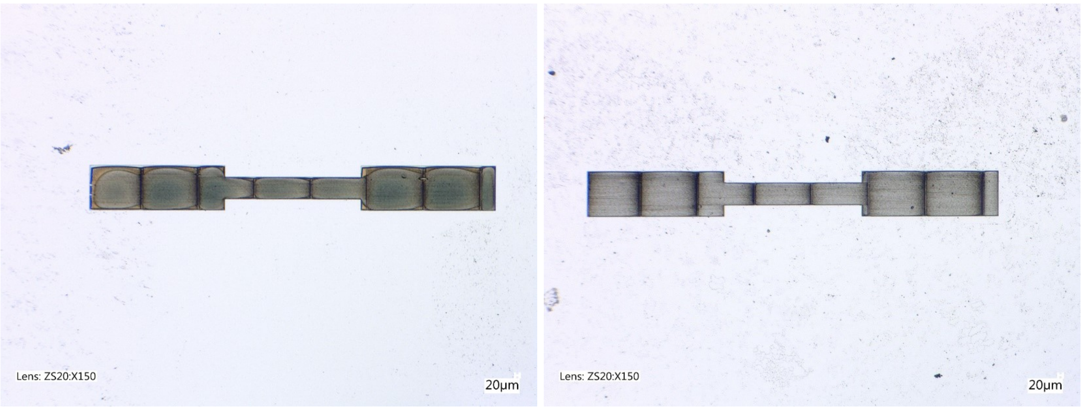

(a) (b)

Figure 5.40: Optical microscope images of a 2-point probe microstructure on which UV treatment is performed, (a) After oxidative polymerisation, (b) Before oxidative polymerisation

The effects of UV exposure are closely examined with specific parameters. A UV exposure of 1000 mW/cm² for 10 minutes is applied using the Honle UV spot source (bluepoint 4 ecocure). When just oxidative polymerised 10% EDOT print has conductivity 13.56 ± 2.68 S/m. However, with UV treatment after the oxidative polymerisation process, the conductivity experiences a decline to 10.78 ± 7.65 S/m. This reduction might be attributed to the polymerisation of residual photoinitiator around the PEDOT clusters, rendering the structure more rigid. Conversely, the PEDOT clusters have yet to form when applying UV polymerisation before chemical polymerisation. Consequently, the spaces that would accommodate these clusters might be reduced, a polymerisation in conductivity measurements showing a value of 7.22 ± 2.7 S/m – approximately half of that without any UV treatment. Notably, the microstructure treated with UV before oxidative polymerisation exhibits minimal deformation. This phenomenon is likely due to heightened rigidity from overexposure to UV light, as depicted in Figure 5.40.

The results of all the parameters mentioned above are summarised in the table 5.3, and all images of microstructures are in Appendix C.

Table 5.3: Effect of printing parameters and treatments on the electrical conductivity of PEDOT doped microstructures

Doping	Treatment	Hatch direction	Hatching Offset	2 Point (S/m)	4 Point (S/m)
10%	IPA 3min	90 90	0 90	0.4811 (Oil), 0.34 (DiLL) 17*10-6 (Oil)	-
10%	Ethanol 3 min	90	0	1.28 ± 0.09	-
10%	DMSO 5min + water 3min	90	0	1.764	-
5%	DMSO 25% 5 min	90 45	0 90	6.59 ± 2.44 6.13 ± 0.76	2.97 ± 2.28 9.12 ± 6.42
10%	DMSO 25% 5 min	90 45	0 90	15.28 ± 3.55 20.28 ± 2.11	6.14 ± 0.62 6.00 ± 3.95
15%	DMSO 25% 5 min	90 45	0 90	12.56 ± 1.07 4.67 ± 1.11	4.55 ± 2.19 4.33 ± 1.4
10%	DMSO 25% 5min UV post-treatment 10min	90 45	0 90	14.33 ± 7.03 26.29 ± 5.92	6.31 ± 2.03 10.82 ± 6.93
10%	DMSO 100%	90 45	0 90	13.56 ± 2.68 9.83 ± 4.58	-
10%	DMSO 100% 5min UV post-treatment 10min	90 45	0 90	10.78 ± 7.65 8.31 ± 1.24	-
10%	UV pre-treatment 10 min DMSO 100% 5min	90 45	0 90	7.22 ± 2.7 6.5 ± 2.74	-

In Figures 5.41, 5.42, 5.44, 5.43, the IV sweeps measurement are displayed for IP-L control and doped PEDOT dogbone structures treated with 100% DMSO, with bias voltages of 5V and 1V. Specifically, in the 5 V bias plots (a), the resistance within the 2-3 V range is approximated for the calculation of electrical conductivity. It is important to note that the behaviour of this plot is dynamic, leading to varying resistance values as a function of the applied voltage bias. The 1 V bias plot (b) shows the electrical response to low voltage. Much smoother curves are obtained at lower voltages, but the conductivity in this region is 270-1000 times lower compared to the 2-3 V region.

The microstructure under investigation comprises IP-L (an Acrylate-based resin) and PEDOT, a conductive polymer. Assumptions are made that the composition is nearly homogeneous. Thus, the final electrical properties are an amalgamation of both materials. The electrical characteristics of PEDOT exhibit a switchable diode phenomenon with a memory effect, while the electrical attributes of IP-L remain unknown. Electrical testing was also conducted on IP-L, as depicted in Figure 5.41 to provide context. A noticeable distinction is observed, where the current flow for IP-L at low voltages is in the pA range, in stark contrast to doped samples exhibiting a flow in the nA range.

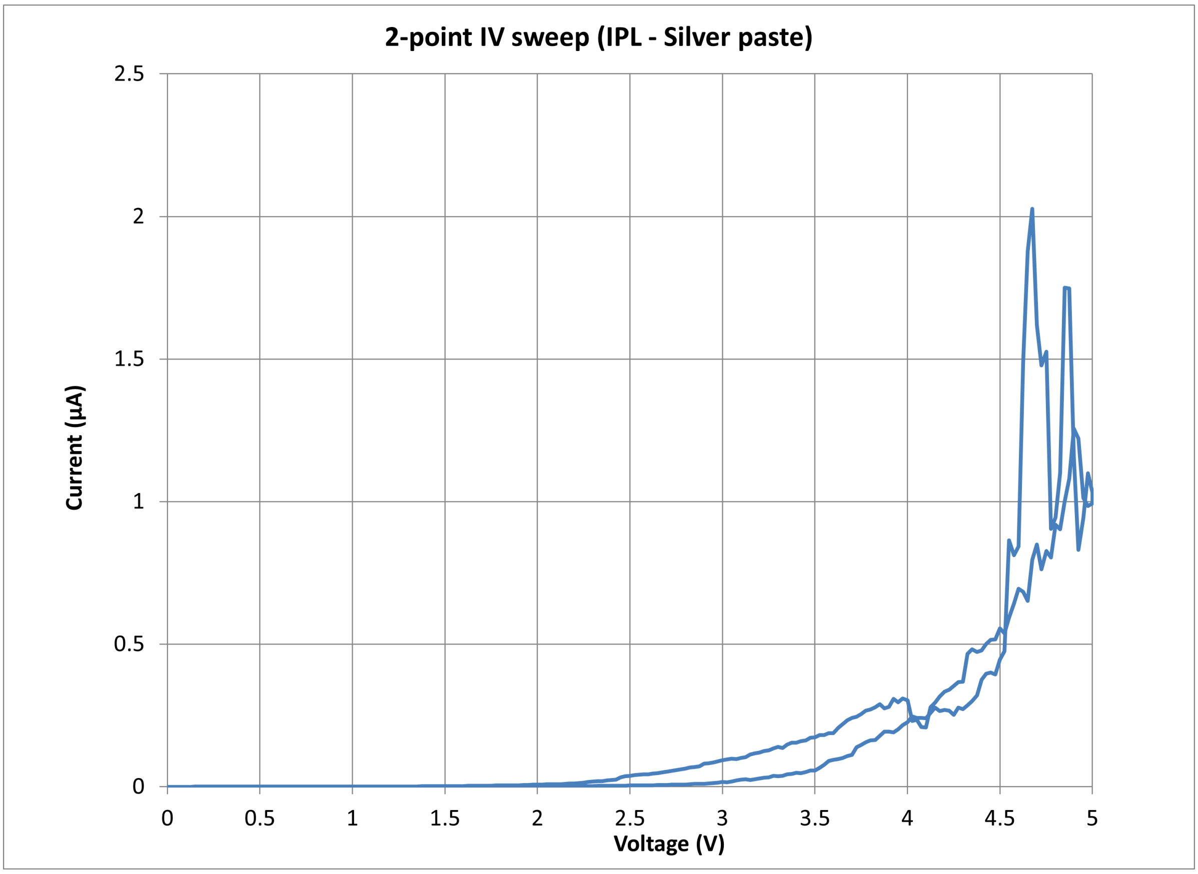

(a)

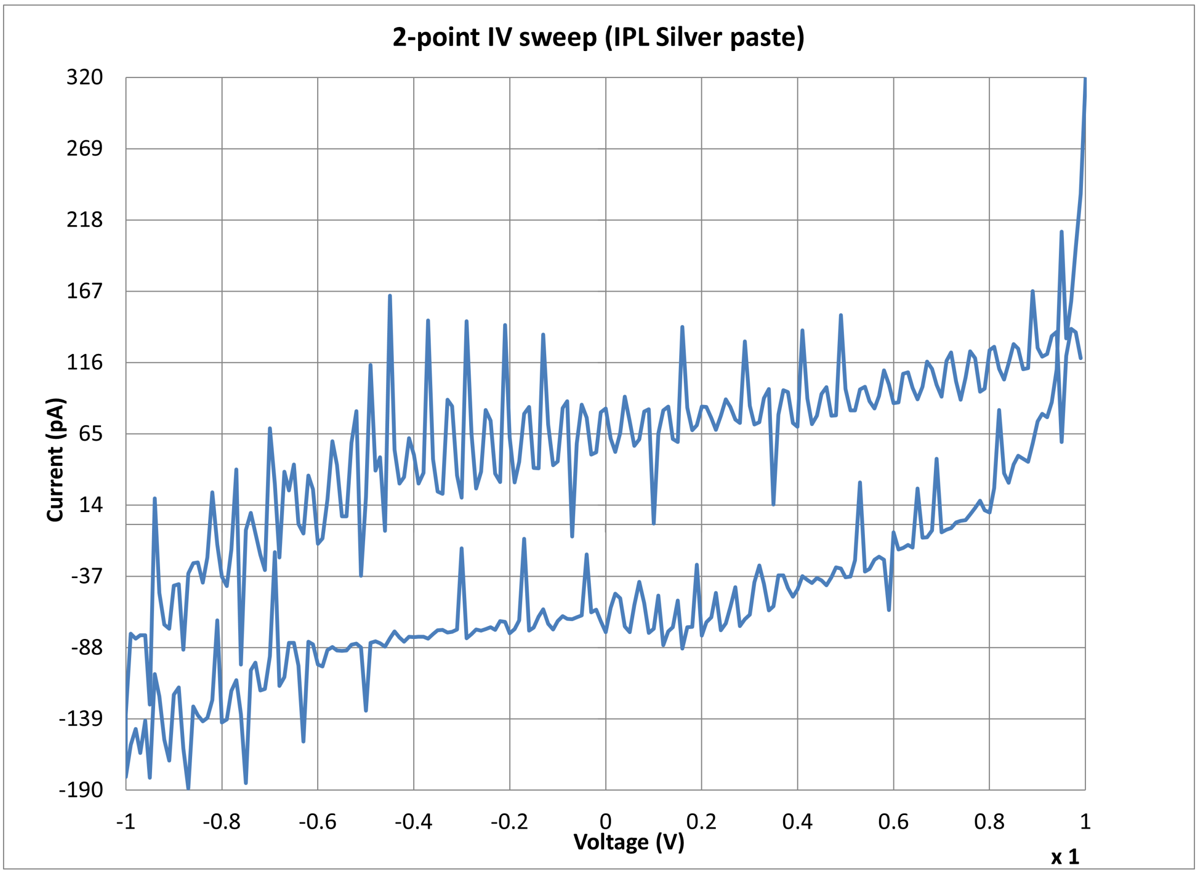

(b)

Figure 5.41: 2-point IV sweep of IP-L microstructure (control), (a) 5 V bias, (b) 1 V bias

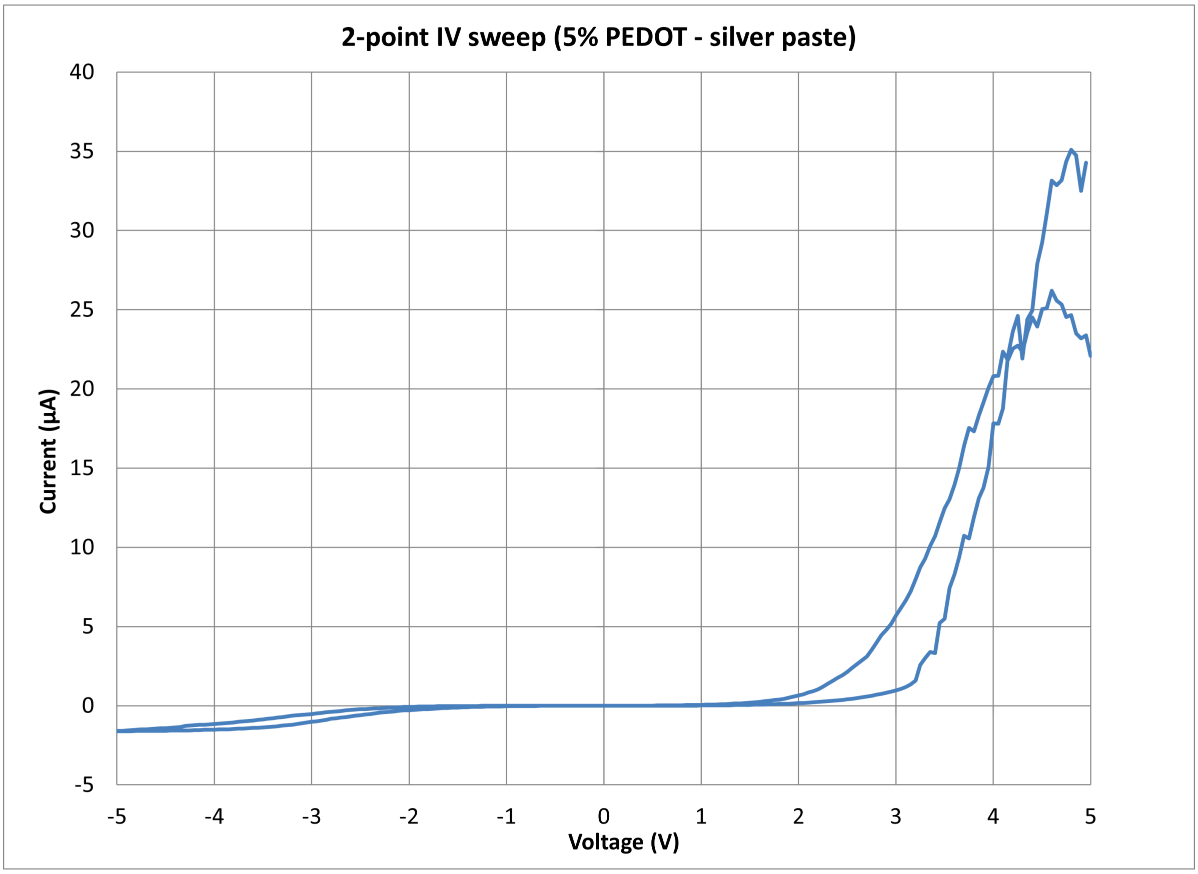

(a)

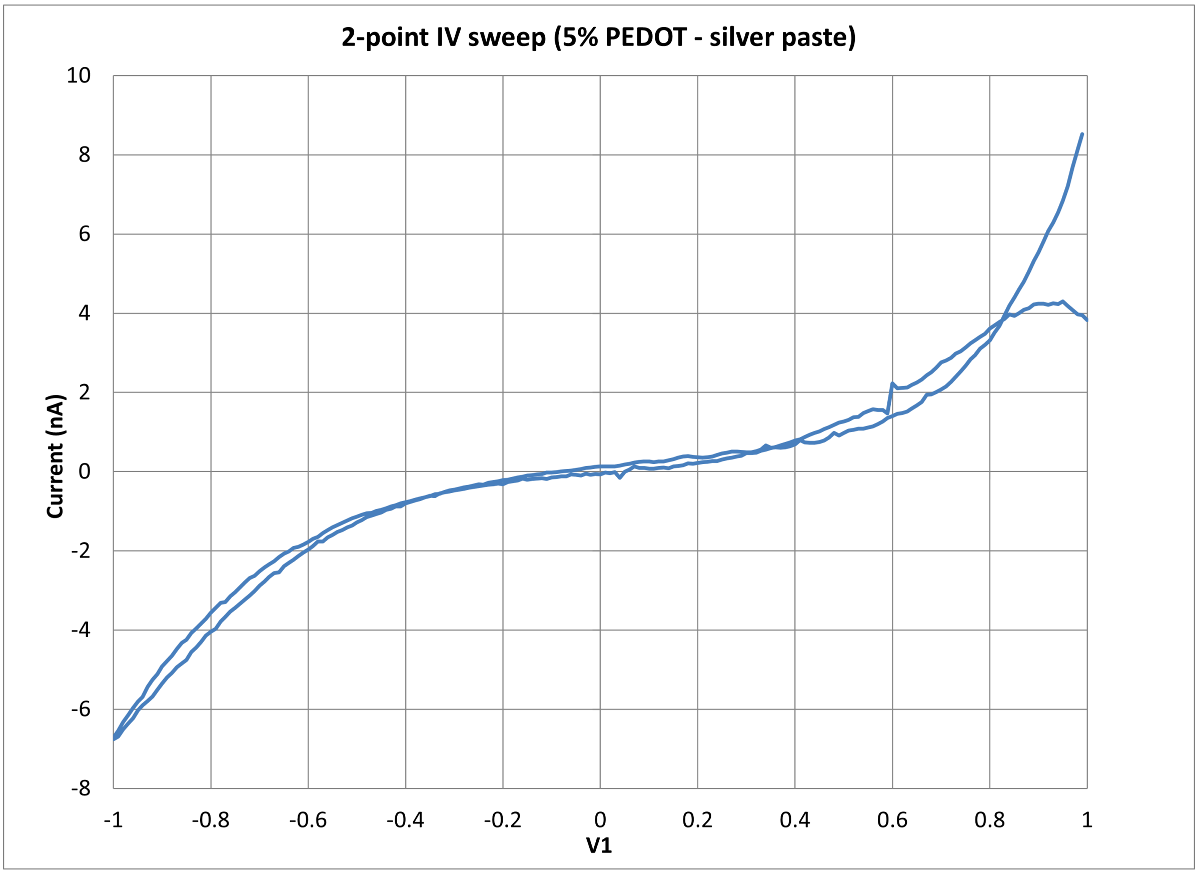

(b)

Figure 5.42: 2-point IV sweep of DMSO treated 5% doped microstructure (a) 5 V bias, (b) 1 V bias

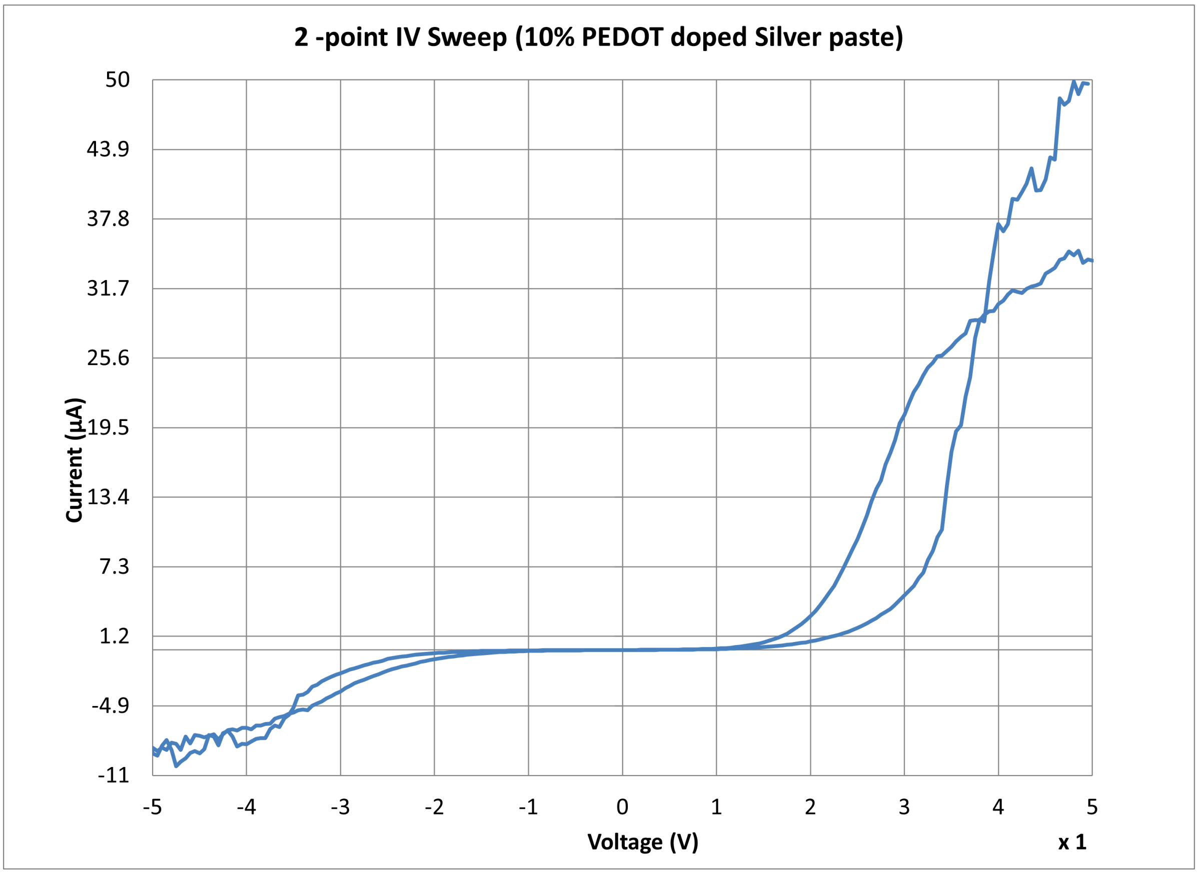

(a)

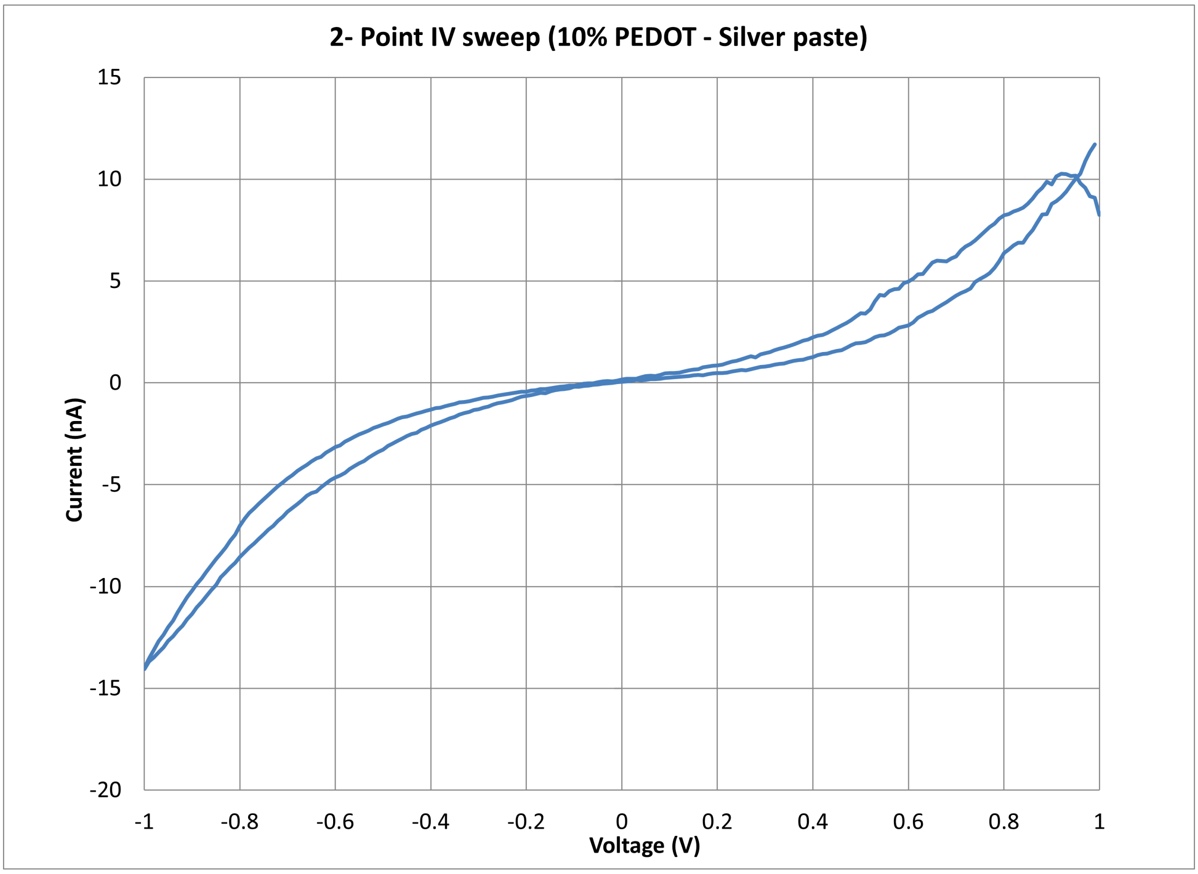

(b)

Figure 5.43: 2-point IV sweep of DMSO treated 10% doped microstructure, (a) 5 V bias, (b) 1 V bias

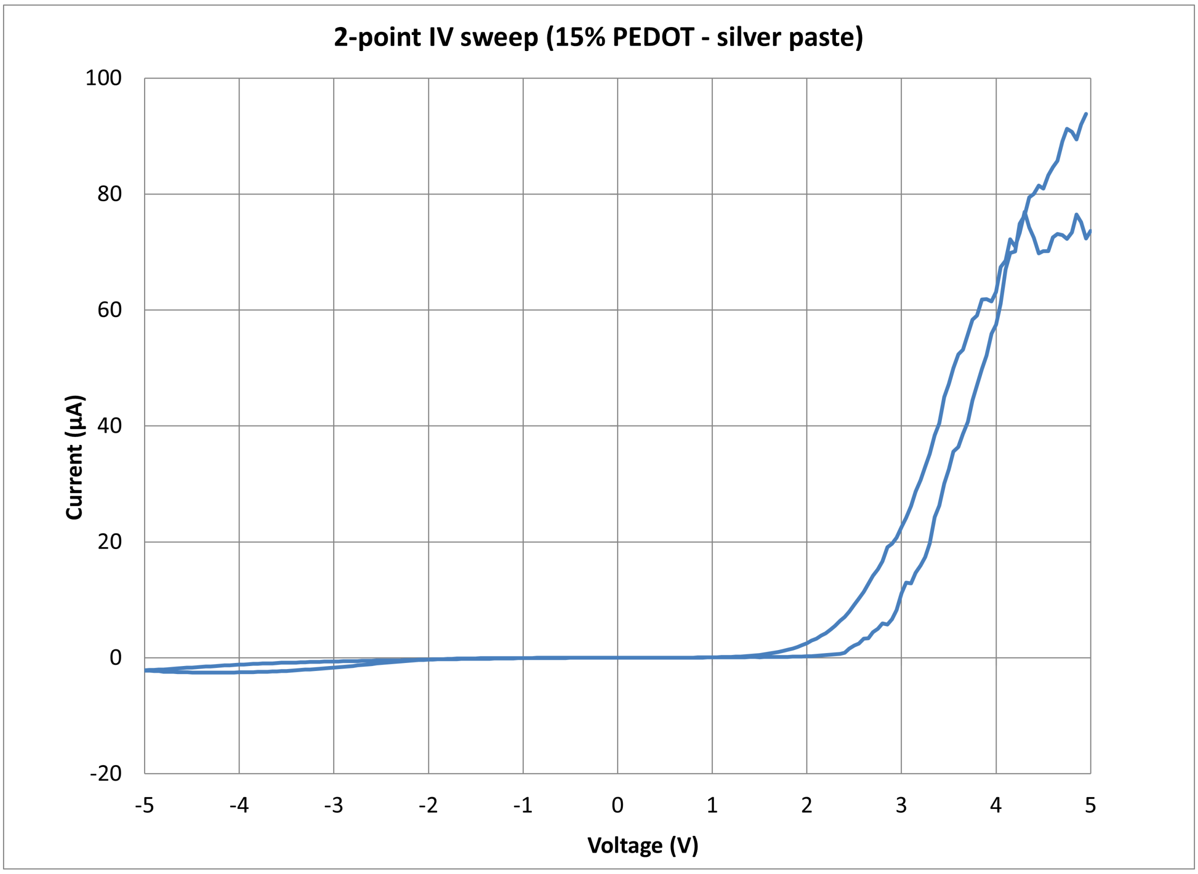

(a)

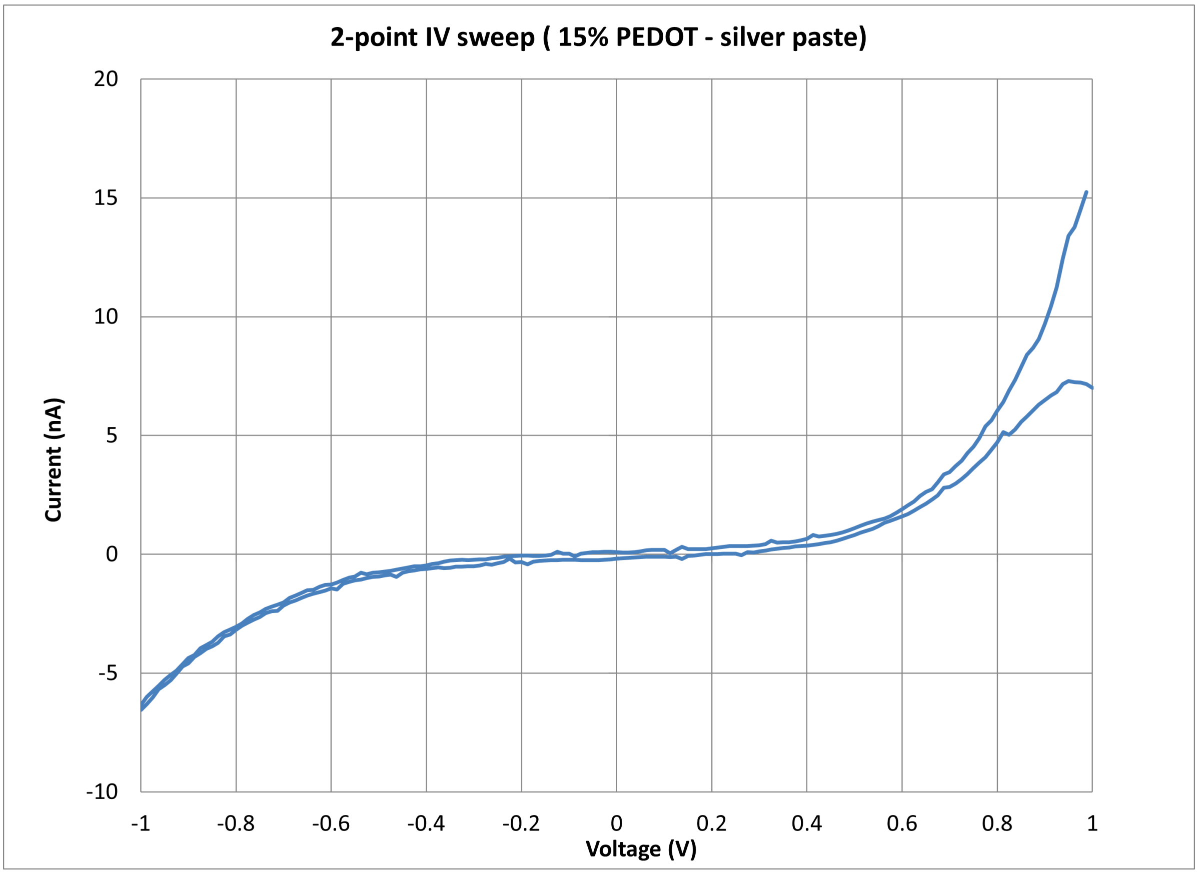

(b)

Figure 5.44: 2-point IV sweep of DMSO treated 15% doped microstructure (a) 5 V bias, (b) 1 V bias

Effect of Phosphate buffer solution on conductivity

Table 5.4: Electrical conductivity at controlled temperature and effect of PBS immersion for 3 days

Doping level	DMSO 100% (S/m)	PBS 3 days (S/m)	Change (%)
IP L (control) *	0.01745 ± 0.00785	-	-
5% EDOT	7.92 ± 2.13	7.82 ± 1.93	-0.5
10% EDOT	12.62 ± 3.54	10.36 ± 1.56	-17.91
15% EDOT	17.43 ± 4.78	8.46 ± 5.47	-51.46

* For IP L (control), the oxidative polymerization step is not performed.

The microstructures for cell cultures have been thoroughly prepared for their intended use. The two-point microstructures were submerged in a Phosphate-buffered saline (PBS) solution with a pH of 7.4 and kept at 37°C for three days to mimic conventional culture medium conditions. Notably, after this immersion period, a noticeable decrease in conductivity is observed as the level of doping increases, as outlined in Table 5.4. This phenomenon might be attributed to the hypothesis that solvents lead to the enlargement of PEDOT clusters. Given this hypothesis, higher doping levels are anticipated to result in more substantial cluster formations, consequently leading to a more pronounced effect of the solvent. Moreover, prolonged exposure to the aqueous-based solution might result in the loss of solvent from highly doped structures into the solution, thereby significantly diminishing the available conduction pathways. IV sweep plots for doping levels and PBS treatments are shown in Figure C.12, Figure C.13 and Figure C.14.

Table 5.5: Electrical conductivity (in the region -1 to 1V) at controlled temperature and effect of PBS immersion for three days

Doping level	DMSO 100% (S/m)	PBS 3 days (S/m)	Change (%)
IP L (control) *	0.0002 ± 0.0001	-	-
5% EDOT	0.0292 ± 0.0222	0.0185 ± 0.0101	-36.66
10% EDOT	0.0113 ± 0.0035	0.0098 ± 0.0079	-13.27
15% EDOT	0.0591 ± 0.0135	0.2150 ± 0.2780	+263.79

5.3.4. Conductivity of microstructures printed on Gold Electrodes

Regarding the printing process, there are notable distinctions between printing on gold and silicon substrates. Gold pad prints incorporate base layers, contributing to observed differences in their behaviour. Microexplosions in microstructure during printing and deformations in gold pads occur after the chemical oxidation process. It is worth noting that the current flow encounters specific disparities, mainly through the bottom layers and layers closer to the gold pads.

A lower laser dosage is utilized for these layers to avert the occurrence of microexplosions. These microexplosions stem from laser reflection on the gold surface and residual AZ adhered to the print walls. In gold pad prints, placing needle probes is a crucial consideration. Figure 5.46 offers insight into the precise arrangement of these needle probes on the gold pads, emphasizing their strategic positioning for accurate measurement and analysis.

Figure 5.45: Electrical conductivity of microstructures printed on gold pads

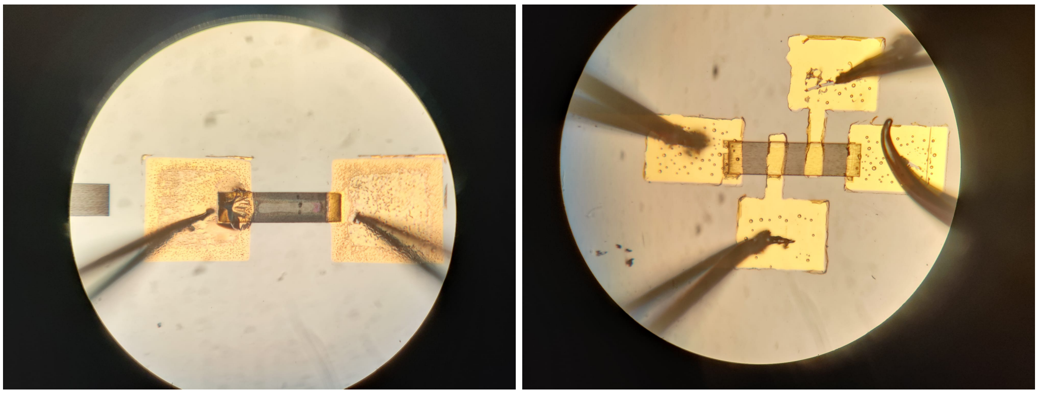

(a) (b)

Figure 5.46: Probe placement for (a)2-point, (b) 4-point measurements on gold electrodes

Table 5.6: Electrical conductivity of microstructures printed on Gold Electrodes

Method	IP L (control) S/m	5% EDOT (S/m)	10%EDOT (S/m)	15% EDOT (S/m)
2 point	0.47 ± 0.08	-	1.51 ± 0.37	1.29 ± 0.76
4 point	0.36 ± 0.02	-	0.20 ± 0.03	0.13 ± 0.74

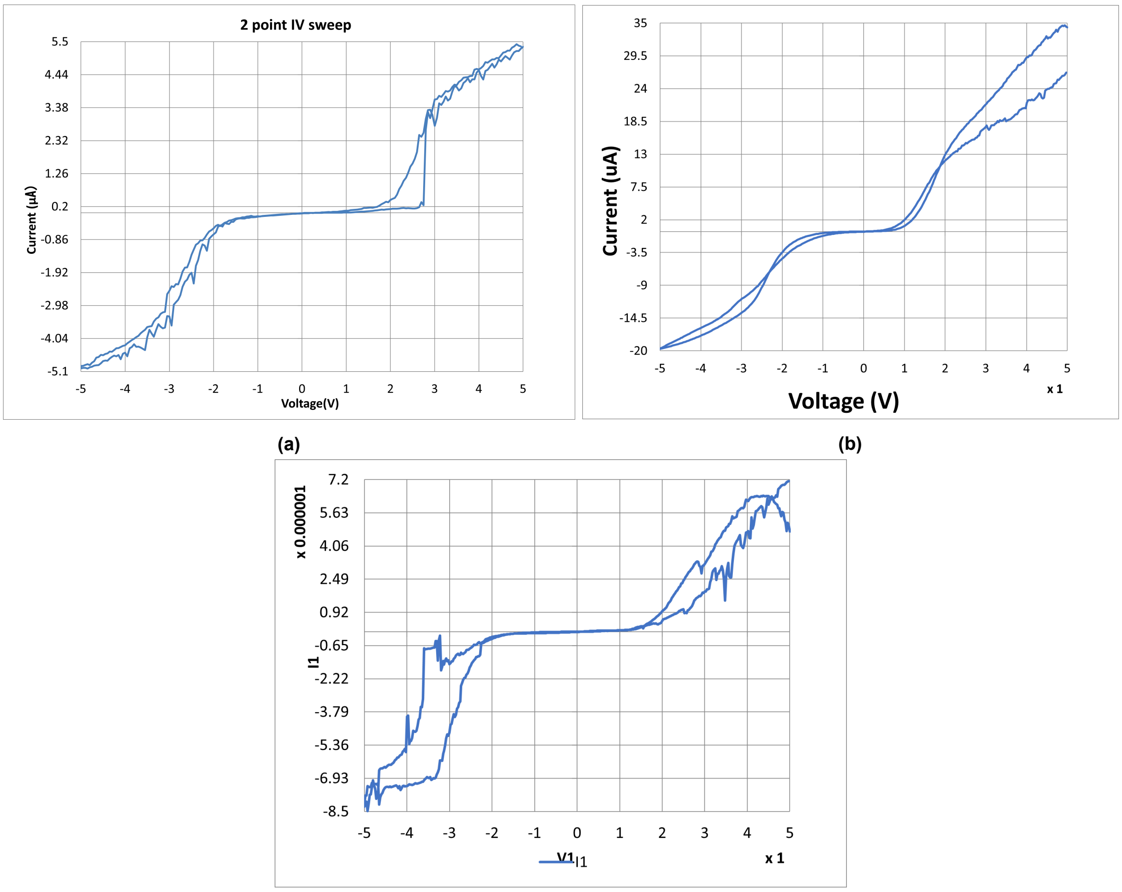

(a) (b)

(c)

Figure 5.47: 2-point IV sweep of microstructures printed on gold pads, (a) IP L (control), (b) 10% PEDOT, (c) 15% PEDOT

These changes in printing parameters and complications lead to non-comparable results in conductivity measured from gold pads and silver paste. It is also observed that there is no apparent variation between 10 and 15% doping of PEDOT, whereas there is a jump in conductivity compared to IP-L(control), Table5.6. The IV sweeps of these are depicted in the Figure.5.47. It is also observed that there is an inconsistency in the gold pad delamination during the chemical oxidation stage, which leads to no measurable samples for 5% doping as there were six consecutive failures. This might be due to the adhesion between Silicon and sputtered gold, this gold layer not homogeneous, and erosion of gold in the acidic medium (chemical bath for PEDOT polymerization); it also might be the MAPTMS layer on the Silicon. The exact cause for this failure is inclusive. The IV sweep plots for four-point measurement are shown in Figures C.15, C.16, C.17, they show a more symmetric behaviour as the current is forced through the material.

6

Conclusion

This thesis aimed to develop 3D electrically conductive scaffolds by two-photon polymerisation (2PP), a 3D printing technology with sub-micrometre resolution.

The fabrication of electrically conductive microstructures was successfully achieved through the utilization of 2PP technology and the incorporation of PEDOT doping, coupled with the utilization of IP-L, a commercial photoresin. A beam array was utilized to determine the printing limitations of the process, and the smallest feature size measured 1.455 x 1 μm^2. Intricate 3D cage-like matrices were also synthesized, characterized by a pore size of 22 μm, 5.8 μm beam thickness, and a structural porosity of 40.69%. A protocol to fabricate 2D gold structure with micrometric is also developed by combining 2PP for maskless lithography and industry-standard lift-off process.

The process of fabricating free-standing electrically conductive scaffolds is successfully developed and characterised. In the results reported in this thesis, the maximum recorded was 26.29 ± 5.92 S/m. This value was achieved using 10% doped EDOT resin, printed with a 45° hatch offset and treated with UV after oxidative polymerisation on a DMSO-treated sample. This value was compared to a similar PEDOT doping approach within a custom resin (Kurselis et al.) reported a value of 4 S/m. Moreover, the study also evaluated the effect of solvents on PEDOT grains. It has been shown that solvent treatment, typically used in the development of pristine PEDOT: PSS films, can also significantly increase the conductivity of PEDOT-doped microstructures. For 10% EDOT printed microstructures the conductivity increased from 0.48 S/m (using IPA) to 12.62 ± 3.54 S/m (using DMSO). In contrast, the conductivity of the brain ECM is 0.17 - 0.27 S/m.

The reported results pave the way to investigate further the effect of 3D electrically conductive PEDOT-doped microstructures on neuronal cell growth and development. The structures fabricated through this method could impact the differentiation and development of neurons.

7

Future Recommendations

The next step involves integrating this approach into a neuronal cell culture study. The focus is observing morphological changes in neuron growth, specifically dendrite quantity and elongation.

When it comes to improving printing resolution and achieving greater accuracy in printing fine details, choosing a higher numerical aperture (NA) objective can make all the difference. Specifically, selecting the 63x variation can significantly enhance the overall quality and precision of the printed output.

It would be worthwhile to explore the effects of a diluted oxidising agent on the reaction rate. This avenue of investigation holds promise for enhancing the connectivity of PEDOT chains and, as a result, improving the quality of printed microstructures. By delving into the existing literature, you may discover that slower reactions can facilitate the formation of smoother chains, providing valuable insights into the underlying chemical processes.

Adding PSS could enhance both the chain connectivity and electrical conductivity of microstructures. However, carefully optimising PSS's concentration and mixing methodology is of utmost importance to achieve the desired results. This will ensure that the microstructures function optimally and meet the intended objectives.

Expanding the proven EDOT doping methodology to more pliable resins like IP-PDMS presents an opportunity to create microstructures that mimic the human brain's extracellular matrix (ECM) characteristics. This could lead to advancements in neural and tissue engineering, as the ECM plays a critical role in cell behaviour and tissue development. We can better understand and replicate the brain's complex structure and functions by emulating its properties. The proposed approaches envision a multi-pronged effort to augment the resolution and quality of printed microstructures. This entails adopting a higher NA objective, managing reaction rates through diluted oxidising agents and enhancing chain connectivity and conductivity via PSS. The exploration of this approach's applicability to softer resins holds the potential to yield microstructures that closely mimic the characteristics of brain ECM, furthering the potential applications of this innovative technique.

8

Self-reflection

I was excited to begin a year-long journey of exploration and learning in a multidisciplinary field, combining micro-fabrication, chemistry, electrical experiments, and their application in tissue engineering.

While at PME, I gained exposure to microfabrication and worked with cutting-edge technologies like the 2PP fabrication system. Additionally, I learned about SEM characterization for imaging purposes. Despite my mechanical engineering background and limited knowledge in cell biology, chemical experimentation, and electrical setups, my thesis work helped me understand these domains better. I found the process of exploring chemical reactions and observing their visual transformations to be immensely enjoyable.

Although I am disappointed about not being able to conduct a neuronal cell culture study, it is heartening to know that my work will continue under the guidance of my supervisor. When I began my thesis, I was nervous about working with advanced equipment and potentially dangerous chemicals. However, I quickly gained confidence by following safety protocols and seeking expert advice when needed. As a result, I became comfortable and proactive in this specialized academic environment.

However, I faced a challenging phase where I felt stuck in a repetitive cycle for several months. Using the scientific principle of elimination and breaking tasks into smaller steps, I overcame this obstacle and achieved my goal, although it took some time.

During my research journey, I experienced emotional highs and lows. Although I enjoyed managing the experimental aspects, I needed help with the literature review and documentation. Acknowledging my areas of weakness, I worked hard to address them. The writing process was reflective and challenging, but it helped me grow as a person. However, I must improve my interpersonal skills to foster better communication and connections with colleagues.

Throughout my thesis, I gained significant insight into the importance of effective time management and setting realistic, achievable goals. I tend to fixate on a particular aspect or area of focus while disregarding other vital components, which can lead to disharmony and disarray. However, I have become increasingly skilled at recognizing this behaviour and identifying when to let go and redirect my attention towards other critical areas. I have also learned to use several tools and how to use them best to my advantage.

I am grateful to my supervisors for allowing me to explore my ideas. Through my practical thesis, I have gained vast knowledge and skills, thanks to their unwavering support and guidance.

References

[1] Alex Burnstine-Townley, Yoni Eshel, and Nadav Amdursky. “Conductive scaffolds for cardiac and neuronal tissue engineering: governing factors and mechanisms”. In: *Advanced Functional Materials* 30.18 (2020), p. 1901369.

[2] Richard Balint, Nigel J Cassidy, and Sarah H Cartmell. “Conductive polymers: Towards a smart biomaterial for tissue engineering”. In: *Acta biomaterialia* 10.6 (2014), pp. 2341–2353.

[3] Fa-Ming Chen and Xiaohua Liu. “Advancing biomaterials of human origin for tissue engineering”. In: *Progress in polymer science* 53 (2016), pp. 86–168.

[4] Filipa Pires et al. “Neural stem cell differentiation by electrical stimulation using a cross-linked PEDOT substrate: Expanding the use of biocompatible conjugated conductive polymers for neural tissue engineering”. In: *Biochimica et Biophysica Acta (BBA)-General Subjects* 1850.6 (2015), pp. 1158–1168.

[5] Andrew S Rowlands and Justin J Cooper-White. “Directing phenotype of vascular smooth muscle cells using electrically stimulated conducting polymer”. In: *Biomaterials* 29.34 (2008), pp. 4510–4520.

[6] Laleh Ghasemi-Mobarakeh et al. “Electrical stimulation of nerve cells using conductive nanofibrous scaffolds for nerve tissue engineering”. In: *Tissue Engineering Part A* 15.11 (2009), pp. 3605–3619.

[7] Claudia Merlini et al. “Electrically conductive polyaniline-coated electrospun poly (vinylidene fluoride) mats”. In: *Frontiers in Materials* 2 (2015), p. 14.

[8] Dong Nyoung Heo et al. “Development of 3D printable conductive hydrogel with crystallized PEDOT: PSS for neural tissue engineering”. In: *Materials Science and Engineering: C* 99 (2019), pp. 582–590.

[9] Koby Baranes et al. “Gold nanoparticle-decorated scaffolds promote neuronal differentiation and maturation”. In: *Nano letters* 16.5 (2016), pp. 2916–2920.

[10] Andrew R Spencer et al. “Bioprinting of a cell-laden conductive hydrogel composite”. In: *ACS applied materials & interfaces* 11.34 (2019), pp. 30518–30533.

[11] Nanoscribe. *3D Printing using Two Photon Polymerization (2PP)*. URL: `https://support.nanoscribe.com/hc/en-gb/articles/360008908273-3D-Printing-using-Two-Photon-Polymerization-2PP`.

[12] J Serbin et al. “Femtosecond laser-induced two-photon polymerization of inorganic-organic hybrid materials for applications in photonics”. In: *Optics letters* 28.5 (2003), pp. 301–303.

[13] Chee Meng Benjamin Ho et al. “3D printed microfluidics for biological applications”. In: *Lab on a Chip* 15.18 (2015), pp. 3627–3637.

[14] O Ulkir. “Design and fabrication of an electrothermal MEMS micro-actuator with 3D printing technology”. In: *Materials Research Express* 7.7 (2020), p. 075015.

[15] V Ferreras Paz et al. “Development of functional sub-100 nm structures with 3D two-photon polymerization technique and optical methods for characterization”. In: *Journal of Laser Applications* 24.4 (2012), p. 042004.

[16] Daniel Fan, Urs Staufer, and Angelo Accardo. “Engineered 3D polymer and hydrogel microenvironments for cell culture applications”. In: *Bioengineering* 6.4 (2019), p. 113.

[17] Angelo Accardo et al. “Two-photon lithography and microscopy of 3D hydrogel scaffolds for neuronal cell growth”. In: *Biomedical Physics & Engineering Express* 4.2 (2018), p. 027009. DOI: `10.1088/2057-1976/aaab93`. URL: `https://dx.doi.org/10.1088/2057-1976/aaab93`.

[18] Kestutis Kurselis et al. “3D fabrication of all-polymer conductive microstructures by two photon polymerization”. In: *Optics express* 21.25 (2013), pp. 31029–31035.

[19] Mozhdeh Imaninezhad et al. “Directed and enhanced neurite outgrowth following exogenous electrical stimulation on carbon nanotube-hydrogel composites”. In: *Journal of neural engineering* 15.5 (2018), p. 056034.

[20] Laleh Ghasemi-Mobarakeh et al. “Application of conductive polymers, scaffolds and electrical stimulation for nerve tissue engineering”. In: *Journal of tissue engineering and regenerative medicine* 5.4 (2011), e17–e35.

[21] Omid Dadras-Toussi, Milad Khorrami, and Mohammad Reza Abidian. “Femtosecond Laser 3D-printing of Conductive Microelectronics for Potential Biomedical Applications”. In: *2021 43rd Annual International Conference of the IEEE Engineering in Medicine & Biology Society (EMBC)*. IEEE. 2021, pp. 1197–1200.

[22] Marco Carlotti and Virgilio Mattoli. “Functional Materials for Two-Photon Polymerization in Microfabrication”. In: *Small* 15.40 (2019), p. 1902687.

[23] Per Brodal. *The central nervous system*. 4th ed. New York: Oxford University Press, 2010.

[24] Paola Riva, Cristina Battaglia, and Marco Venturin. “Emerging Role of Genetic Alterations Affecting Exosome Biology in Neurodegenerative Diseases”. In: *International Journal of Molecular Sciences* 20 (Aug. 2019), p. 4113. DOI: `10.3390/ijms20174113`.

[25] Suzana Herculano-Houzel. “The remarkable, yet not extraordinary, human brain as a scaled-up primate brain and its associated cost”. In: *Proceedings of the National Academy of Sciences* 109.supplement_1 (2012), pp. 10661–10668.

[26] ASU - Ask A Biologist. *Neuron Anatomy*. URL: `https://askabiologist.asu.edu/neuron-anatomy`.

[27] Yue B. “Biology of the extracellular matrix: an overview.” In: *Journal of glaucoma* (2014). DOI: `https://doi.org/10.1097/IJG.0000000000000108`.

[28] Francesca Cortini et al. “Understanding the basis of Ehlers–Danlos syndrome in the era of the next-generation sequencing”. In: *Archives of Dermatological Research* 311 (May 2019). DOI: `10.1007/s00403-019-01894-0`.

[29] Charles Nicholson and Eva Syková. “Extracellular space structure revealed by diffusion analysis”. In: *Trends in neurosciences* 21.5 (1998), pp. 207–215.

[30] Laurent Koessler et al. “In-vivo measurements of human brain tissue conductivity using focal electrical current injection through intracerebral multicontact electrodes”. In: *Hum. Brain Mapp.* 38.2 (Feb. 2017), pp. 974–986. ISSN: 1097-0193. DOI: `10.1002/hbm.23431`. eprint: `27726249`.

[31] Mai T Ngo and Brendan AC Harley. “Progress in mimicking brain microenvironments to understand and treat neurological disorders”. In: *APL bioengineering* 5.2 (2021), p. 020902.

[32] Julien Nicolas et al. “3D Extracellular Matrix Mimics: Fundamental Concepts and Role of Materials Chemistry to Influence Stem Cell Fate”. In: *Biomacromolecules* 21.6 (2020). PMID: 32227919, pp. 1968–1994. DOI: `10.1021/acs.biomac.0c00045`. eprint: `https://doi.org/10.1021/acs.biomac.0c00045`. URL: `https://doi.org/10.1021/acs.biomac.0c00045`.

[33] Kenneth M Yamada and Edna Cukierman. “Modeling tissue morphogenesis and cancer in 3D”. In: *Cell* 130.4 (2007), pp. 601–610.

[34] Tzeranis D.S et al Kourgiantaki A. “Neural stem cell delivery via porous collagen scaffolds promotes neuronal differentiation and locomotion recovery in spinal cord injury”. In: *Regen Med* (2020).

[35] F. Yang et al. “Characterization of neural stem cells on electrospun poly(L-lactic acid) nanofibrous scaffold”. In: *Journal of Biomaterials Science, Polymer Edition* 15.12 (2004). PMID: 15696794, pp. 1483–1497. DOI: `10.1163/1568562042459733`. eprint: `https://doi.org/10.1163/1568562042459733`. URL: `https://doi.org/10.1163/1568562042459733`.

[36] Bing Song et al. “Electrical cues regulate the orientation and frequency of cell division and the rate of wound healing <i>in</i> <i>vivo</i>”. In: *Proceedings of the National Academy of Sciences* 99.21 (2002), pp. 13577–13582. DOI: `10.1073/pnas.202235299`.

[37] Pu J. et al Zhao M Song B. “Electrical signals control wound healing through phosphatidylinositol”. In: *Nature* 442 (2006), pp. 457–460. DOI: `https://doi.org/10.1038/nature04925`.

[38] Zhi-yong Dong et al. “Electric field stimulation induced neuronal differentiation of filum terminale derived neural progenitor cells”. In: *Neuroscience Letters* 651 (2017), pp. 109–115.

[39] M. E. McGinnis et al R. J. Cork. “The growth of PC-12 neurites is biased towards the anode of an applied electrical field”. In: *Developmental Neurobiology* 25.12 (1994). DOI: `https://doi.org/10.1002/neu.480251204`.

[40] Brianna C Thompson et al. “Conducting polymers, dual neurotrophins and pulsed electrical stimulation—dramatic effects on neurite outgrowth”. In: *Journal of Controlled Release* 141.2 (2010), pp. 161–167.

[41] Indranil De, Prashant Sharma, and Manish Singh. “Emerging approaches of neural regeneration using physical stimulations solely or coupled with smart piezoelectric nano-biomaterials”. In: *European Journal of Pharmaceutics and Biopharmaceutics* 173 (2022), pp. 73–91. ISSN: 0939-6411. DOI: `https://doi.org/10.1016/j.ejpb.2022.02.016`. URL: `https://www.sciencedirect.com/science/article/pii/S0939641122000376`.

[42] Ma X. & Lin F Wu D. “DC Electric Fields Direct Breast Cancer Cell Migration, Induce EGFR Polarization, and Increase the Intracellular Level of Calcium Ions.” In: *Cell Biochem Biophys* 67 (2013). DOI: `https://doi.org/10.1007/s12013-013-9615-7`.

[43] Yan Huang et al Hong Cheng. “Electrical Stimulation Promotes Stem Cell Neural Differentiation in Tissue Engineering”. In: *Stem Cells International* (2021). https://doi.org/10.1155/2021/6697574.

[44] Pallavi Gupta et al. “Differential neural cell adhesion and neurite outgrowth on carbon nanotube and graphene reinforced polymeric scaffolds”. In: *Materials Science and Engineering: C* 97 (2019), pp. 539–551. ISSN: 0928-4931. DOI: `https://doi.org/10.1016/j.msec.2018.12.065`. URL: `https://www.sciencedirect.com/science/article/pii/S0928493118301954`.

[45] Yu-Shuan Chen and Ging-Ho Hsiue. “Directing neural differentiation of mesenchymal stem cells by carboxylated multiwalled carbon nanotubes”. In: *Biomaterials* 34.21 (2013), pp. 4936–4944. ISSN: 0142-9612. DOI: `https://doi.org/10.1016/j.biomaterials.2013.03.063`. URL: `https://www.sciencedirect.com/science/article/pii/S0142961213003852`.

[46] Abdalla Eltom, Gaoyan Zhong, and Ameen Muhammad. “Scaffold techniques and designs in tissue engineering functions and purposes: a review”. In: *Advances in materials science and engineering* 2019 (2019).

[47] Yudan Whulanza et al. “Sensing scaffolds to monitor cellular activity using impedance measurements”. In: *Biosensors and Bioelectronics* 26.7 (2011), pp. 3303–3308.

[48] Xifeng Liu et al. “Functionalized carbon nanotube and graphene oxide embedded electrically conductive hydrogel synergistically stimulates nerve cell differentiation”. In: *ACS applied materials & interfaces* 9.17 (2017), pp. 14677–14690.

[49] Marek Pagac et al. “A review of vat photopolymerization technology: Materials, applications, challenges, and future trends of 3d printing”. In: *Polymers* 13.4 (2021), p. 598.

[50] Jigang Huang, Qin Qin, and Jie Wang. “A review of stereolithography: Processes and systems”. In: *Processes* 8.9 (2020), p. 1138.

[51] Thomas Distler and Aldo R. Boccaccini. “3D printing of electrically conductive hydrogels for tissue engineering and biosensors – A review”. In: *Acta Biomater.* 101 (Jan. 2020), pp. 1–13. ISSN: 1742-7061. DOI: `10.1016/j.actbio.2019.08.044`.

[52] Xiang-Yu Yin et al. “3D printing of ionic conductors for high-sensitivity wearable sensors”. In: *Mater. Horiz.* 6.4 (Apr. 2019), pp. 767–780. ISSN: 2051-6347. DOI: `10.1039/C8MH01398E`.

[53] Ning Li et al. “Three-dimensional graphene foam as a biocompatible and conductive scaffold for neural stem cells”. In: *Scientific reports* 3.1 (2013), pp. 1–6.

[54] Hyunwoo Yuk et al. “3D printing of conducting polymers”. In: *Nature communications* 11.1 (2020), pp. 1–8.

[55] Yibo Wu et al. “Fabrication of conductive gelatin methacrylate–polyaniline hydrogels”. In: *Acta biomaterialia* 33 (2016), pp. 122–130.

[56] Omid Dadras-Toussi, Milad Khorrami, and Mohammad Reza Abidian. “Femtosecond Laser 3D-printing of Conductive Microelectronics for Potential Biomedical Applications”. In: (2021), pp. 1197–1200. DOI: `10.1109/EMBC46164.2021.9630885`.

[57] Amedeo Ruggiero et al. “Two-photon polymerization lithography enabling the fabrication of PEDOT: PSS 3D structures for bioelectronic applications”. In: *Chemical Communications* 58.70 (2022), pp. 9790–9793.

[58] Paola Sanjuan-Alberte et al. “Development of conductive gelatine-methacrylate inks for two-photon polymerisation”. In: *Polymers* 13.7 (2021), p. 1038.

[59] Natalia A Bakhtina et al. “Two-Photon Nanolithography Enhances the Performance of an Ionic Liquid–Polymer Composite Sensor”. In: *Advanced Functional Materials* 25.11 (2015), pp. 1683–1693.

[60] Ioannis S Chronakis, Sven Grapenson, and Alexandra Jakob. “Conductive polypyrrole nanofibers via electrospinning: electrical and morphological properties”. In: *Polymer* 47.5 (2006), pp. 1597–1603.

[61] Muhammad Ahmed Khan et al. “A Review on Biomaterials for 3D Conductive Scaffolds for Stimulating and Monitoring Cellular Activities”. In: *Applied Sciences* 9.5 (2019). URL: `https://www.mdpi.com/2076-3417/9/5/961`.

[62] Terje A Skotheim. *Handbook of conducting polymers*. CRC press, 1997.

[63] Qingsong Zhang et al. “The synthesis and characterization of a novel biodegradable and electroactive polyphosphazene for nerve regeneration”. In: *Materials Science and Engineering: C* 30.1 (2010), pp. 160–166.

[64] Nathalie K Guimard, Natalia Gomez, and Christine E Schmidt. “Conducting polymers in biomedical engineering”. In: *Progress in polymer science* 32.8-9 (2007), pp. 876–921.

[65] Christopher J Bettinger et al. “Biocompatibility of biodegradable semiconducting melanin films for nerve tissue engineering”. In: *Biomaterials* 30.17 (2009), pp. 3050–3057.

[66] Molamma P Prabhakaran et al. “Electrospun conducting polymer nanofibers and electrical stimulation of nerve stem cells”. In: *Journal of bioscience and bioengineering* 112.5 (2011), pp. 501–507.

[67] A Borriello et al. “Optimizing PANi doped electroactive substrates as patches for the regeneration of cardiac muscle”. In: *Journal of Materials Science: Materials in Medicine* 22.4 (2011), pp. 1053–1062.

[68] Natalia Gomez et al. “Micropatterned polypyrrole: a combination of electrical and topographical characteristics for the stimulation of cells”. In: *Advanced functional materials* 17.10 (2007), pp. 1645–1653.

[69] Suat Cetiner et al. “Electrospun nanofibers of polypyrrole-poly (acrylonitrile-co-vinyl acetate)”. In: *Textile research journal* 80.17 (2010), pp. 1784–1792.

[70] Smain Bousalem et al. “Synthesis, characterization and potential biomedical applications of N-succinimidyl ester functionalized, polypyrrole-coated polystyrene latex particles”. In: *Colloid and Polymer Science* 282.12 (2004), pp. 1301–1307.

[71] Maria Asplund et al. “Toxicity evaluation of PEDOT/biomolecular composites intended for neural communication electrodes”. In: *Biomedical Materials* 4.4 (2009), p. 045009.

[72] Antonio Peramo et al. “In situ polymerization of a conductive polymer in acellular muscle tissue constructs”. In: *Tissue Engineering Part A* 14.3 (2008), pp. 423–432.

[73] Shisong Nie et al. “Progress in synthesis of conductive polymer poly (3, 4ethylenedioxythiophene)(PEDOT)”. In: *Frontiers in Chemistry* (2021), p. 1137.

[74] Mohammad Ali et al. “Effects of the FeCl 3 concentration on the polymerization of conductive poly(3,4-ethylenedioxythiophene) thin films on (3-aminopropyl) trimethoxysilane monolayer-coated SiO 2 surfaces”. In: *Metals and Materials International - MET MATER INT* 15 (Dec. 2009), pp. 977–981. DOI: `10.1007/s12540-009-0977-8`.

[75] G. Zotti et al. “Electrochemical and XPS Studies toward the Role of Monomeric and Polymeric Sulfonate Counterions in the Synthesis, Composition, and Properties of Poly(3,4-ethylenedioxythiophene)”. In: *Macromolecules* 36.9 (2003), pp. 3337–3344. DOI: `10.1021/ma021715k`.

[76] Takakazu Yamamoto and Mahmut Abla. “Synthesis of non-doped poly (3, 4-ethylenedioxythiophene) and its spectroscopic data”. In: *Synthetic metals* 100.2 (1999), pp. 237–239.

[77] Aleksandr Ovsianikov Jürgen Stampfl Robert Liska. *Multiphoton Lithography: Techniques, Materials and Applications*. Wiley□VCH Verlag GmbH & Co. KGaA, 2016.

[78] Steve Ruzin and Holly Aaron. *1P vs 2P fluorescence imaging*. URL: `http://microscopy.berkeley.%20edu/courses/TLM/2P/index.html` (visited on 2021).

[79] Ada-Ioana Bunea et al. “Micro 3D Printing by Two-Photon Polymerization: Configurations and Parameters for the Nanoscribe System”. In: *Micro* 1.2 (2021), pp. 164–180. URL: `https://www.mdpi.com/2673-8023/1/2/13`.

[80] Jing Qu et al. “Stiffness, strength and adhesion characterization of electrochemically deposited conjugated polymer films”. In: *Acta Biomater.* 31 (Feb. 2016), p. 114. DOI: `10.1016/j.actbio.2015.11.018`.

[81] V. Nguyen and P. Lee. “Resistive Switching Memory Phenomena in PEDOT PSS: Coexistence of Switchable Diode Effect and Write Once Read Many Memory”. In: *Scientific Reports* 6 (2016), p. 19594. DOI: `10.1038/srep19594`.

[82] Alireza Moazzeni, Samaneh hamedi, and Zoheir Kordrostami. “Switching characteristic of fabricated nonvolatile bipolar resistive switching memory (ReRAM) using PEDOT: PSS/GO”. In: *Solid-State Electronics* 188 (2022), p. 108208. ISSN: 0038-1101. DOI: `https://doi.org/10.1016/j.sse.2021.108208`. URL: `https://www.sciencedirect.com/science/article/pii/S0038110121002513`.

[83] Y. Liu et al. “Precise 3D printing of micro/nanostructures using highly conductive carbon nanotube-thiol-acrylate composites”. In: 9738 (2016). Ed. by Bo Gu, Henry Helvajian, and Alberto Piqué, p. 973808. DOI: `10.1117/12.2214862`. URL: `https://doi.org/10.1117/12.2214862`.

[84] Leona V. Lingstedt et al. “Effect of DMSO Solvent Treatments on the Performance of PEDOT:PSS Based Organic Electrochemical Transistors”. In: *Advanced Electronic Materials* 5.3 (), p. 1800804. DOI: `https://doi.org/10.1002/aelm.201800804`. eprint: `https://onlinelibrary.wiley.com/doi/pdf/10.1002/aelm.201800804`. URL: `https://onlinelibrary.wiley.com/doi/abs/10.1002/aelm.201800804`.

[85] Ehsan Hosseini, Vinayaraj Ozhukil Kollath, and Kunal Karan. “The key mechanism of conductivity in PEDOT:PSS thin films exposed by anomalous conduction behaviour upon solvent-doping and sulfuric acid post-treatment”. In: *J. Mater. Chem. C* 8 (12 2020), pp. 3982–3990. DOI: `10.1039/C9TC06311K`. URL: `http://dx.doi.org/10.1039/C9TC06311K`.

A

Appendix A: Backup Plans

A.1. Plan B - Cyclic voltammetric deposition of PEDOT PSS

As shown in figure A.1, First, the base structure, IP-L or IP-Dip, is printed and later on, EDOT: PSS is polymerized onto the microstructure by an electrochemical method, cyclic voltammetry, using a potentiostat [57]

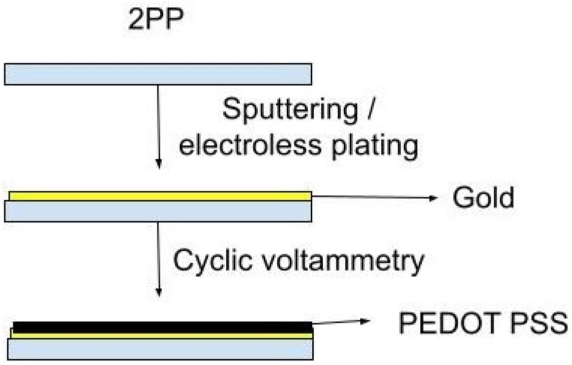

Figure A.1: Illustration of Plan B, PEDOT: PSS coating on 2PP printed microstructres

This is similar to the chemical oxidation of EDOT, but the electric potential is used here as a driving factor. An applied voltage oxidizes EDOT during electro-polymerization, and polymerization occurs at the electrode. A three-electrode setup (counter electrode, reference electrode, and working electrode) and electrolyte solution are required for electrochemical polymerization of EDOT, Fig 2.20. As electrolytes, small molecules are used in solutions like lithium perchlorate (LiClO4), 1-butyl-3-methylimidazolium hexaphonate (BMIMPF6), and lithium bis (trifluoromethosulfonyl) amide (LiTFSI).

To ensure that EDOT deposits onto the structure, the structure must first be conductive. For that, a gold layer is deposited on it. It can be done in 2 ways, Sputtering and electroless plating. Firstly, the sputtering is used for 2D and 2.5D structures to assess the plan's viability. In the case of sputtering, theoretically, the deposition will be uniform in 2D and simple 3D structures. When fabricating 3D structures, sputtering is tried out and accessed. If the coating is deemed non-uniform via morphological assessment, SEM, then electroless plating is implemented. In electroless plating, the deposition will be uniform, with the drawback being an additional chemical step, electroless plating, added to the plan B protocol. The same characterisation methods as plan A are implemented here as well.

Risk analysis(plan B):

- Non-uniform gold coating on the microstructure. This can happen in complex microstructures.

If that happens, an electroless 2PP fabricated structures protocol will be developed. And if this protocol fails, further steps of plan B cannot be implemented.

- Failure to polymerise EDOT onto the gold-coated structure. This can happen due to incorrect potential differences and electrolytes while using the potentiostat.
- Failure to connect the microstructure to the potentiostat.

A.2. Plan C - Photo Polymerisation of PEDOT TMA on base structure

The base structure is printed, IP-L or IP-Dip, and rinsed. Then, PEDOT-TMA (PEDOT -Tetramethacrylate) liquid and photoinitiator mixture is dropped on the structure. Since IP resin and TMA are acrylate-based, in theory, there will be photo polymerisation between the exposed acrylates of microstructure and those in TMA once exposed to a UV source. This potentially results in forming a conductive PEDOT-TMA layer on the microstructure, Fig A.2. The verification and characterisation procedure is the same as in plan A.

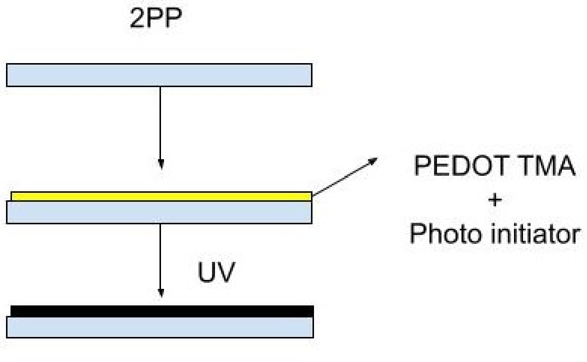

Figure A.2: Illustration of Plan C, Photo-polymerisation of PEDOT-TMA on 2PP printed scaffolds

Risk analysis (plan C):

- Weak bonding of structure and PEDOT TMA can happen due to failure to crosslink acrylates in TMA and microstructure.
- Failure to polymerise PEDOT TMA
- Change in porosity of microstructure can happen due to the formation of PEDOT TMA meniscus on the structure.

A.3. Plan D - PEDOT PSS nanofibril infused resin

In this plan, the conductive PEDOT PSS in freeze-dried nanofibrils is infused in IP-L, and then the microstructure is printed, Fig A.3. To obtain the PEDOT: PSS nanofibrils, PEDOT: PSS aqueous solution is freeze-dried (−80 °C) for 12 - 24h and lyophilized [8]. Lyophilisation removes water from a frozen product and places it under a vacuum, allowing the ice to transition directly from solid to vapour without going through a liquid phase for 1 - 3 days. The verification and characterisation procedure is the same as in plan A. Mixing of nanofibrils and IP-L is done by using mechanical stirring and sonication.

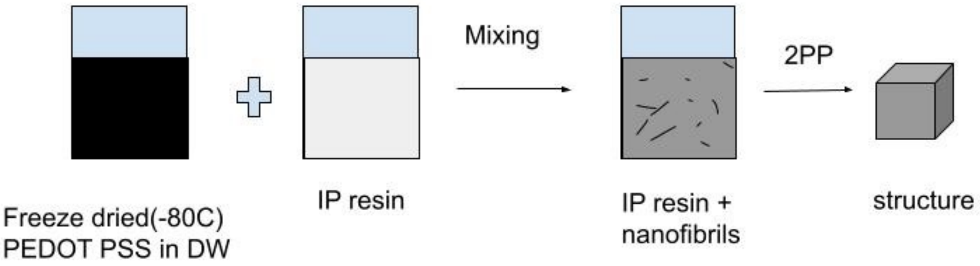

Figure A.3: Illustration of Plan D

Risk analysis (plan D):

- Failure to create nanofibrils. This can happen due error in temperature monitoring of PEDOT PSS.
- Failure to mix IP-L and nanofibrils, since the photoresist is highly viscous, the mixing is done by increasing entropy mechanically(stirring). The idle time after stirring can settle down the fibrils.
- Failure to 2PP the mixture. This can be due to the interruption of the laser by nanofibrils in the resin. The laser power has to be optimised to print this mixture. The transparency of this mixture will also be an issue since PEDOT is black. Thus the shallow concentration of PEDOT PSS nanofibrils is used.

B

Appendix B: Printing in 63x Oil configuration

B.1. Fabrication of pedestal

Figure B.1: Mixing of resin IP-L and EDOT, before and after 2 min vortexer and 2 hour of sonication

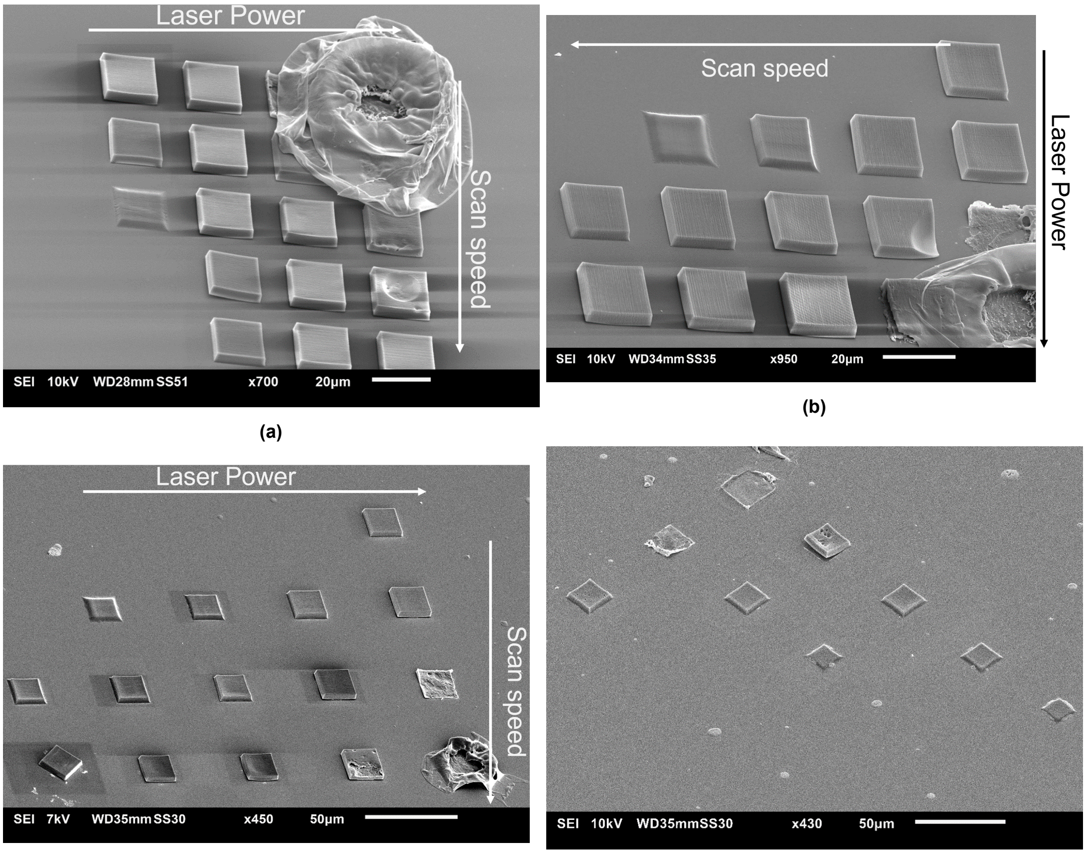

(a) (b) (c) (d)

Figure B.2: 63x Oil configuration dose test, (a) IP-L (control), (b) 5% EDOT, (c) 10% EDOT, (d) 15% EDOT

Laser Power: 10 - 50 mW
Scan speed: 10 - 90 mm/s
Hatching distance:0.2 μm
Slicing distance: 0.2 μm
Optimal dose: , 40 mW 30 mm/s (15% doping), 30 mW 10 mm/s (rest)

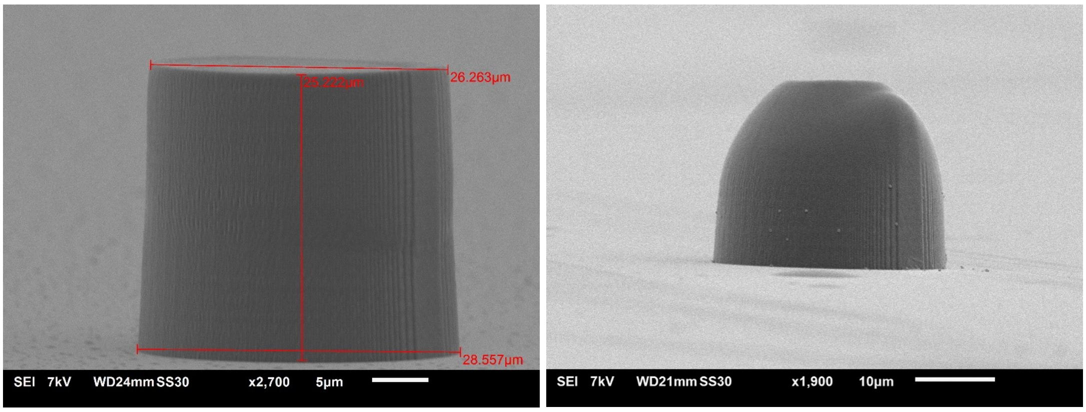

(a) (b)

Figure B.3: 30x30x30 μm^3 Cylinder, (a) IP-L (control), (b) 5% EDOT

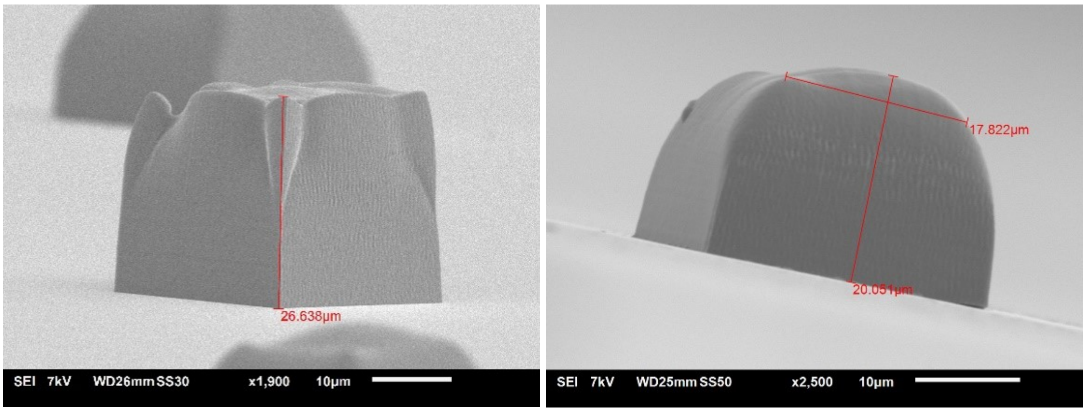

(a) (b)

Figure B.4: 30x30x30 μm^3 pedestal, (a) IP-L (control), (b) 5% EDOT

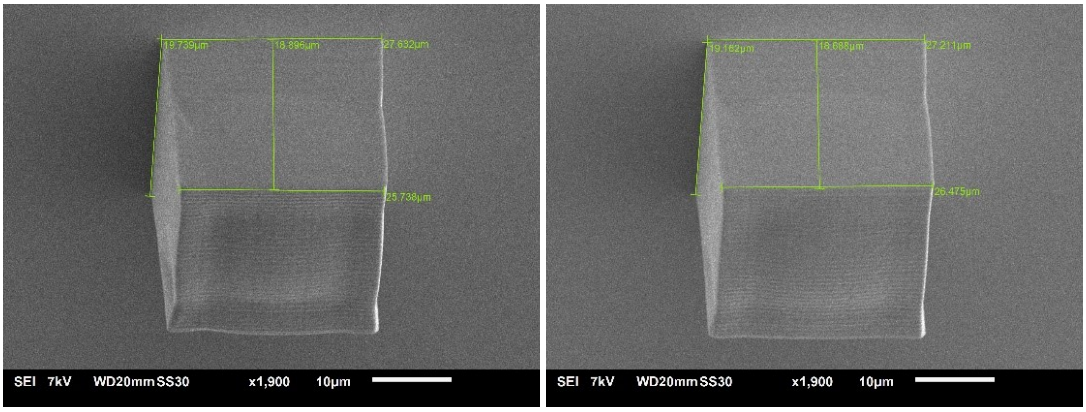

(a) (b)

Figure B.5: 63x Oil configuration, 30x30x30 μm^3 pedestal printed in IP-L with powerslope, (a) 0.01, (b) 0.02

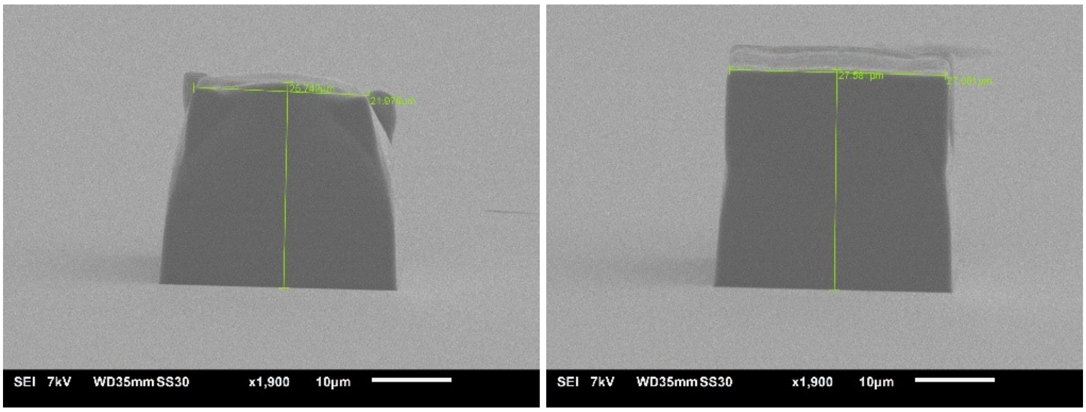

(a) (b)

Figure B.6: 63x Oil configuration, 30x30x30 μm^3 pedestal printed in 5% EDOT with powerslope, (a) 0.01, (b) 0.02

Through trial and error, it is found that powerslope 0.02 give a suitable pedestal for mechanical characterisation. (figure.B.6, B.5)

Since the resin, IP-L is viscous, printing structures from top to bottom might be possible. This will eliminate the problem of shadowing. It is observed that the structures are true to design if the laser power and the scan speed are high. (figure B.8 and B.7)

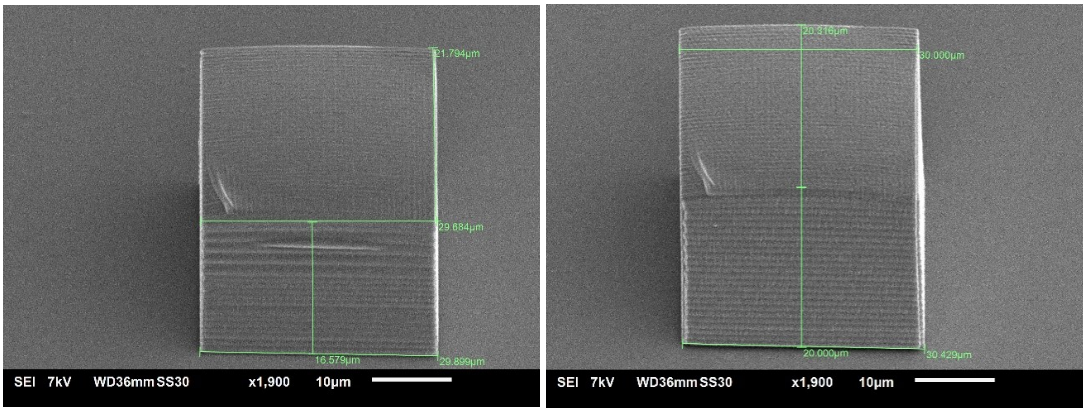

(a) (b)

Figure B.7: 63x Oil configuration, 30x30x30 μm^3 pedestal printed top-down in IP-L with laser exposure of (a) 30 mW 15mm/s, (b) 40mW 30mm/s

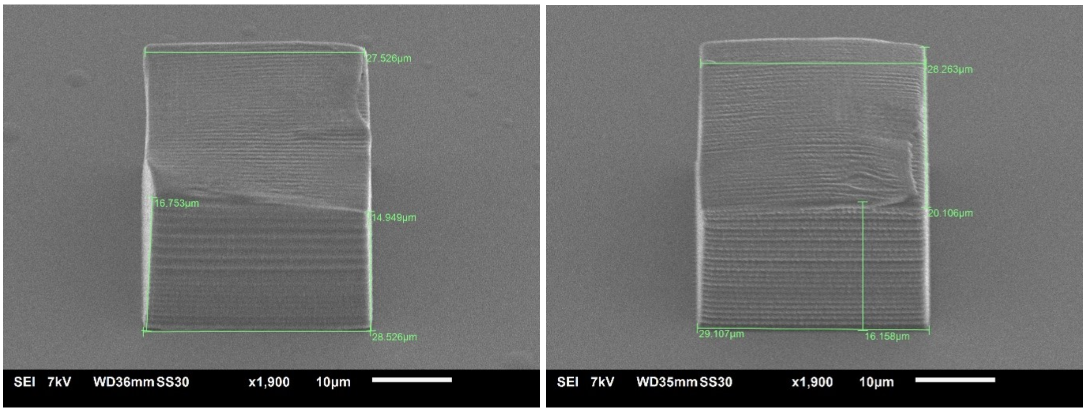

(a) (b)

Figure B.8: 63x Oil configuration, 30x30x30 μm^3 pedestal printed top-down in IP-L with laser exposure of (a) 30 mW 15mm/s, (b) 40mW 30mm/s

B.1.1. Mechanical characterisation

The mechanical characterisation is performed for all seven conditions, Control, doped and chemically polymerised for four sets of laser parameters. As the doping level increases, Young's modulus decreases, the figure B.9 shows, and it increases as the laser dosage increases (figure B.10).

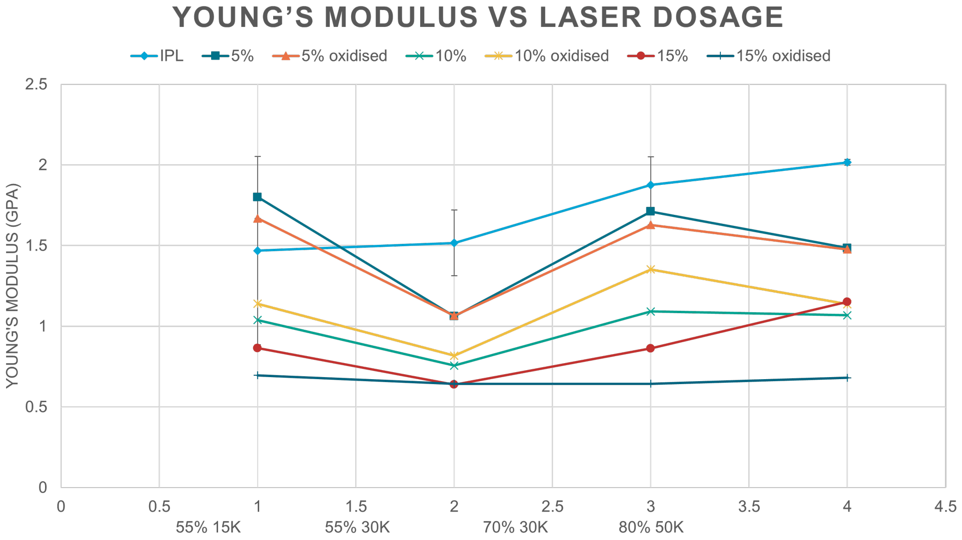

Figure B.9: Mechanical characterisation Summarized.

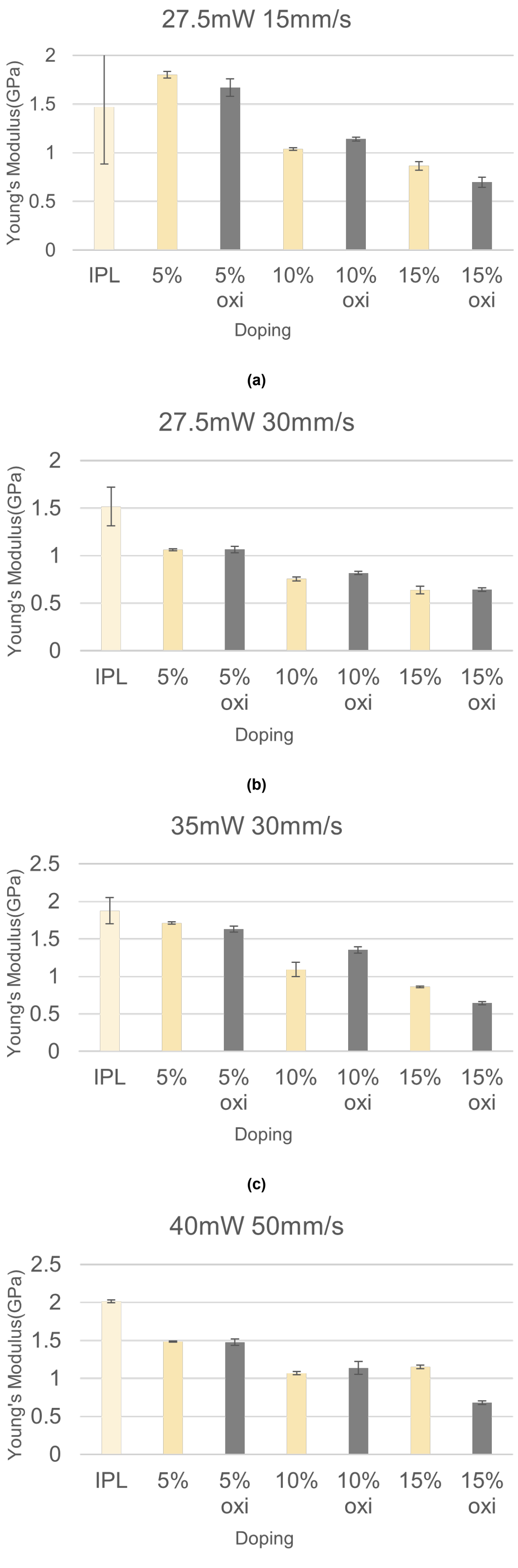

(a)

(b)

(c)

(d)

Figure B.10: Mechanical characterisation for individual laser exposure, (a) Laser power 27.5 mW, scan speed 15mm/s, (b) Laser power 27.5 mW, scan speed 30mm/s, (c) Laser power 35 mW, scan speed 30mm/s, (d) Laser power 40 mW, scan speed 50mm/s

B.2. Fabrication of 3D microstructures

B.2.1. Unit cell

While printing 3D microstructures, it is observed that shadowing has a significant effect on higher structures. The figure shows the difference between a structure printed with Powerslope and one with the top-down approach (figure’B.11).

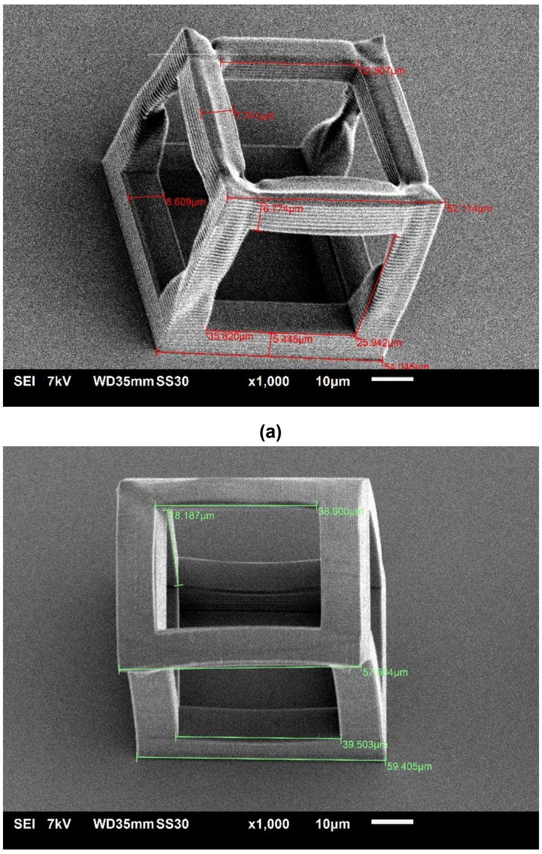

(a)

(b)

Figure B.11: Unit cell of beam thickness $10\mu m$ and pore size of $40\mu m$ printing in IP-L using (a) Powerslope 0.02, (b) Top-down printing

Various approaches are used to compensate for the shadowing and have a stable 3D microstructure.

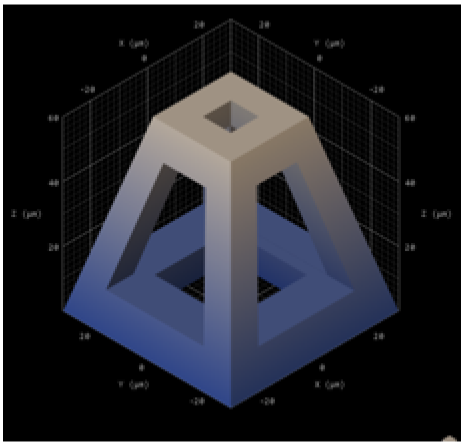

Figure B.12: Pyramid-shaped unit cell design

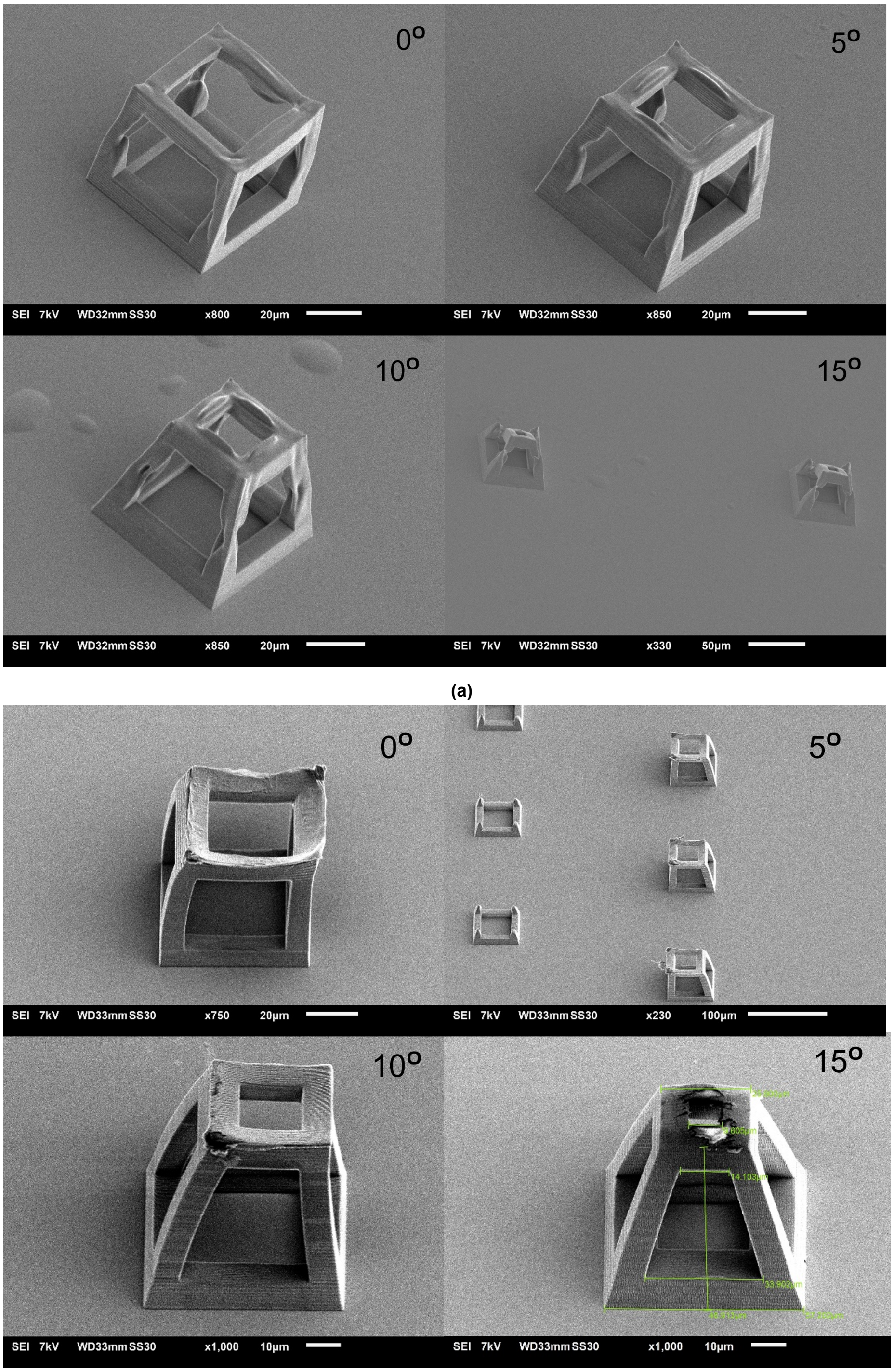

Figure B.13: Unit cell printed in IP-L. (a) Powerslope, as the angle increases, the beams start thinning and collapse. (b) In top-down printing, the topmost layer becomes smaller as the angle increases. Since those layers are printed first, the smaller the topmost section, the more design-like it is printed

Since the beam thins as the height increases, a design is made to uniformly increase the width of the pillar by giving it an inward angle, figure B.14. It is observed that though the middle section of the pillar thins, it thickens as the inward angle increases, figure.B.15.

Figure B.14: Unit cell design with an inward angle on the pillar

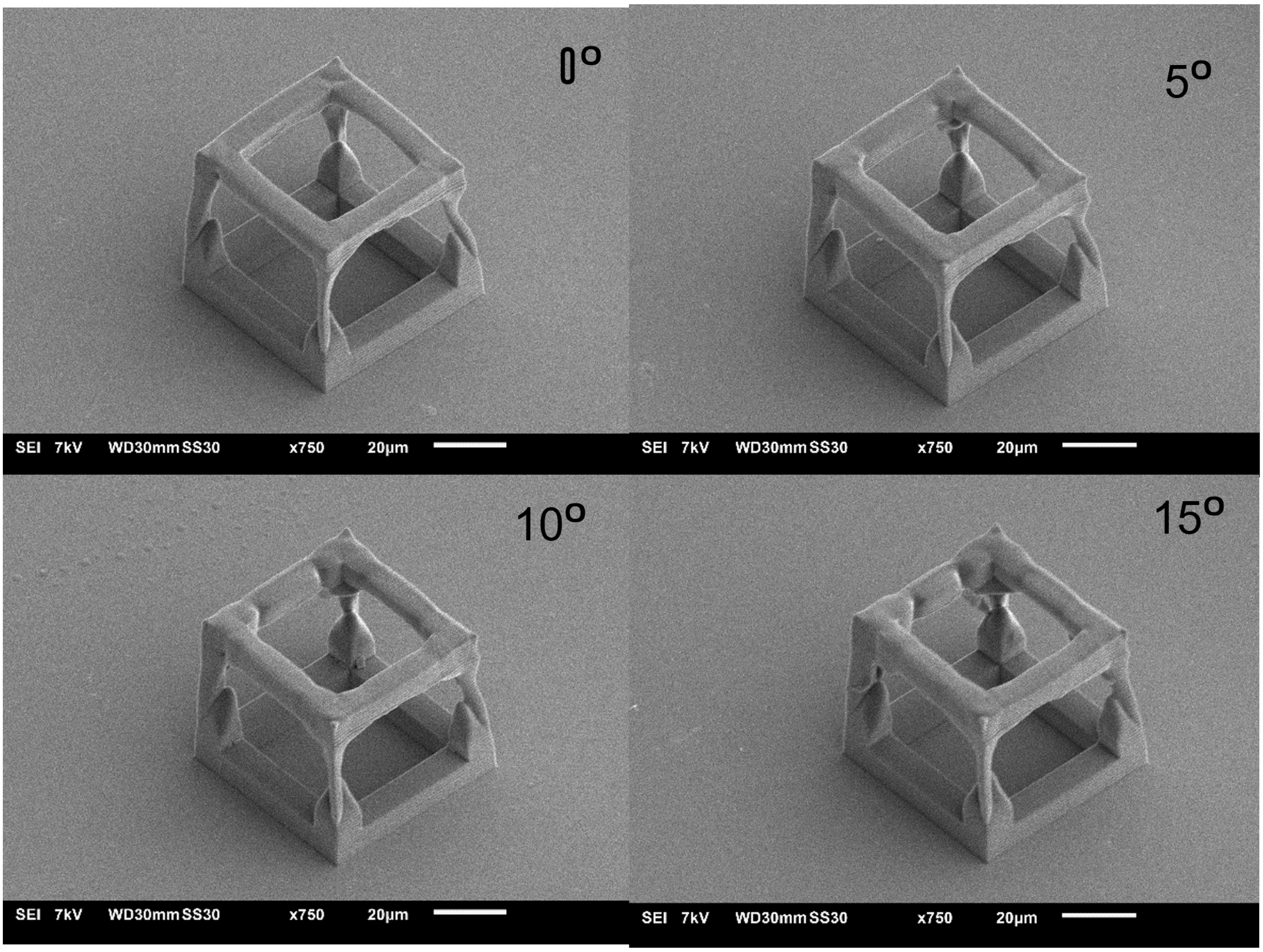

Figure B.15: SEM image of Unit cell design with increasing inward angle on the pillar

As the base will also contribute to the shadowing of the pillars. A design without the base and an increasing inward angle is printed in the figure.B.16. It is observed as the angle increases, there is a dip forming in the middle of the pillar. This is due to the laser being defocused in the middle due to the printed part below, whereas the outer part is not hindered as there is no solid material underneath.

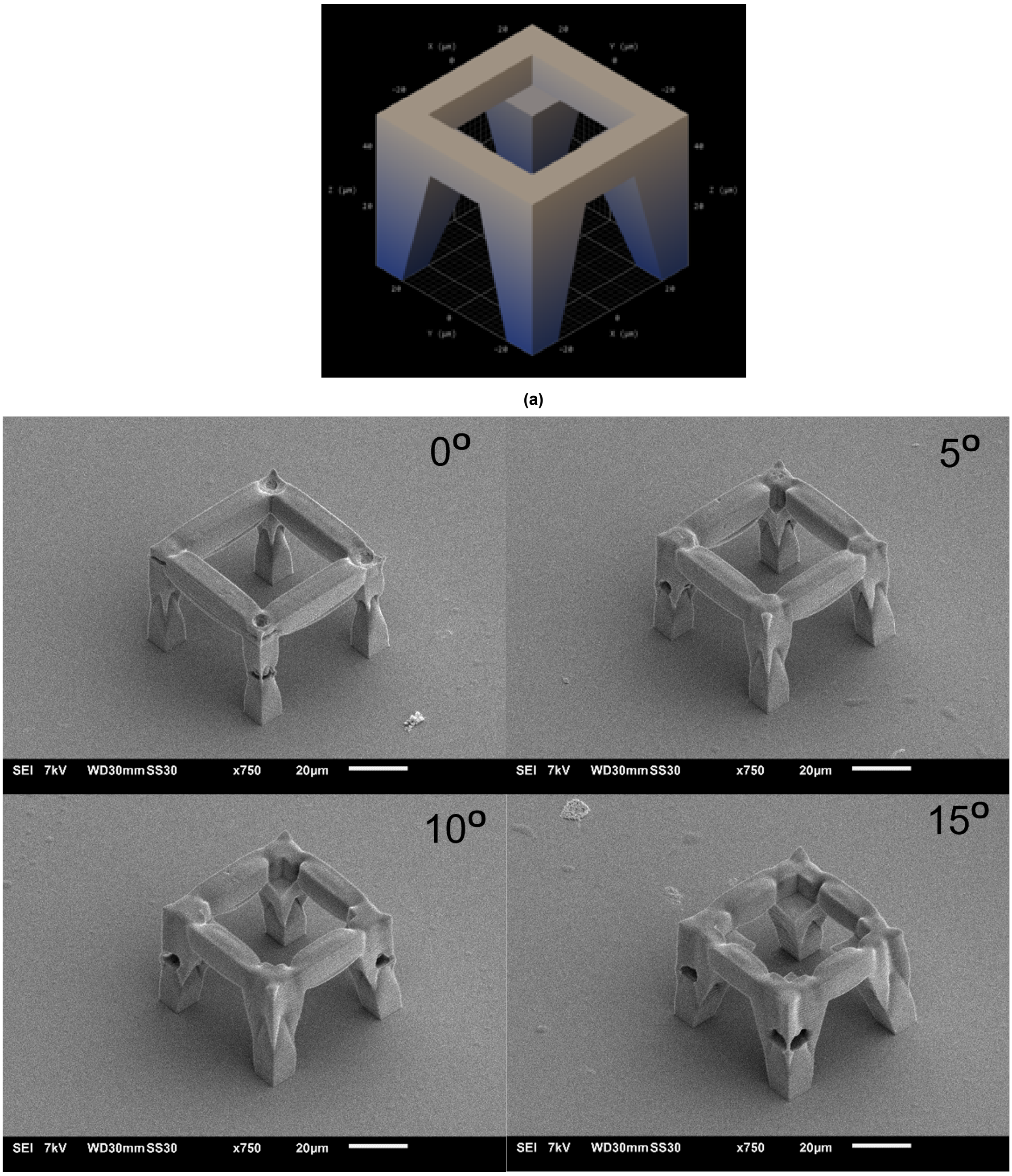

(a)

(b)

Figure B.16: (a) Unit cell design without base, (b) SEM images of unit cell without base with an inward, increasing angle on the pillar printed in IP-L

B.2.2. 3D Cage

To compensate for the shadowing in a 3D complex structure, the pillars in each row are given a larger taper than the previous row, i.e. $2, 4, 6°$, figure.B.17 (a). A small 3D cage of total height $40 \mu m$ is observed to be stable, but higher structures are deformed in figure B.17(b).

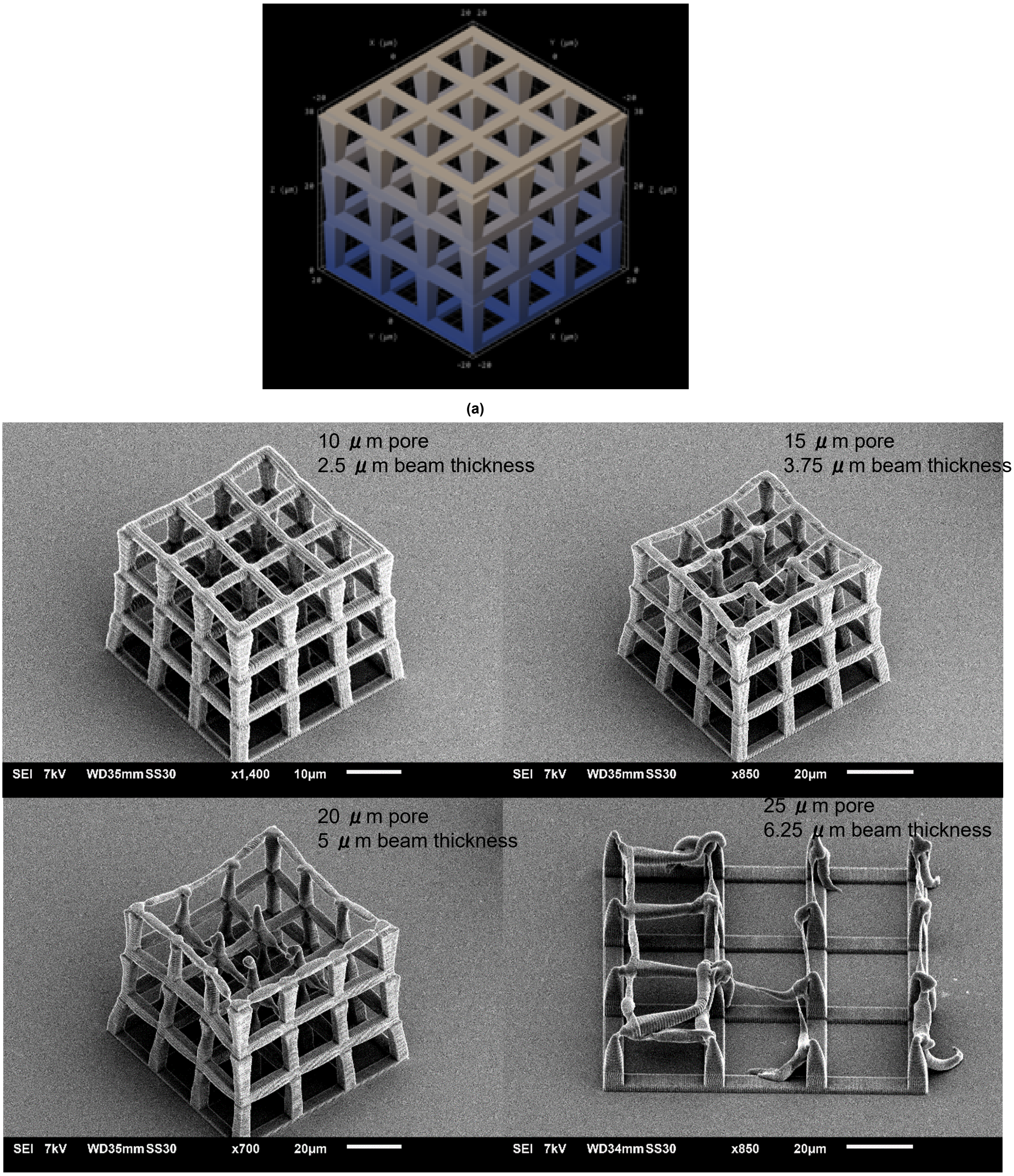

(a)

(b)

Figure B.17: 3D cage with increasing taper on the pillar (a) Design, (b) SEM image of printed structure with power slope 0.02 printed in 5% EDOT

In this iteration, an additional function defocusfactor (1.2) along with powerslope 0.02 is used to adjust the focus of the laser through the program, figure.B.18, no visible difference is observed.

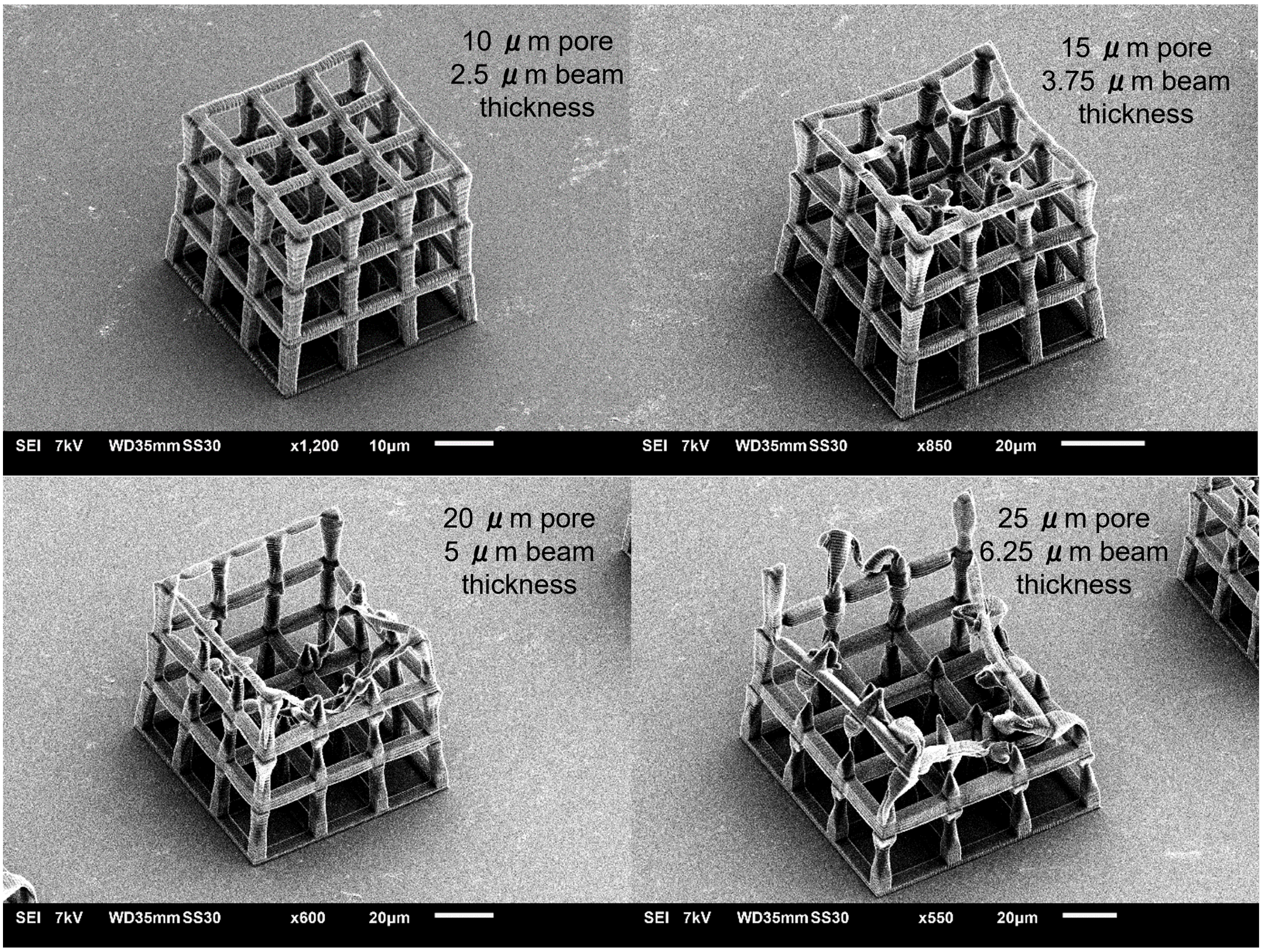

Figure B.18: 3D cages printed with defocusfactor(1.2) and powerslope (0,02)

To have a stable print in 63x Oil configuration, powerslope and defocus factor are optimised for each design as the deviation in laser path through the structure depends on the structure's design.

C

Appendix C: Electrical characterisation

C.1. Bulk sample

The oxidative polymerised droplets are electrically charachteised to obtain the qualitative behaviour of the PEDOT doped IP-L. Two point probe mode was used to conduct this experiment. It is observed that this bulk sample has a similar hysteresis behaviour but the striking difference is that the bulk samples give much smoother response and current is 6 mA for 20% EDOT doped IP-L, which is 50x higher than 2PP printed structure in 15% EDOT resin.

(a) (b)

Figure C.1: (a)UV polymerized IP L EDOT 5%, (b) Oxidative polymerized IP-L PEDOT 5%

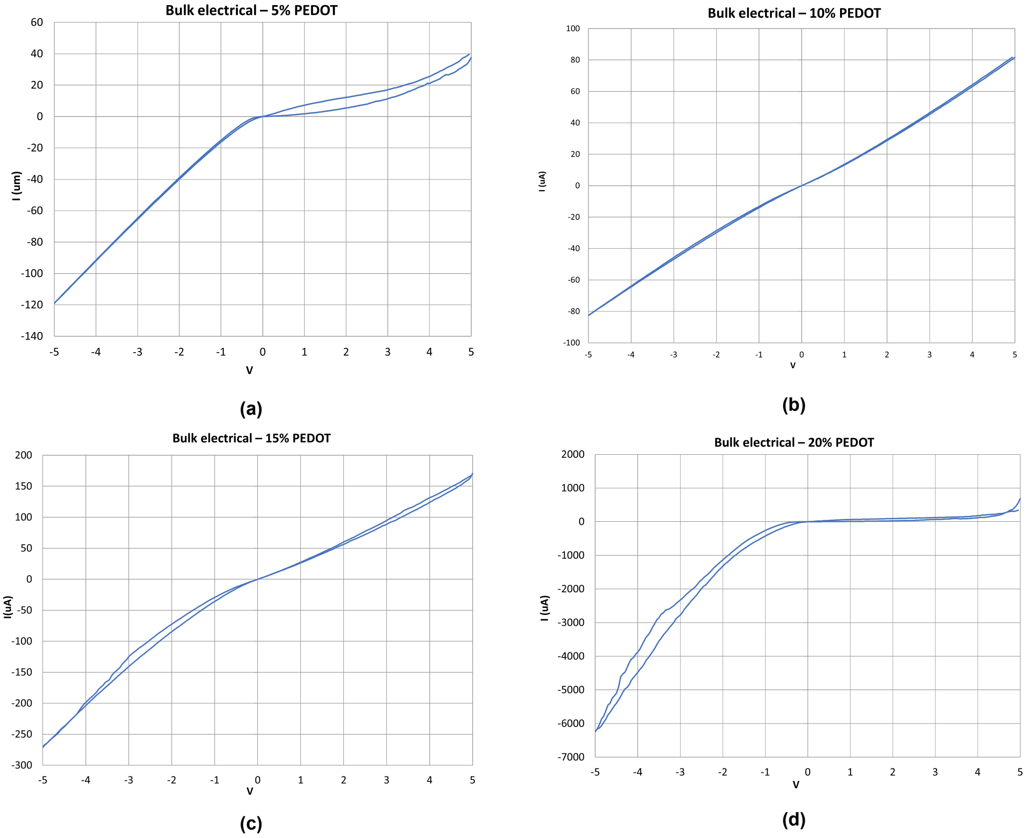

(a)

(b)

(c)

(d)

Figure C.2: 2-point probe, IV sweeps on oxidative polymerised droplets, (a) EDOT 5%, (b) EDOT 10%, (c) EDOT 15%, (d) EDOT 20%

C.2. 25x Oil

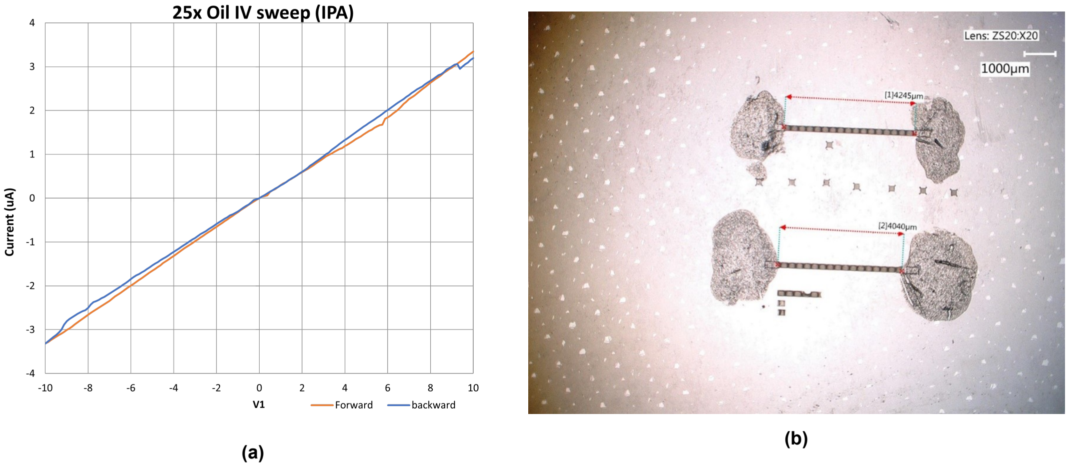

(a)

(b)

Figure C.3: 25x Oil mode printed $5mmx200\mu mx15\mu m$ line (Hatch offset 0)IPA treated with silver paste on ends, (a) 2-point IV sweep with silver paste, (b) Optical image of the structure

C.3. 25x Dill

The electrical behaviour caused due to factors are discussed in this section.

C.3.1. Solvent Treatment

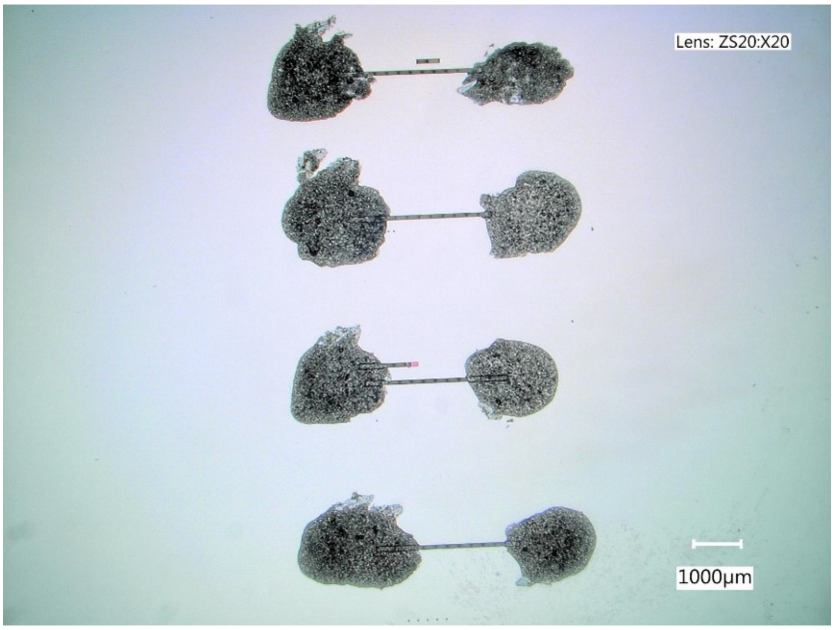

Figure C.4: 2 probe IV sweeps, IPA 3 min

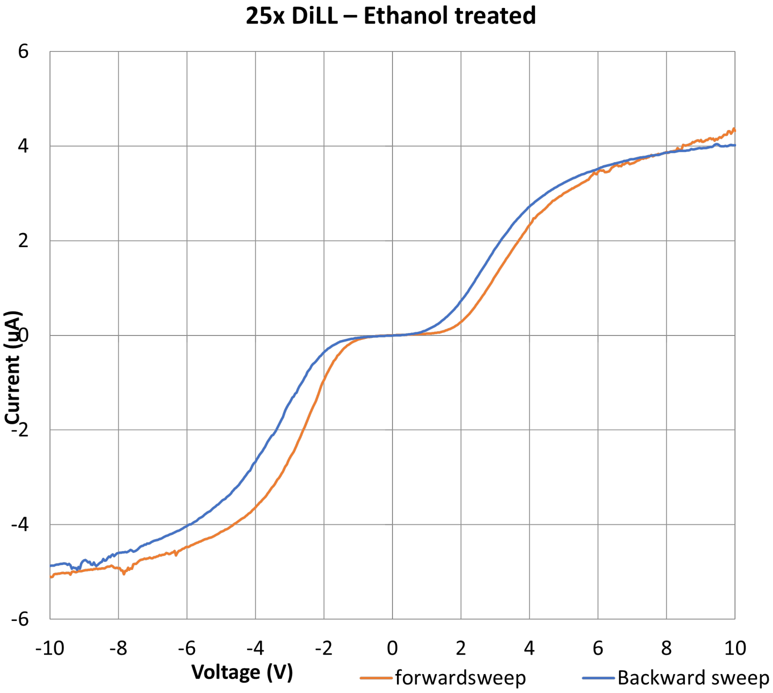

Figure C.5: 2 probe IV sweeps, Ethanol 3 min

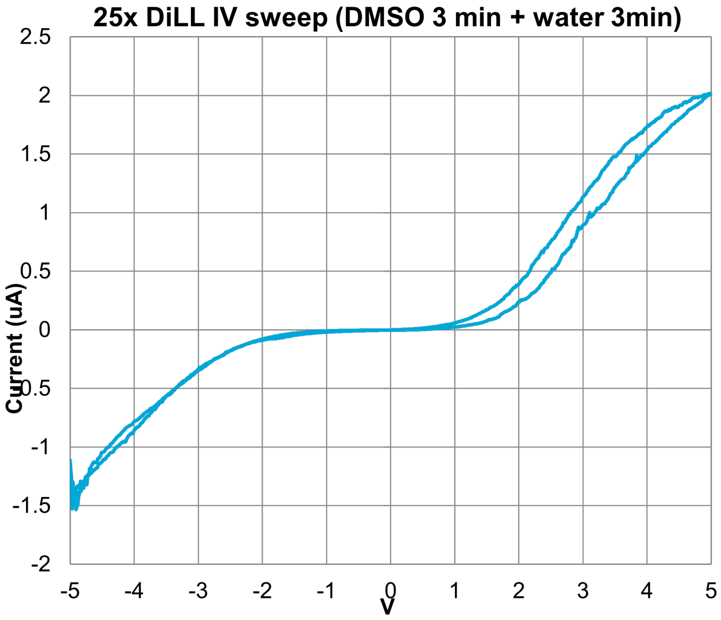

Figure C.6: 2 probe IV sweeps, DMSO 3 min, water 3 min. 5V bias

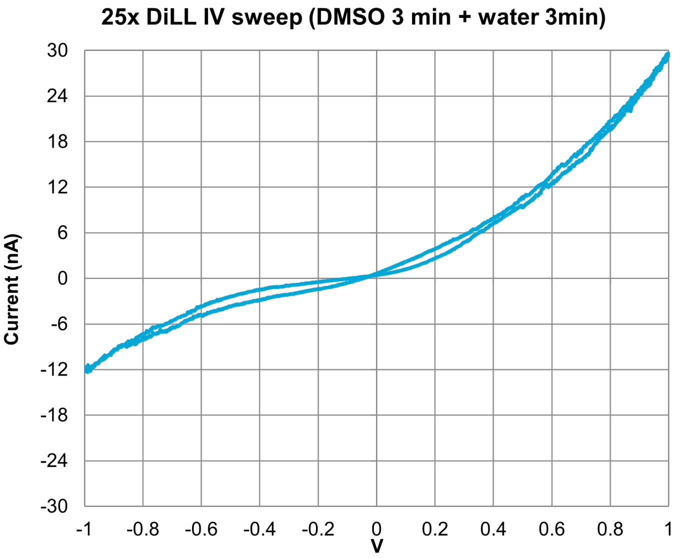

Figure C.7: 2 probe IV sweeps, DMSO 3 min, water 3 min. 1 V bias

C.3.2. Printing parameters

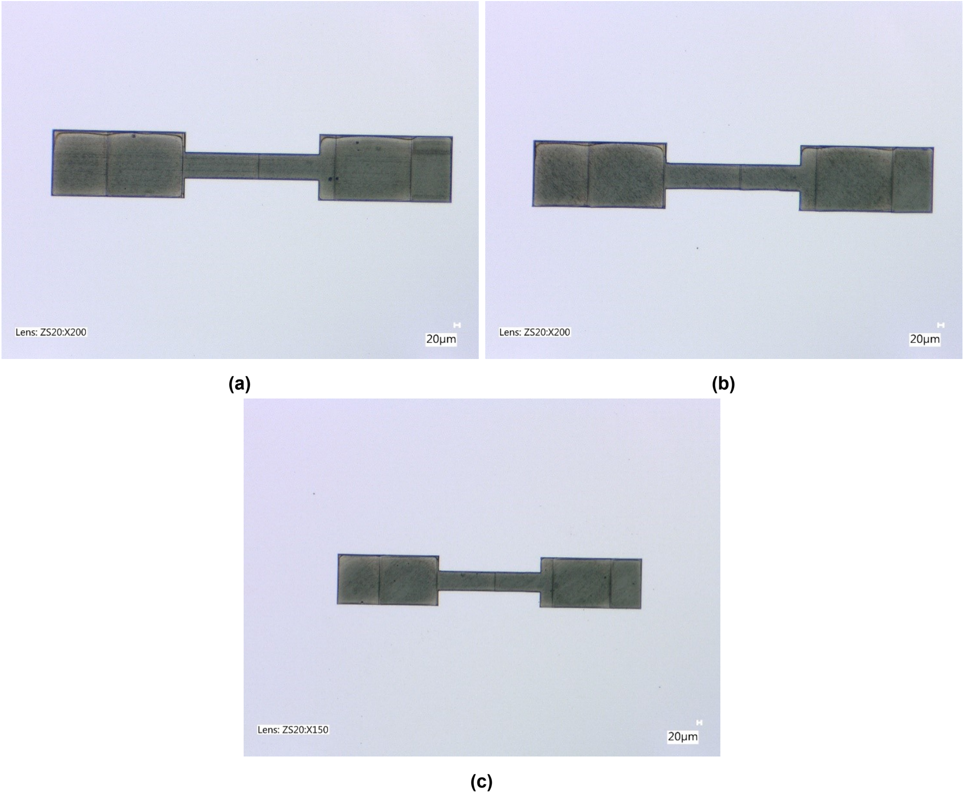

(a) (b) (c)

Figure C.8: Optical image of 2-point structure with varying hatch and offset solvent treated with DMSO 25%. (a) Hatch 90, Offset 0, (b) Hatch 45, Offset 0, (c) Hatch 45, Offset 90

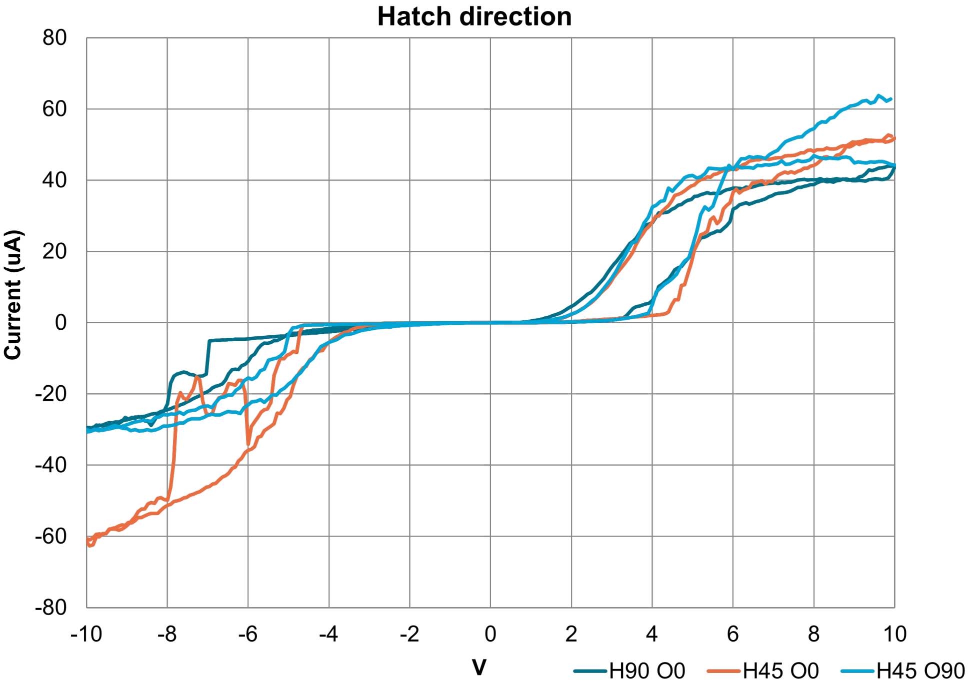

Figure C.9: 2 point IV sweep. Effect of hatch direction and hatch offset, H=Hatch, O = offset, DMSO 25%

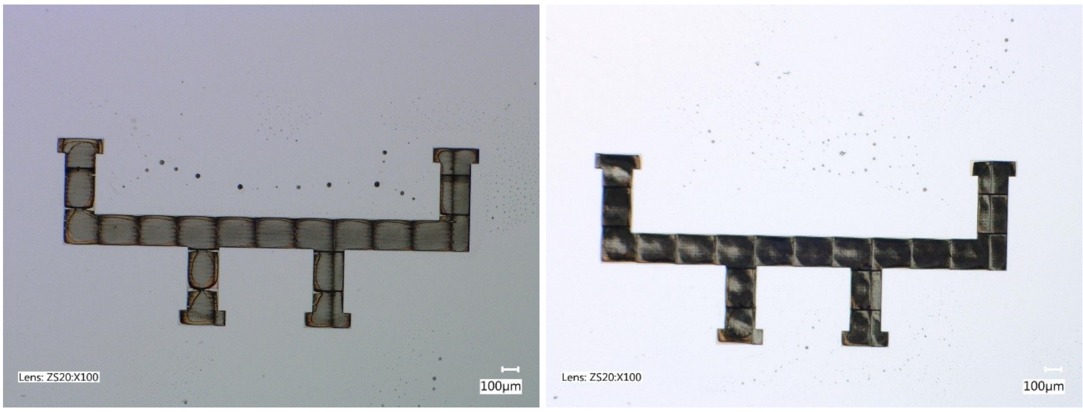

(a) (b)

Figure C.10: 4-point probe, Pi structure with varying hatch and offset, DMSO 25% solvent treatement. (a) Hatch 90°, Offset 0°, (b) Hatch 45°, Offset 90°

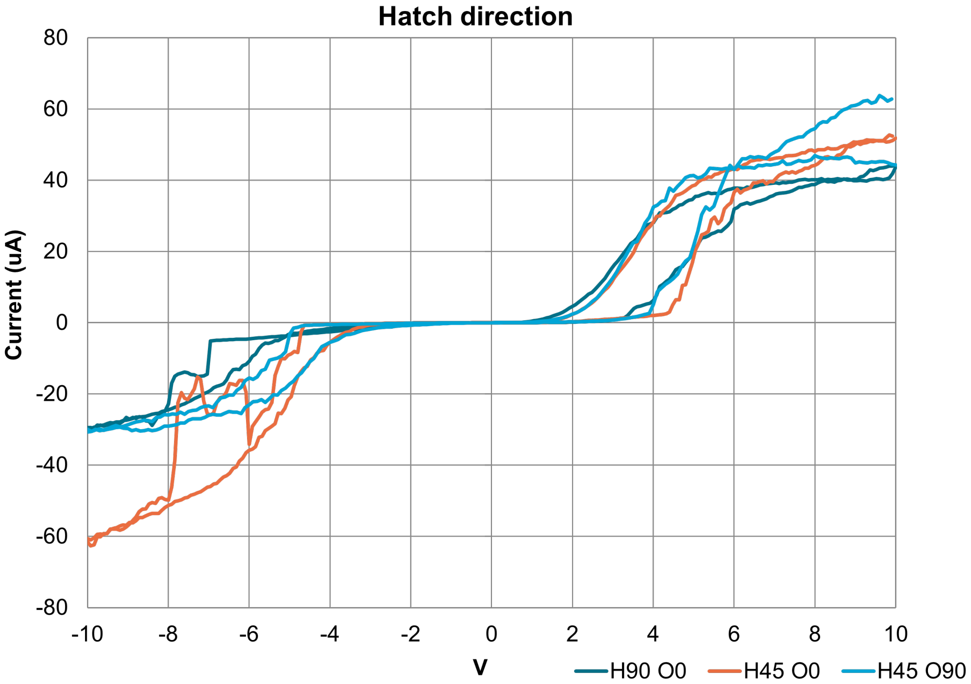

Figure C.11: 4-point probe IV sweep, Effect of hatch direction and hatch offset, H=Hatch, O = offset, DMSO 25%

C.3.3. PBS treated micro structures

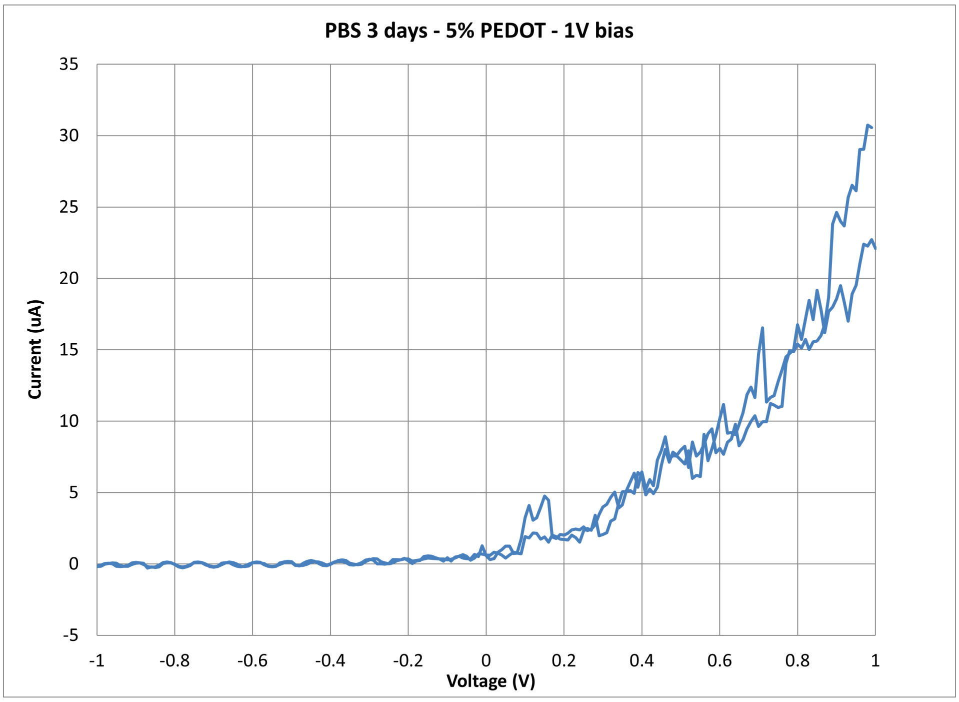

(a)

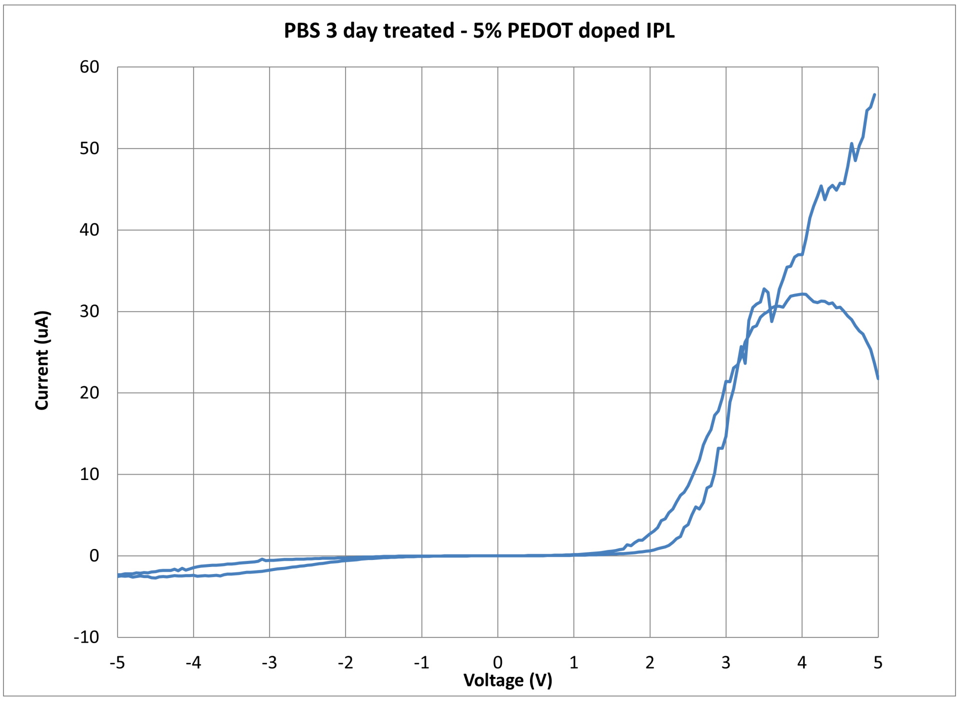

(b)

Figure C.12: 2-point IV sweep of 3 days PBS treated 5% doped microstructure. (a) 1 V bias, (b) 5 V bias

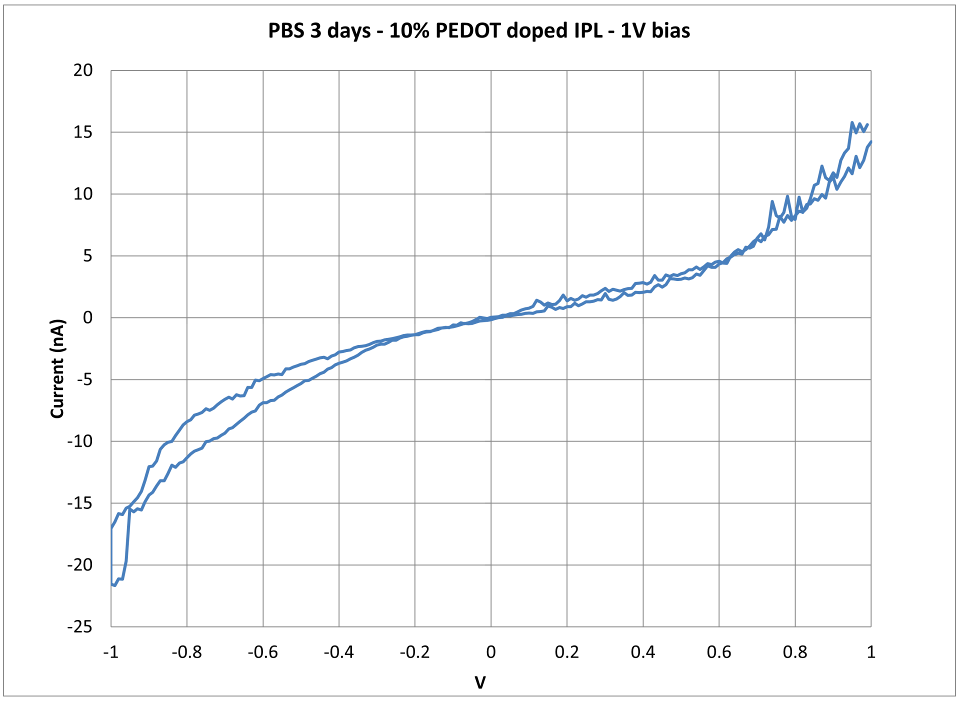

(a)

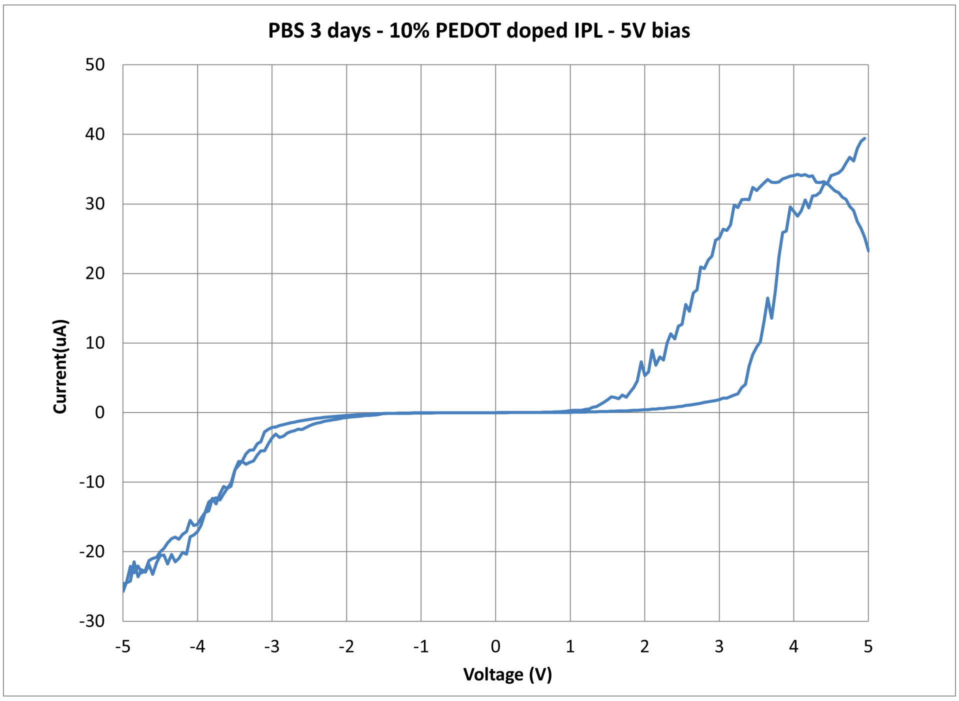

(b)

Figure C.13: 2-point IV sweep of 3 days PBS treated 10% doped microstructure. (a) 1 V bias, (b) 5 V bias

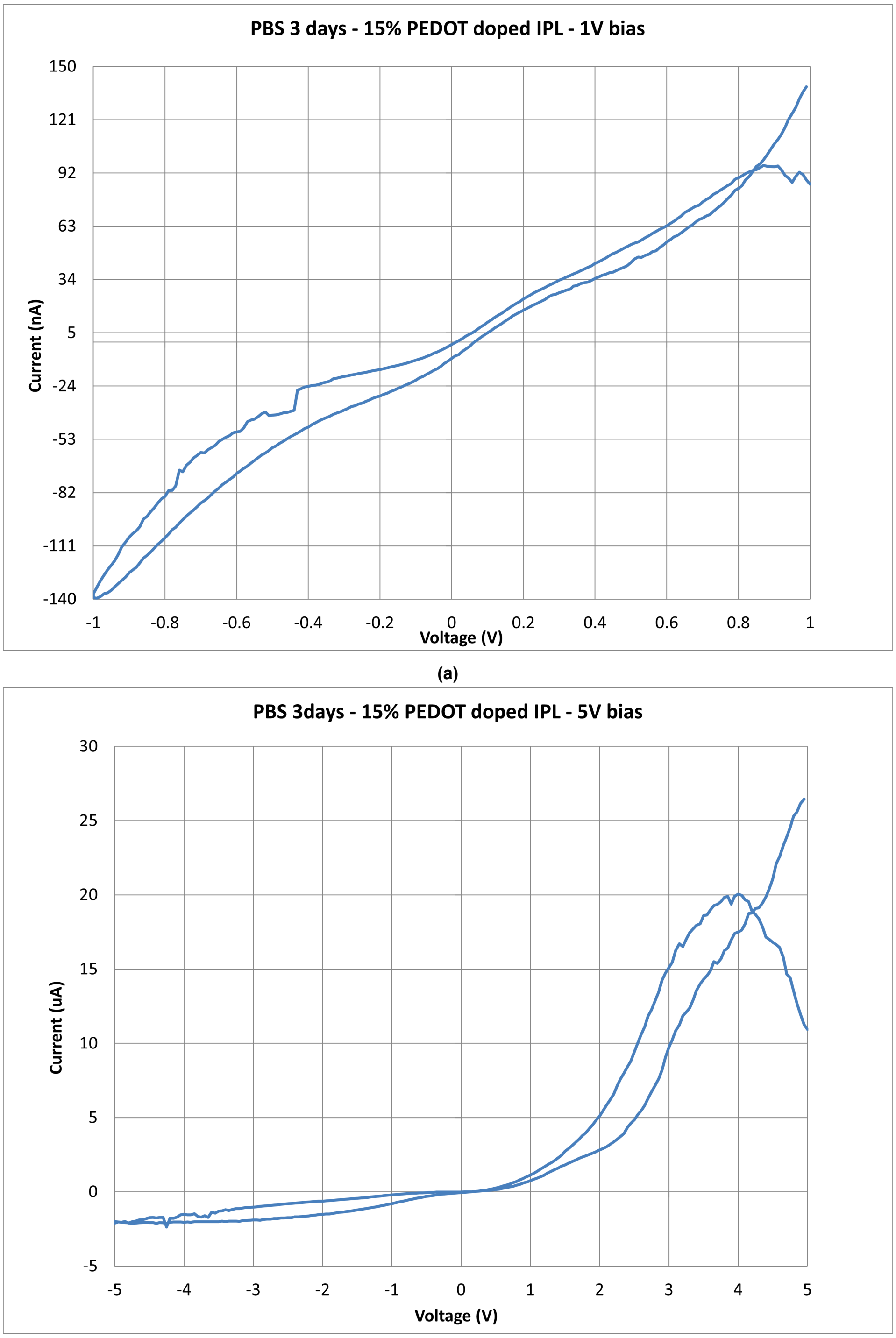

(a)

(b)

Figure C.14: 2-point IV sweep of 3 days PBS treated 15% doped microstructure. (a) 1 V bias, (b) 5 V bias

C.3.4. Conductivity measurement of prints on gold pads

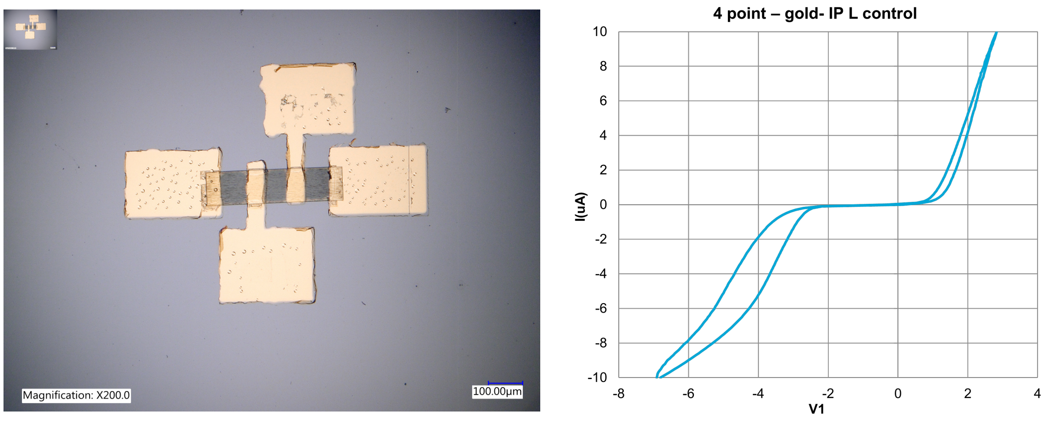

(a) **(b)**

Figure C.15: (a) 4-point probe on gold pads IP L, (b) IV sweep

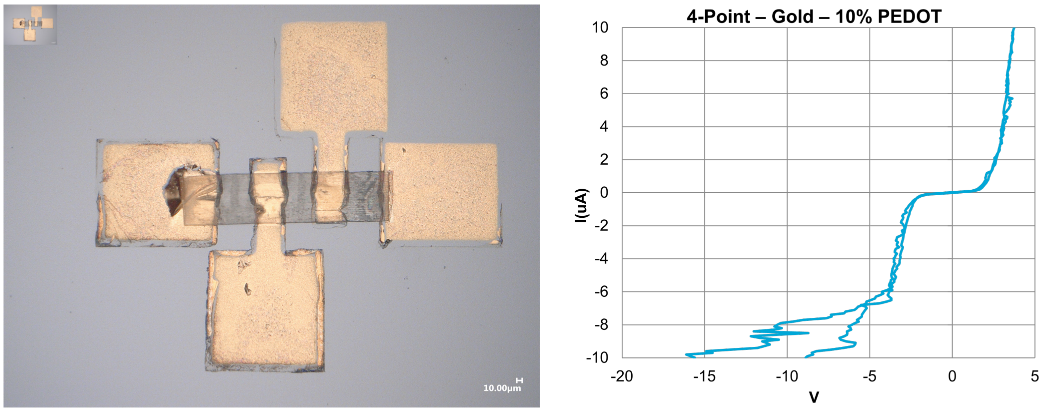

(a) **(b)**

Figure C.16: (a) 4-point probe on gold pads PEDOT 10%, (b) IV sweep

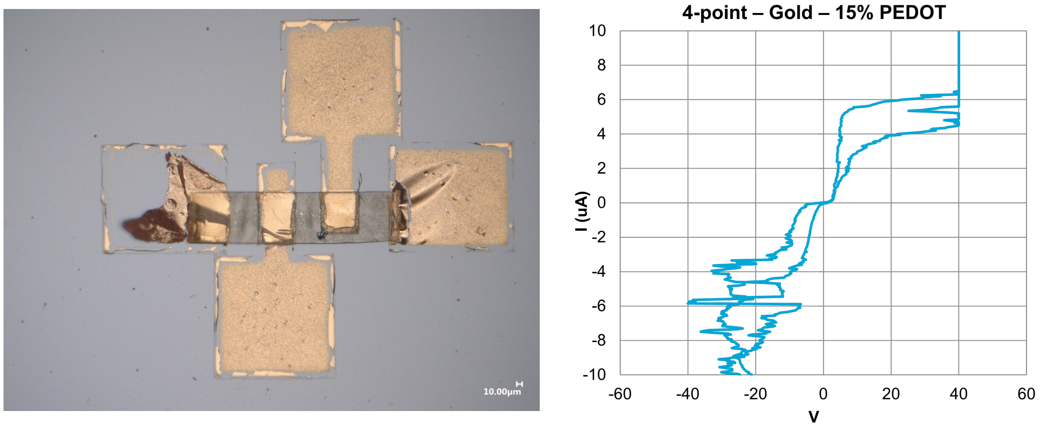

(a) **(b)**

Figure C.17: (a) 4-point probe on gold pads PEDOT 15%, (b) IV sweep